Aus dem Max-Planck-Institute für Kolloid- und Grenzflächenforschung
Abteilung Kolloidchemie

Nonaqueous Syntheses of Metal Oxide Nanoparticles and Their Assembly into Mesoporous Materials

Dissertation
zur Erlangung des akademischen Grades
"doctor rerum naturalium"
(Dr. rer. nat.)
in der Wissenschaftsdisziplin "Kolloidchemie"

eingereicht an der
Mathematisch-Naturwissenschaftlichen Fakultät
der Universität Potsdam

von

Jianhua Ba

Potsdam, im Juni 2006

给我最最亲爱的爸爸妈妈

给我最爱的晓菡

Nonaqueous Syntheses of Metal Oxide Nanoparticles and Their Assembly into Mesoporous Materials

Jianhua Ba

Abstract

This thesis mainly consist of two parts, the synthesis of several kinds of technologically interesting crystalline metal oxide nanoparticles via nonaqueous sol-gel process and the formation of mesoporous metal oxides using some of these nanoparticles as building blocks and amphiphilic block copolymer as template via evaporation induced self-assembly (EISA) technique.

In the first part, the experimental procedures and characterization results of successful syntheses of crystalline tin oxide and tin doped indium oxide (ITO) nanoparticles are reported. SnO_2 nanoparticles exhibit monodisperse particle size (3.5 nm in average), high crystallinity and particularly high dispersibility in THF, which enable them to become the ideal particulate precursor for the formation of mesoporous SnO_2. ITO nanoparticles possess uniform particle morphology, narrow particle size distribution (5-10 nm), high crystallinity as well as high electrical conductivity.

The synthesis approaches and characterization of various mesoporous metal oxides, including TiO_2, SnO_2, mixture of CeO_2 and TiO_2, mixture of $BaTiO_3$ and SnO_2, are reported in the second part of this thesis. Mesoporous TiO_2 and SnO_2 are presented as highlights of this part. Mesoporous TiO_2 was produced in the forms of both films and bulk material. In the case of mesoporous SnO_2, the study was focused on the high order of the porous structure. All these mesoporous metal oxides show high crystallinity, high surface area and rather monodisperse pore sizes, which demonstrate the validity of EISA process and the usage of preformed crystalline nanoparticles as nanobuilding blocks (NBBs) to produce mesoporous metal oxides.

Nichtwässrige Synthese von Metalloxid-Nanopartikeln und Deren Anordnung zu Mesoporösen Materialien

Jianhua Ba

Zusammenfassung

Diese Arbeit besteht hauptsächlich aus zwei Teilen. Der erste Teil befasst sich mit der Synthese von mehreren technologisch wichtigen, kristallinen Metalloxid-Nanopartikeln mittels nichtwässriger Sol-Gel Chemie. Der zweite Teil beinhaltet die Herstellung von mesoporösen Metalloxiden. Dabei wurden ausgewählte Nanopartikel als Bausteine verwendet und durch langsames Verdampfen des Lösungsmittels in die entsprechenden porösen Strukturen überführt.

Das experimentelle Vorgehen wie auch die Charakterisierung der erfolgreich hergestellten Zinnoxid- und Indiumzinnoxid-Nanopartikel sind im ersten Teil beschrieben. Die Zinnoxid-Nanpartikel zeichnen sich durch einheitliche Partikelgrösse (im Durchschnitt ca. 3.5 nm), hoher Kristallinität, und guter Dispergierbarkeit in Tetrahydrofuran aus. Diese Eigenschaften machen aus den Zinnoxid-Nanopartikeln die perfekten Bausteine für den Aufbau von mesoporösem Zinnoxid. Die Indiumzinnoxid-Nanopartikel haben eine einheitliche Partikelform, eine schmale Grösseverteilung (5-10 nm), hohe Kristallinität wie auch gute elektrische Leitfähigkeit.

Die Synthese und Charakterisierung von verschiedenen mesoporösen Metalloxiden wie TiO_2, SnO_2, Mischungen von CeO_2 und TiO_2, wie auch Mischungen von $BaTiO_3$ und SnO_2 werden im zweiten Teil der Arbeit diskutiert. Mesoporöses TiO_2 und SnO_2 werden als besonders gelungene Beispiele herausgehoben. Mesoporöses TiO_2 wurde in Form von Dünnfilmen wie auch als Bulkmaterial hergestellt. Im Falle von SnO_2 galt das Augenmerk vor allem der hohen Ordnung der Mesoporen. Alle diese mesoporösen Materialien zeigen eine hohe Kristallinität, grosse Oberfläche und relativ einheitliche Porengrössen. Diese Eigenschaften unterstreichen, wie wertvoll der Ansatz ist, vorgeformte Nanopartikel als Bausteine für die Synthese von porösen Materialien zu verwenden.

Table of Contents

Chapter 1 Introduction

1.1 Nanoscience and Nanotechnology

In the last decades, a little word attracted enormous attention, interest and investigation from all over the world: “nano”. What it presents in terms of science and technology, which are also called nanoscience and nanotechnology, is much, much more than just a word describing a specific length scale. It has dramatically changed every aspect of the way that we think in science and technology and will definitely bring more and more surprises into our daily life as well as into the world in the future.[1]

What is actually so exciting about “nano”? “Nano” means one billionth (10^{-9}), so 1 nanometer refers to 10^{-9} meter and is expressed as 1 nm. 1 nm is so small that things smaller than it can only be molecules, clusters of atoms or particles in the quantum world. Nanometer is a special point in the overall length scale because nanometer scale is the junction where the smallest manufacturable objects “meet” the largest molecules in nature. The structures, devices and systems having at least one dimension in nanometer scale are not only smaller than anything that we’ve ever made before, but also possibly the smallest solid materials that we are able to produce. Besides, in nanometer scale, the properties of materials that we are familiar with in our daily life, such as color, melting point, electronic, catalytic or magnetic properties,[2] will change dramatically or be replaced by completely novel properties due to what is usually called size effect.[3] “At this size scale, everything, regardless of what it is, has new properties. And that is, where a lot of the scientific interest is.” said Professor Alivisatos. All these make “nano” so fascinating.

What are nanoscience and nanotechnology? In fact, there are no exact definitions for them. The following is the definition of nanoscience and nanotechnology given by the US National Nanotechnology Initiative (NNI): nanoscience and –technology are

"Research and technology development at the atomic, molecular and macromolecular levels in the length scale of approximately 1-100 nanometer range, to provide a fundamental understanding of phenomena and materials at the nanoscale and to create and use structures, devices and systems that have novel properties and functions because of their small and/or intermediate size". Simply saying, nanoscience tells us how to understand the basic theories and principles of nanoscale structures, devices and systems (1-100 nm); and nanotechnology tells us what to do and how to use these nanoscale materials.

On December 29th 1959, Nobel Prize winner, physicist Richard P. Feynman said in his famous speech "There is Plenty of Room at the Bottom": "In the year 2000, when they look back at this age, they will wonder why it was not until the year 1960 that anybody began seriously to move in this (nanometer) direction." Actually, in the years after, people did want to "move in this direction". However, not much progress was made in both nanoscience and nanotechnology until 1980's when scanning tunneling microscope (STM) was invented because there were not many suitable analytical tools available to investigate nanometer scale materials.[1] After STM, highly advanced analytical tools were developed (and are still developed) rapidly, which enables the characterization and manipulation of small objects down to a few nm bringing human being's view into real atomic world. As one of the consequences of explosive development of nanoscience, nanotechnology had its breakthrough before the coming of the new century. Nowadays, many remarkable techniques, such as nanoimprint lithography, self-assembly technique, nanoscale crystal growth technique, are already available to make nanoscale products in relatively large amounts, showing the great potentials of nanotechnology in real applications.

1.2 Synthesis of Metal Oxide Nanoparticles

Although the term of nanomaterials represents a large variety of materials in the domain of nanometers, nanoparticles have been always considered as one of a few core materials in nanoscience and nanotechnology. The reasons are, in addition to the

aforementioned size effect, nanoparticles represent the most popular morphology of the nanoscale world and are ideal manipulable building blocks to construct larger devices, structures and systems following the so-called “bottom-up” approach in nanotechnology. Many discoveries related to nanoparticles synthesis, such as the discovery of carbon nanotubes, the synthesis of well-defined quantum dots or the shape control of CeSe nanocrystals, can be regarded as milestones in the history of nanoscience,[4] which further proves the important role of nanoparticles in nanoscience.

Nowadays, the synthesis, characterization and application of nanoparticles represent a highly dynamic area in both scientific research and business communities. Definitely, the synthesis of nanoparticles is the crucial step in this area. Human beings started synthesizing and utilizing nanoparticles more than thousand years ago. Ancient Chinese used carbon nanoparticles to produce the famous and superfine Hui Ink for handwritings and paintings, still keeping their fresh color after thousand years. Roman glassmakers used noble metal nanoparticles to fabricate colored glasses as early as in the fourth century A. D. Real scientific research on nanoparticles was started in the mid-nineteenth century by M. Faraday and hasn’t experienced tremendous development until the last decades. Today, there is a huge toolbox available to successfully synthesize both organic and inorganic nanoparticles with great diverse approaches. For instance, liquid-phase techniques, including coprecipitation, sol-gel chemistry, microemulsion, hydrothermal/solvothermal processing and template syntheses, are particularly versatile for the synthesis of inorganic particles regarding its ability of synthesizing broad classes of nanoparticles and controlling particle size and morphology.[4]

Among various classes of inorganic nanoparticles, metal oxide nanoparticles are particularly attractive from both scientific and technological point of view. The unique characteristics of metal oxides make them the most diverse class of materials, with optical, electronic, electrical, photoelectronic, catalytic or magnetic properties

covering almost all aspects of materials science and solid state physics.[4] When metal oxides are brought into nanometer scale, they further exhibit improved or completely novel properties compared to their bulk materials. Their fascinating properties certainly enable their various applications in nanotechnology, such as in gas sensing, electroceramics, catalysis, superconductors and energy conversions, etc.

In my PhD work, the synthesis of metal oxide nanoparticles, precisely SnO_2, tin doped indium oxide (ITO) and $YBa_2Cu_3O_7$ (YBCO) nanoparticles, was one of the two major subjects. The common feature of the syntheses of these three kinds of metal oxide nanoparticles is that they were all synthesized via nonaqueous sol-gel process. More information about aqueous and nonaqueous sol-gel syntheses will be given in chapter 3. Herein, I just want to briefly introduce the basics of sol-gel process.

Simply saying, sol-gel process is the procedure that molecular precursors, e.g. metal chlorides or metal alkoxides, react with certain solvent, e.g. H_2O or organic solvents, and form 3D metal oxide network via inorganic polymerization including hydrolysis/solvolysis and condensation reactions. Conventionally, aqueous sol-gel process, in which water is the solvent, is broadly used for the synthesis of metal oxide bulk materials as well as nanoparticles. The reaction mechanisms of hydrolysis and condensation processes are shown in the following.[5] Firstly, the metal alkoxide or metal chloride is hydrolyzed and an M-OH species is generated:

Hydrolysis

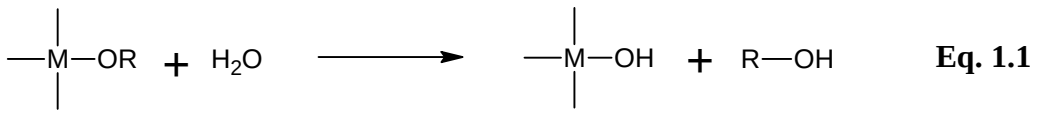

Eq. 1.1

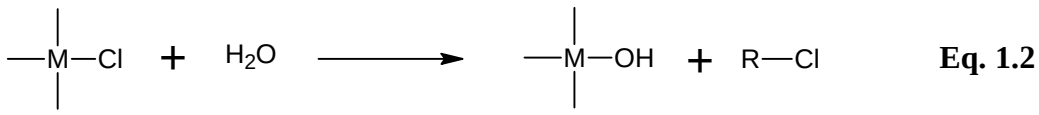

Eq. 1.2

In the second step, the hydroxy groups react with each other or other metal alkoxide/chloride and a 3D M-O-M network is then formed upon the propagation of the condensation reaction and results in the elimination of ROH, water or HCl.

Condensation

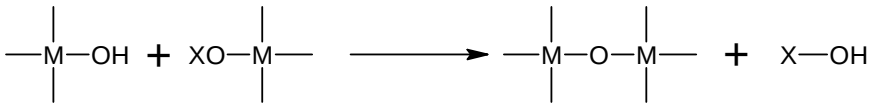

Eq. 1.3

(X=H or R)

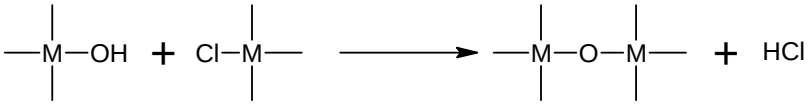

Eq. 1.4

The reaction mechanism of aqueous sol-gel process is rather simple. However, resulting from the high reactivity of the precursor towards hydrolysis,[6] it has several disadvantages. For instance, the resulting products are often amorphous, which means that post thermal treatments are not avoidable to get crystalline material; the reaction parameters, such as temperature, pH, concentration of anions and even the method of mixing, have to be carefully controlled to achieve the desired products and reproducibility.

As an alternative to aqueous sol-gel techniques, nonaqueous sol-gel process has become more and more popular in the past ten years because it exhibits great advantages in contrast to aqueous sol-gel chemistry. Instead of water, organic solvents, such as alcohols, ketones or amines, are used as the liquid phase reactants. Various metal oxide precursors are used in these procedures, ranging from organometallic complexes to metal halides, alkoxides and acetylacetonates. In contrast to aqueous sol-gel process, nonaqueous sol-gel process possesses several advantages, such as better control of particle formation due to slower reaction rates between precursors and organic solvents, high crystallinity of the achieved nanoparticles at relatively moderate temperatures (100-300°C) and homogeneous particle morphology within one reaction system, etc. What is also one of the advantages of nonaqueous sol-gel chemistry is that the control over particle sizes, shapes and compositions is possible because of the large variety of organic solvents and the well understood organic reaction processes.[4]

The reaction mechanism of nonaqueous sol-gel chemistry is more complex than aqueous sol-gel chemistry, and a lot of studies on it are still going on.[4] Therefore, the general reaction schemes of nonaqueous sol-gel process are not presented here. However, detailed individual reaction mechanisms of the syntheses of SnO_2 and ITO nanoparticles will be proposed in Chapter 3.

1.3 Synthesis of Mesoporous Materials

Since the time when nanoscience became popular, people have been always thinking how to bring the fascinating properties of individual nanoscale objects into the macroscopical world. In contrast to direct uses of nanomaterials as powders or dispersions, manufacturing highly complex devices and systems with novel properties by precise control and utilization of nanomaterials as building blocks is very challenging and promising to maximize their potential applications in nanotechnology. However, great difficulties to handle the nanomaterials make the conventional manufacturing technology inapplicable in nanoscale domain. Many techniques inspired by traditional technology, such as nanoimprint lithography, dip-pen nanolithography, have been applied into nanotechnology and considered as "top-down" technique. As a representative of "bottom-up" technique, self-assembly approaches attract more and more interests.

"A general definition of self-assembly is the spontaneous organization of materials through noncovalent interactions (hydrogen bonding, Van der Waals forces, electrostatic forces, etc.) with no external intervention."[7] Self-assembly involves "components from the molecular (crystals) to the planetary (weather systems) scale".[8] The driving force of self-assembly is that the organizing materials (molecules, molecular clusters, polymers, or, generally speaking, building blocks) always try to minimize their energy, including potential energy, interfacial energy, electrostatic energy, etc.

Self-assembly technique has been broadly used by the nature to construct highly

complex biological supramolecules, tissues and systems. However, it is only about 100 years since scientists started thinking and understanding supramolecular chemistry, which is the basis of self-assembly technique. Because large-scale materials with nanostructural features can be "automatically" produced by using this technique, self-assembly exhibits great advantages as a representative of "bottom-up" route in nanotechnology. Due to its versatility, ability and low costs to fabricate complex systems in different length scales, self-assembly will probably become the most important technique in nanotechnology.[1]

As one of the main applications of self-assembly technique, the successful synthesis of mesoporous SiO_2 by the researchers of Mobil in 1992 opened up the exciting development of mesoporous materials, which possess the pore sizes in the range of 2-50 nm.[9] Before 1990, mesoporous materials with highly ordered pore structures had never been realized since there was no template available in the nature for the synthesis of mesoporous materials. After the great discovery of synthesizing mesoporous materials via self-assembly approach, scientists had rapidly extended mesoporous materials from SiO_2 related materials to other metal oxides, such as TiO_2, ZrO_2, Nb_2O_5, WO_3,[10] Ta_2O_5,[11] CeO_2,[12, 13] SnO_2,[14] etc. Meanwhile, studies focusing on the formation mechanisms of mesoporous structures were also equally active and reported by various groups.[7, 15-21]

The basic idea of synthesizing mesoporous materials via self-assembly approach is to utilize the amphiphilicity of surfactants or block copolymers. It is well known that surfactants and amphiphilic block copolymers are able to form different liquid crystal structures when their concentrations are above the critical micelle concentrations (CMC). Nowadays, amphiphilic block copolymers attracts much more interests than small molecule surfactants because they have many advantages, such as the wide variability of the structure of the block polymers, broadly adjustable liquid crystalline structures, low CMC, being able to form long lifetime block-copolymer micelles, etc.[17] A schematic figure illustrating the common morphologies of

micorphase-separated block copolymers is presented in Figure 1.1, in which one can see the various liquid crystalline morphologies that can be achieved by using amphiphilic block copolymers.

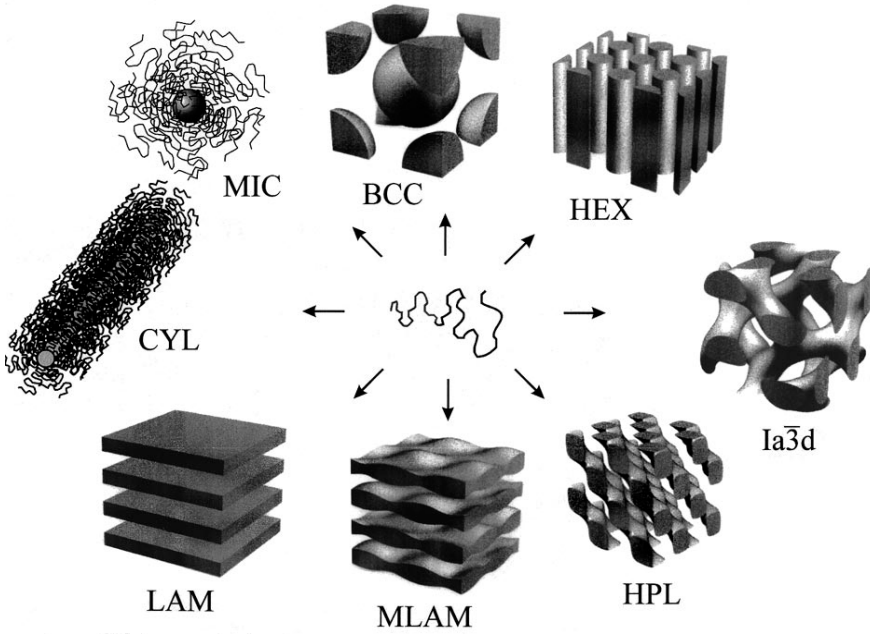

Figure 1.1 Common morphologies of microphase-separated block copolymers: body centered cubic (bcc) packed spheres (BCC), hexagonally ordered cylinders (HEX), gyroid (Ia3d), hexagonally perforated layers (HPL), modulated lamellae (MLAM), lamellae (LAM), cylindrical micelles (CYL), and spherical micelles (MIC).[17]

In the next step of the procedure of mesopores formation, the "soft" liquid crystalline structures behave as templates and their morphology are transformed into inorganic framework via nanocasting/-coating technique[22, 23] and inorganic polymerization. After the removal of the organic templates (extraction or calcination), pure inorganic materials with desired mesoporous morphology can be achieved. Detailed formation mechanisms of mesoporous materials via self-assembly approach are available in aforementioned references[7, 15-21] and therefore not repeated here.

In my PhD work, amphiphilic block copolymer, polybutylene-block-poly(ethylene oxide) (PB-PEO), was employed as the main template for the formation of

mesoporous TiO_2, SnO_2, mixtures of CeO_2 and TiO_2, $BaTiO_3$ and SnO_2. Preformed crystalline nanoparticulate TiO_2, SnO_2, etc., were used as precursors instead of conventional molecular precursors in synthesizing mesoporous metal oxides. Fully detailed synthesis procedures and characterization of above mesoporous metal oxides are presented in Chapter 4.

References

[1] M. Ratner, D. Ratner, *Nanotechnology: A Gentle Introduction to the Next Big Idea*, Person Education, Inc., **2003**.

[2] A. Eychmuller, *J. Phys. Chem. B* **2000**, *104*, 6514.

[3] C. N. R. Rao, A. Mueller, A. K. Cheetham, *The Chemistry of Nanomaterials: Synthesis, Properties and Applications, Vol.1*, Wiley-VCH, Weinheim, **2004**.

[4] M. Niederberger, G. Garnweitner, *Chem. Eur. J.* **2006**, in print.

[5] C. J. Brinker, G. W. Scherer, *Sol-Gel Science*. *Academic Press* **1990**.

[6] C. Sanchez, J. Livage, *New J. Chem.* **1990**, *14*, 513.

[7] C. J. Brinker, Y. F. Lu, A. Sellinger, H. Y. Fan, *Adv. Mater.* **1999**, *11*, 579.

[8] G. M. Whitesides, B. Grzybowski, *Science* **2002**, *295*, 2418.

[9] C. T. Kresge, M. E. Leonowicz, W. J. Roth, J. C. Vartuli, J. S. Beck, **1992**, *359*, 710.

[10] P. D. Yang, D. Y. Zhao, D. I. Margolese, B. F. Chmelka, G. D. Stucky, *Nature* **1998**, *396*, 152.

[11] D. M. Antonelli, J. Y. Ying, *Chem. Mater.* **1996**, *8*, 874.

[12] A. Corma, P. Atienzar, H. Garcia, J. Y. Chane-Ching, *Nat. Mater.* **2004**, *3*, 394.

[13] A. S. Deshpande, N. Pinna, B. Smarsly, M. Antonietti, M. Niederberger, *Small* **2005**, *1*, 313.

[14] J. Ba, J. Polleux, M. Antonietti, M. Niederberger, *Adv. Mater.* **2005**, *17*, 2509.

[15] G. J. d. A. A. Soler-Illia, C. Sanchez, B. Lebeau, J. Patarin, *Chem. Rev.* **2002**, *102*, 4093.

[16] C. G. Göltner, M. Antonietti, *Adv. Mater.* **1997,** *9,* 431.

[17] S. Förster, M. Antonietti, *Adv. Mater.* ***19*98,** *10,* 195.

[18] G. A. Ozin, *Chem. Comm.* **2000,** 419.

[19] D. Grosso, G. J. d. A. Soler-Illia, E. L. Crepaldi, F. Cagnol, C. Sinturel, A. Bourgeois, A. Brunet-Bruneau, H. Amenitsch, P. A. Albouy, C. Sanchez, *Chem. Mater.* **2003,** *15,* 4562.

[20] D. Grosso, F. Cagnol, G. J. de A. A. Soler-Illia, E. L. Crepaldi, H. Amenitsch, A. Brunet-Bruneau, A. Bourgeois, C. Sanchez, *Adv. Funct. Mater.* **2004,** *14,* **3**09.

[21] D. Grosso, C. Boissiere, B. Smarsly, T. Brezesinski, N. Pinna, P. A. Albouy, H. Amenitsch, M. Antonietti, C. Sanchez, *Nat. Mater.* **2004,** *3,* **787**.

[22] R. A. Caruso, M. Antonietti, *Chem. Mater.* **2001,** *13,* **32**72.

[23] R. A. Caruso, *Top. Curr. Chem.* 2003, *22**6,*** **9**1.

Chapter 2 Analytical Methods

In the first part of this chapter, the basic theories and principles of the three main analytical methods X-ray analysis, electron microscopy and specific surface area measurement, are discussed. In the second part, the experimental parameters and instrumental details of all the characterization tools used in this thesis are summarized.

2.1 Main Analytical Methods

2.1.1 X-ray Analysis

2.1.1.1 Basis of X-rays

X-rays are defined as short-wavelength electromagnetic radiation produced by the deceleration of high-energy electrons or by electronic transitions involving electrons in the inner orbitals of atoms. The wavelength range of X-rays is from perhaps 10^{-4} nm to about 10 nm.[1] Since its first discovery by Wilhelm Conrad Roentgen, the techniques based on the measurement of fluorescence, absorption, scattering and diffraction of X-rays have been developed and broadly used to investigate the compositions and structures of matters.

For analytical purposes, X-rays are obtained in three ways, (1) by bombardment of a metal target with a beam of high-energy electrons, (2) by exposure of a substance to a primary beam of X-rays in order to generate a secondary beam of X-ray fluorescence, and (3) by employment of radioactive source whose decay process results in X-ray emission. X-ray tube and synchrotron are the well-known equipments for the generation of X-rays. X-ray tubes are basically used for the measurements of scattering and diffraction of X-rays and quite usual in the common X-ray labs due to their relatively simple structures and much lower cost than synchrotron. In an X-ray tube, electrons produced at a heated cathode are accelerated toward a metal anode (the target) by a potential as great as 100 kV; upon collision, part of the energy of the

electron beam is converted to X-rays.

Because the wavelengths of X-rays are on the nanometer scale, they are especially suitable for investigating the substances in nanometer or atomic scales, which are invisible by using electromagnetic radiations with longer wavelengths, such as visible light or ultraviolet. Furthermore, in contrast to neutrons, which are sensitive to the difference of nucleus of the matters, X-rays are sensitive to the changes of electron densities. Therefore, they are mainly utilized to study materials having nonuniform electron densities.

2.1.1.2 Bragg's Law

By analogy with the diffraction of light by an optical grating, crystals, with their regularly repeating structures, should be capable of diffracting radiation that has a wavelength similar to interatomic separations, ~2-3Å. Three types of radiation are used for crystal diffraction studies: X-rays, electrons and neutrons. Of these, X-rays are the most useful and popular.[2]

For the investigation of crystal structures by X-ray diffraction, Bragg's law is the most basic and important principle. It was formulated in 1912 by W. L. Bragg in order to explain the observed phenomenon that crystals only reflected X-rays at certain angles of incidence. The Bragg approach to diffraction is to regard crystals as composed of layers or planes such that each acts as a semi-transparent mirror. Some of the X-ray is reflected off a plane with the angle of reflection equal to the angle of incidence, but the rest are transmitted to be subsequently reflected by succeeding planes.

The derivation of Bragg's law is shown in Figure 2.1. Two X-ray beams, 1 and 2, are reflected from adjacent planes, A and B, within the crystal and we wish to know under what conditions the reflected beams 1' and 2' are in phase. Beam 22' has to travel the extra distance *xyz* as compared to beam 11', and for 1' and 2' to be in phase, distance *xyz* must equal a whole number of wavelengths. The perpendicular distance between pairs of adjacent planes, the *d-spacing*, *d*, and the angle of incidence, or Bragg angle,

θ, related to the distance xy by $xy = yz = d\sin\theta$. Thus, $xyz = 2d\sin\theta$. But $xyz = n\lambda$, therefore

$$2d \sin\theta = n\lambda \qquad \textbf{Eq. 2.1}$$

which is so-called Bragg's law. When Bragg's law is satisfied, the reflected beams are in phase and interfere constructively.

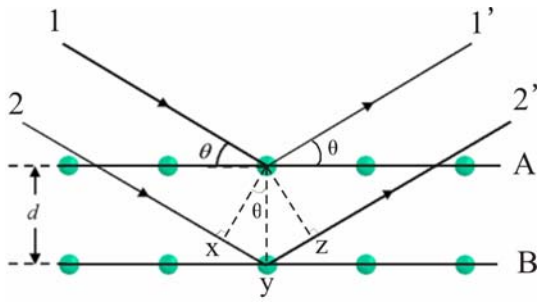

Figure 2.1 Scheme for the derivation of Bragg's law.

2.1.1.3 Wide Angle X-ray Scattering (WAXS)

Powder X-ray diffraction (XRD), which also refers to wide angle X-ray scattering (WAXS), is nowadays broadly used to study the crystal structures of polycrystalline materials. The principle of XRD is shown in Figure 2.2. A monochromatic beam of X-rays strikes a finely powdered sample that has crystals randomly arranged in every possible orientation. In such a powder sample, the various lattice planes are also present in every possible orientation. For each set of planes, therefore, at least some crystals must be orientated at the Bragg's angle, θ, to the incident beam and thus, diffraction occurs for these crystals and planes. The diffracted beams may be detected by using a Geiger counter or scintillation counter connected to a computer (diffratometer). The computer is then able to plot the characteristic XRD/WAXS pattern of the measured sample upon the detected X-ray intensities on different positions. This pattern can be further used to determine the crystal structure and other structural features of the specimen.

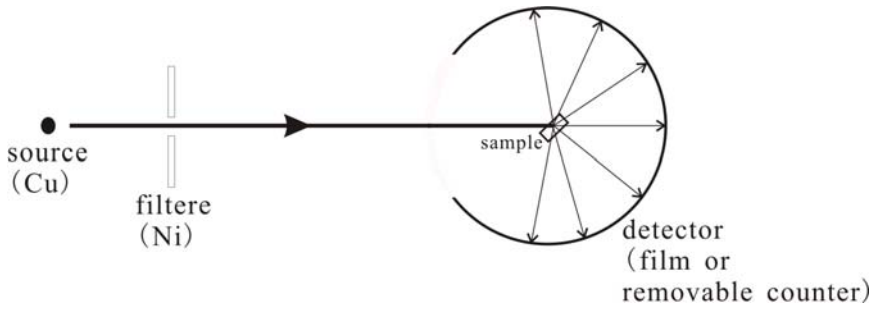

Figure 2.2 Schematic diagram of the setup of X-ray powder diffraction.

2.1.1.4 Small angle X-ray Scattering (SAXS)

According to Bragg's law, when the wavelength of the X-ray is constant, smaller angles lead to the detection of large *d-spacing*. In SAXS, the angle of incidence is usually smaller than 5 degrees, which means that it detects the *d-spacing* in the domain of nanometers. Therefore, SAXS is a technique for studying structural features in the nanometer range. It is performed by focusing a low divergence X-ray beam onto a sample and observing a coherent scattering pattern that arises from electron density inhomogeneities within the sample. Due to its considerable ability to probe the materials in nanometer scales, SAXS plays an important role in nanoscience, such as polymer research, medical-biological studies, catalyst development and so on.

There are mainly two kinds of collimation systems broadly used to provide a low divergence X-ray beam for SAXS: Kratky camera and Pinhole camera. The advantages of the former one is: (1) simple structure as well as low running cost, (2) satisfying efficiency due to its relatively high intensity of X-ray beam. Therefore, the Kratky camera can be found in many X-ray labs. The schematic diagram of Kratky camera is shown below in Figure 2.3.

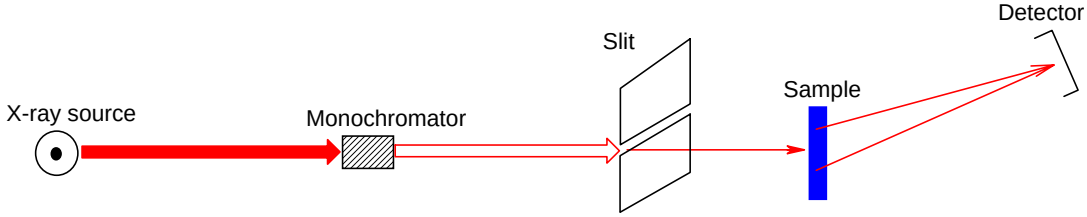

Figure 2.3 Schematic diagram of Kratky camera.

2.1.2 Electron Microscopy

Electron microscopy is extremely versatile for providing structural information over a wide range of resolution from 10 µm to 2 Å. Especially in the range where the specimen is so small (<1µm) that optical microscopes are not able to image it anymore. Electron microscopes operate in either transmission (TEM) or reflection (SEM) mode. The basic principle and setup of each working mode are briefly introduced in the following.

2.1.2.1 Transmission Electron Microscopy (TEM)

In TEM, the ray of electrons is produced by a pin-shaped cathode heated up by current. The electrons are vacuumed up by a high voltage at the anode. The acceleration voltage is between 50 and 150 kV. The higher it is, the shorter are the electron waves and the higher is the power of resolution. But this factor is hardly ever limiting. The power of resolution of electron microscopy is usually restrained by the quality of the lens-systems and especially by the technique with which the preparation has been achieved. Modern gadgets have powers of resolution that range in 2-3 Å.

The accelerated beam of electrons passes a drill-hole at the bottom of the anode. Its following way is analogous to that of a ray of light in a light microscope. The lens-systems consist of electronic coils generating an electromagnetic field. The beam is first focused by a condenser, and then passes through the object, where it is partially deflected. The degree of deflection depends on the electron density of the object. The greater the mass of the atoms, the greater is the degree of deflection. Biological objects have only weak contrasts since they consist mainly of atoms with low atomic numbers (C, H, N, O). Consequently it is necessary to treat the preparations with special contrast enhancing chemicals (heavy metals) to get at least some contrast. Additionally they must not be thicker than 100 nm, because the temperature is rising due to electron absorption. This again can lead to destruction of the specimen. It is generally impossible to examine living objects.

After passing the object the scattered electrons are collected by an objective. Thereby an image is formed, that is subsequently enlarged by an additional lens-system (projective with electron microscopes). The thus formed image is made visible on a fluorescent screen or it is documented on photographic material. Photos taken with electron microscopes are always black and white. The schematic diagram of the setup of TEM is presented in Figure 2.4a.

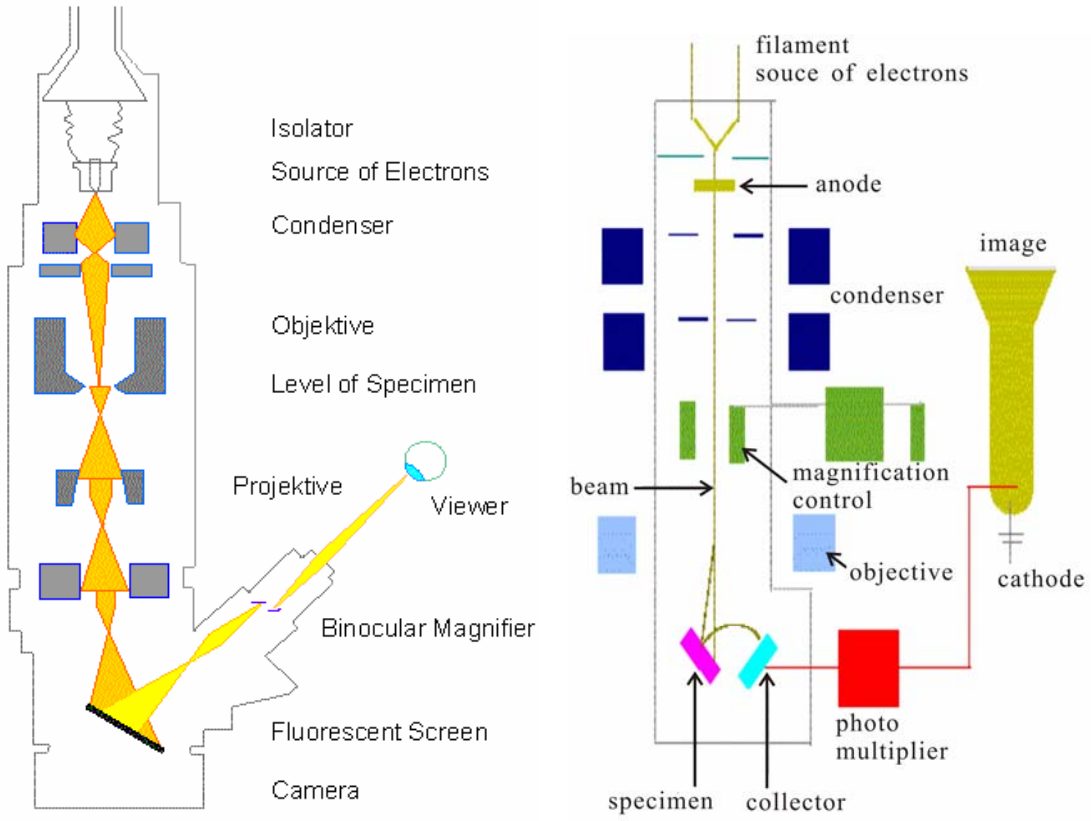

(a) (b)

Figure 2.4 Schematic diagrams of the setups of TEM (a) and SEM (b).

2.1.2.2 Scanning Electron Microscopy (SEM)

The path of the electron beam within the scanning electron microscope differs from that of the TEM. The technology used is based on television techniques. The method is suitable for the depiction of preparations with conductive surfaces. Biological objects have thus to be made conductive by coating with a thin layer of heavy metal, e.g. gold. The power of resolution is normally smaller than in transmission electron microscopes, but the depth of focus is several orders of magnitude greater. Scanning

electron microscopy is therefore also well-suited for very low magnifications.

The surface of the object is scanned with the electron beam point by point whereby secondary electrons are set free. The intensity of this secondary radiation is dependent on the angle of inclination of the object's surface. The secondary electrons are collected by a detector that sits at an angle at the side above the object. The signal is then enhanced electronically. The magnification can be chosen smoothly (depending on the model) and the image appears a little later on a viewing screen. The schematic diagram of the setup of SEM is presented in Figure 2.4b.

2.1.3 Characterization of Porosity

The porosity, such as pore size and specific surface area, is one of the most relevant properties of porous materials. On the basis of the pore diameter, an official classification was proposed by the International Union of Pure and Applied Chemistry (IUPAC), [3, 4] which is given in Table 1 below.

Table 2.1 Classification of pores according to their diameter or width

Classification of pores	Pore size
Micropores	< 2 nm
Mesopores	2 nm to 50 nm
Macropores	> 50 nm

By measuring the gas adsorption isotherms of numerous porous materials, six types of isotherms have been summarized (shown in Figure 2.5).[4, 5] The relative pressure is expressed by p/p^0, where p is the pressure of the vapour and p^0 is the saturation vapour of the adsorptive.

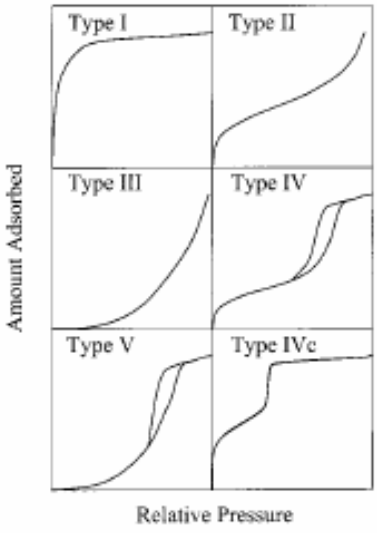

Figure 2.5 Classification of gas adsorption isotherms.

In Figure 2.5, the isotherm of Type I is considered as the isotherm of microporous materials. Type II and Type III are associated with nonporous and macroporous materials, respectively. Type IV and Type V are all the exhibitions of mesoporosity. Type IVc is of theoretical interest and relatively rare in practice. Various types of isotherms shown in Figure 2.5 are all related to the different behaviours of the interactions between the adsorbents, the solids, and the adsorbates, the adsorbed gas such as nitrogen, in microporous, mesoporous or macroporous materials. Therefore, the isotherm of one substance can be utilized to determine its pore size qualitatively.

The specific surface area is another important aspect of porosity. Usually, the specific surface area is expressed by the following equation:

$$A = \frac{a}{m} \qquad \textbf{Eq. 2.2}$$

where A is the specific surface area, m^2/g; a is the total surface are of a measured sample, m^2; m is the mass of the measured sample, g. Currently, there are two main methods to evaluate the specific surface area from the gas adsorption data: the Brunauer-Emmett-Teller (BET) method and the comparative method.[4, 5] The basic idea of BET method is to evaluate the specific surface area by fitting the adsorption

data to the BET model and equation.[4] The same purpose as BET method is realized by comparing the adsorption isotherm for a given porous material with the adsorption isotherm for a suitable reference adsorbent of known specific surface area.

2.2 Experimental Details of Samples Characterization

2.2.1 X-ray measurements

Wide angle X-ray scattering (WAXS) measurements were performed on an Enraf-Nonius PDS-120 powder diffractometer in reflection mode, using an FR-590 generator as the source of Cu Kα radiation. A Nonius CPS-120 curved position sensitive detector, showing a resolution of $2\theta = 0.018°$, was employed to record the scattered radiation. Alternatively, a Bruker D8 diffractometer equipped with a scintillation counter was used. The samples were measured in θ–θ reflection mode (under CuKα radiation)

Small angle X-ray scattering (SAXS) measurements were performed by using a Kratky camera assembly manufactured by Anton Paar, Germany. The samples were analyzed in transmission mode under vacuum with an X-ray source of Cu Kα radiation.

2.2.2 Transmission Electron Microscopy (TEM)

Transmission electron microscopy (TEM) was performed on a Zeiss EM 912Ω instrument at an acceleration voltage of 120 kV. The samples usually were prepared by dispersing a small amount of powder in ethanol. Next, one drop of the dispersion was put on a carbon-coated copper grid (400 mesh) and left to dry under ambient conditions before insertion into the device.

High-resolution transmission electron microscopy (HRTEM) in phase contrast was performed at 200 kV on a field-emission instrument of the type Jeol JEM-2100F with an ultra-high resolution pole piece, providing a point-resolution better than 0.19 nm. An Oxford Instruments INCA-200-TEM system with an ultra-thin window was

connected to the microscope that allowed elemental analysis using energy-dispersive X-ray spectroscopy (EDXS). Moreover, the microscope was equipped with an energy filter of the type Gatan GIF 2001 with a 1k-CCD camera. The filter was used to enhance the dynamics in selected area electron diffraction (SAED) pattern by elastic filtering with a band width of 15 eV. The samples were deposited as dry powders on 300-mesh copper-supported carbon films.

2.2.3 Scanning Electron Microscopy (SEM)

A LEO1550-Gemini instrument was used for obtaining SEM images of the samples. The samples were loaded on carbon-coated stubs and sputter coated with Au/Pd alloy prior to analysis.

2.2.4 Nitrogen Adsorption Experiments

Nitrogen adsorption and desorption isotherms of various porous materials were all measured at 77 K with a Micromeritics Tristar 3000 system. Prior to the measurement, the sample was degassed at 150°C overnight under vacuum. For the determination of the surface area, the BET method was used.

2.2.5 X-ray Photoelectron Spectroscopy (XPS)

XPS measurements were taken on a Physical Electronics ESCA 5600 spectrometer with a monochromatic Al-K_α X-ray source at a power of 200 W/14 kV and a multi channel detector OmniIV. The electron take-off angle (θ) to the sample surface was adjusted to 45°. The base pressure of the sample chamber was around $4x10^{-8}$ Pa throughout the measurements. Spectra were obtained for both, high-resolution mode (pass energy of 58.70 eV, 0.125 eV/step) for C1s, O1s, Sn3d and In3d and low-resolution mode (pass energy of 187.85 eV, 0.8 eV/step). Binding energies for the high-resolution spectra were calibrated by setting C1s at 284.6 eV. Gaussian-Lorentzian curves and Shirley background were applied for photoelectron peak analysis.

2.2.6 Thermogravimetric Analysis (TGA)

The TGA measurements were carried out using a Netzsch thermoanalyzer TG 209, measuring under nitrogen from room temperature to 930°C at a heating rate of 20°C/min. Ceramic crucibles were used as sample holders. For one measurement, about 5 mg sample was used.

2.2.7 Nuclear Magnetic Resonance (NMR) Analysis

NMR analysis was performed on a Bruker DPX400 spectrometer at 100 MHz for ^{1}H-BB-decoupled ^{13}C measurements, at a sample spinning rate of 20 Hz, and a ZG30 pulse program.

2.2.8 Analytical Ultracentrifugation (AUC)

Analytical ultracentrifugation was performed on a Beckman Optima XL-I centrifuge (Beckman/ Coulter, Palo Alto, CA) with a scanning absorption optics and on-line Rayleigh interferometer. For the determination of the particle size distribution of SnO_2, the absorbance was measured at the two wavelengths of 400 nm and 450 nm at 10000 rpm at 25°C in a band centrifugation experiment to allow for an optimum particle separation. 12 µL of the SnO_2 dispersion in water (ρ_{SnO2}= 6.95 g/cm^3) were overlaid onto 300 µL D_2O in a self-made 12 mm synthetic boundary epon cell of the Vinograd type to avoid convection problems. The UV/Vis spectra were taken at radial positions where the local particle size was known from prior and subsequent radial scans.

References

[1] B. Chu, B. S. Hsiao, *Chem. Rev.* **2001**, *101*, 1727.

[2] A. R. West, *Basic Solid State Chemistry-Second Edition*, John Wiley & Sons, Ltd., **1995**.

[3] IUPAC, *Pure and Applied Chemistry* **1972**, *31*, 578.

[4] S. J. Gregg, K. S. W. Sing, *Adsorption, Surface Area and Porosity-2nd Edition*, Academic Press Limited. United Kingdom., **1997**.

[5] M. Kruk, M. Jaroniec, *Chem. Mater.* **2001**, *13*, 3169.

Chapter 3 Nonaqueous Syntheses of Crystalline Metal Oxide Nanoparticles

3.1 Introduction

As one of the important aspects of colloid chemistry, the syntheses of metal oxides with nanoscale features, typically nanoparticles, nanotubes and nanowires etc., with well-controlled size and shape as well as size distribution attract enormous attention and investigation from both academia and industry. Immense efforts have been dedicated into this field for decades and many traditional metal oxides with improved or novel properties have been achieved by following the approach of bringing the materials into the domain of nanometers.[1-8]

Conventionally, the direct reaction of a mixture of powders is often used to synthesize metal oxide materials. However, because high temperature and homogeneous distribution of the reactants are required in this kind of solid state reaction, it is always rather difficult to really control the particle size as well as particle morphology.[9] A promising alternative approach to solid state reactions is the use of soft-chemistry routes,[10, 11] which allow relatively good control over particle size and shape under rather moderate processing conditions. Broadly used aqueous sol-gel chemistry in synthesizing bulk metal oxides is usually considered as the main concept of making metal oxide nanoparticles.[8] Comparing with solid state reactions, the aqueous sol-gel synthesis route has obvious advantages, such as high purity products and low processing temperatures. However, it also has some crucial disadvantages. One of its major drawbacks is that the aqueous sol-gel synthesis usually results in amorphous precipitates due to very fast hydrolysis and condensation processes and subsequent thermal treatment is necessary to achieve crystalline nanoparticles. Another disadvantage of aqueous sol-gel synthesis is the difficulty to control the reaction parameters, such as fast hydrolysis rate of the metal alkoxides, pH values, method of mixing, rate of oxidation and especially the nature and concentration of anions, which

could all strongly impact the morphology of the final products.[12, 13] In order to overcome the drawbacks of aqueous sol-gel routes, a new branch of sol-gel chemistry, nonaqueous sol-gel route, has been introduced into people's view and become very promising to synthesize metal oxide nanoparticles.

Nonaqueous sol-gel synthesis approach was firstly reported in 1928 by Dearing and Reid[14] and became popular at the beginning of the nineties in the scientific community.[15, 16] It usually involves the reaction between metal oxide precursors, ranging from organometallic complexes to metal halides, alkoxides and acetylacetonates, and alcohols or other inert organic solvents, such as amines and ketones. Because of the lower reactivities of the organic solvents towards metal oxide precursors, the rapid solvolysis-condensation process is slowed down and performed in a more well-controlled fashion. As one of the results of the slow solvolysis-condensation process, the resulting metal oxide products are highly crystalline in most of the cases, and consequently, post thermal treatments are not necessary anymore, and the particle morphologies are then well preserved. Another advantage of nonaqueous sol-gel route is that the organic solvents behave not only as reacting agents, but also as stabilizing agents, which enable us to control the growth, surface properties and dispersibility of the resulting nanoparticles. These great advantages of the nonaqueous synthesis approach make it a valuable alternative to aqueous routes and enrich rapidly the family of the metal oxide nanoparticles synthesized by this nonhydrolytic reaction route.[17-19]

Among a variety of available organic solvents that could be used in the nonaqueous synthesis of metal oxide nanoparticles, benzyl alcohol is particularly versatile as found by M. Niederberger and his coworkers. A large number of metal oxide nanoparticles, such as TiO_2,[20] V_2O_3,[21] SnO_2, In_2O_3,[22, 23] HfO_2,[24] ZrO_2,[23] $BaTiO_3$, (Ba, Sr)TiO_3[25] etc., with well-controlled particle size and various morphology and/or specific surface properties and/or good dispersibility[26, 27] have been synthesized successfully and reported in the past few years. Furthermore, some novel reaction

mechanisms, such as the mechanism of $BaTiO_3$ synthesis involving a C-C bond formation,[28] have been proposed. The high versatility of benzyl alcohol also made it come into my consideration of synthesizing nanoparticles of SnO_2, tin doped indium oxide (ITO) and one of the most important superconductors, YBCO.

In this chapter, I would present the successful nonaqueous syntheses of SnO_2[27] and ITO nanoparticles.[29] Besides, the unsuccessful synthesis of YBCO will also be reported and discussed. The unique feature of SnO_2 nanoparticles reported here comparing with previous work in our group is that they are perfectly dispersible in THF, which opens a pathway towards the synthesis of highly ordered mesoporous structures. The specialities of ITO nanoparticles presented in this chapter are their monodisperse particle size, uniform particle morphology and high electrical conductivity.

3.2 Nonaqueous synthesis of SnO_2 nanocrystals

The unique characteristics of tin oxide make it a key functional material with applications in gas sensing,[30, 31] catalysis,[32, 33] electrochemistry[34] and optoelectronic devices.[35, 36] For many of these applications, high surface areas, which are typical of small particle sizes, are important prerequisites. Accordingly, a large variety of tin oxide nanoparticles with different sizes and shapes were reported using sol-gel,[22, 37-39] thermal evaporation,[40] or laser ablation techniques.[41, 42] However, in order to achieve optimized access to surface area and flow rates through the material, well structured porosity on the nanometer scale is an additional important morphological feature. Although partially crystalline mesoporous materials have been reported a few years ago,[43] the preparation of fully crystalline networks is still a major issue, mainly due to the fact that many oxide mesostructures collapse during the crystallization process. The use of templates that promote to formation of larger pores was able to solve this problem enabling the synthesis of mesoporous crystalline TiO_2,[44] CeO_2, ZrO_2,[45] and $SrTiO_3$.[46] However, the synthesis of mesostructured tin

oxide remains particularly challenging. Although several reports were published on this topic,[47-55] none of these materials preserved an ordered mesoporous structure after removal of the surfactants by calcination. In order to circumvent these problems, the polymer-directed assembly of preformed crystalline nanoparticles into mesostructures should be a valuable alternative route. However, the synthesis of nanoparticles with well-defined shape and size, which can be redirspersed without agglomeration, keeps this approach from being frequently applied, and only few examples such as mesoporous tungstated zirconium oxide,[56] titania[57] and ceria[58, 59] are known.

In the following part of my work, the nonaqueous synthesis and characterization of SnO_2 nanocrystals with a rather small particle size distribution are presented. Particularly, the very high dispersibility of the SnO_2 nanoparticles in THF fulfills the demand on nanoparticulate precursor sols for synthesizing mesoporous SnO_2, offering the possibility to form highly ordered mesoporous structures via evaporation induced self-assembly (EISA), which will be further discussed in Chapter 4. Furthermore, the formation mechanism of SnO_2 nanoparticles will also be briefly discussed.

3.2.1 Experimental

3.2.1.1 Synthesis of SnO_2 Nanoparticle Sols

In contrast to our previous work on crystalline tin oxide nanoparticles,[22] we prepared the sols by reacting tin chloride with benzyl alcohol in a beaker without any subsequent solvothermal treatment. In a typical synthesis procedure, 1 ml (8.54 mmol) tin (IV) chloride (Sigma-Aldrich, 99%) was slowly and dropwise added to 20 ml (193.3 mmol) benzyl alcohol (Sigma-Aldrich, 99+%) under vigorous stirring. The reaction mixture was heated in an oil bath at 100ºC for 24 h and at 110°C for another 6 h. The white precipitate was collected by centrifugation and immediately dispersed in 20 ml of tetrahydrofuran (THF, Fluka, ≥99.5%) yielding a colorless and completely transparent sol of about 4 wt%.

3.2.1.2 Characterization

The crystallinity, particle size and particle morphology of the obtained SnO_2 nanocrystals were characterized by WAXS, TEM and AUC. Their applicability as NBBs to construct mesoporous SnO_2 will be further proven and studied in Chapter 4.

In order to investigate the reaction mechanism, the organic byproducts were identified by ^{13}C-NMR measurements after the removal of the precipitation of SnO_2 nanoparticles. The ^{13}C-NMR measurements were performed using $CDCl_3$ as solvent, under ^{1}H-BB decoupling at 100 MHz.

3.2.2 Results and Discussion

In the case of titania nanoparticle sols obtained by a similar process, the particle surface has to be functionalized with ligands in order to provide good dispersibility.[26] Here, the presence of hydrochloric acid as a side product has a positive influence on particle size and redispersibility, so that the wet precipitate can be redispersed in THF yielding a completely transparent and colorless dispersion.

The WAXS pattern of the as-synthesized tin oxide nanopowder is displayed in Figure 3.1 and corresponds to the cassiterite structure (JCPDS 41-1445) without any indication of other crystalline byproducts. By using Scherrer equation[60] from the line broadening of the (110) diffraction peak, the crystallite size of SnO_2 can be calculated to be 3.7 nm.

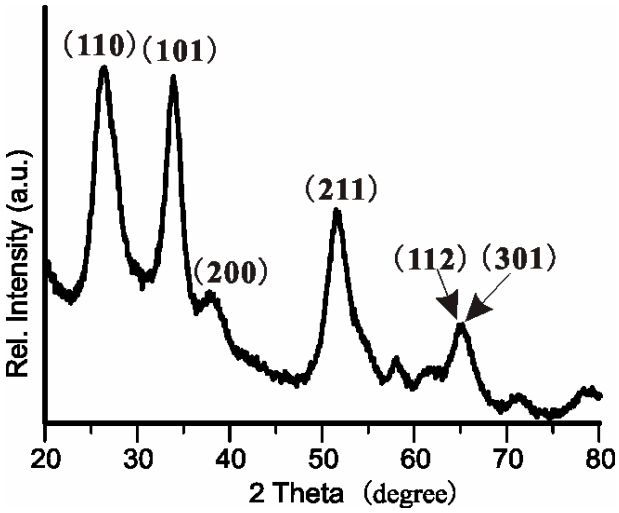

Figure 3.1 WAXS pattern of the as-synthesized SnO_2 nanopowder.

The TEM images of as-synthesized SnO_2 nanoparticles are presented in Figure 3.2. Figure 3.2a is an overview and proves that there are basically no large agglomerates existing in the SnO_2 sol and the SnO_2 nanoparticles are all well separated, although no additional stabilizing agent was added. The closer views on SnO_2 nanoparticles, Figure 3.2b and c, show that the observed agglomerates normally consist of just a few SnO_2 nanoparticles and the size of SnO_2 nanoparticles is rather uniform and in the range of 3-6 nm.

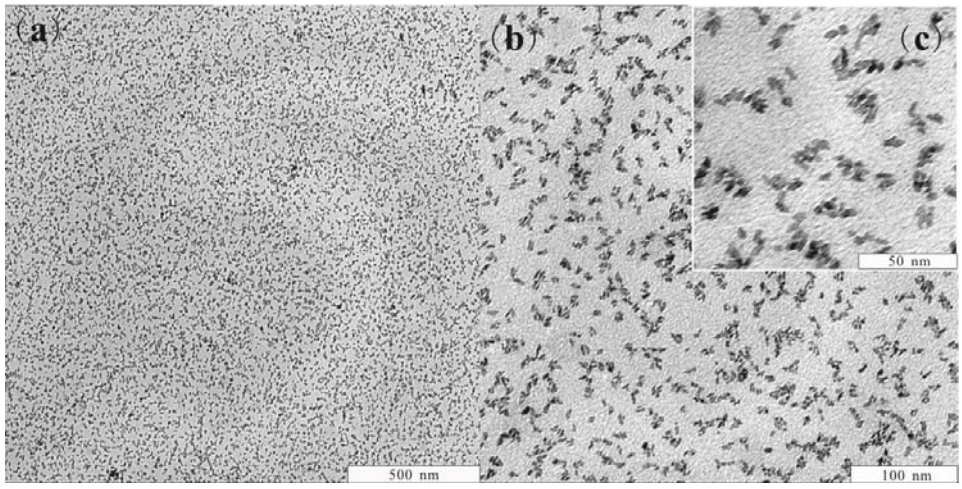

Figure 3.2 TEM images of as-synthesized SnO_2 nanoparticles at different magnifications.

The observation of the size of SnO_2 nanoparticles in TEM images and the explanation

about the presence of small agglomerations are confirmed by AUC of the nanoparticle sol in THF, which gives a particle size distribution ranging from about 2 to 5 nm, with a maximum at 3.5 nm (Figure 3.3). In contrast to TEM, AUC detects all particles of a sample with a resolution of the particle size distribution in the Ångstrom range.[61] The particle size distribution is calculated using the particle density of bulk tin oxide of 6.95 g/cm^3. Because the particle size of SnO_2 we observed in TEM images was 3-6 nm and the AUC measurement indicates that the particle size distribution in the SnO_2 sol in THF ranges from 2 to 5 nm, one is then able to deduce that the SnO_2 nanocrystals are individually dispersed in THF sol without basically any agglomeration.

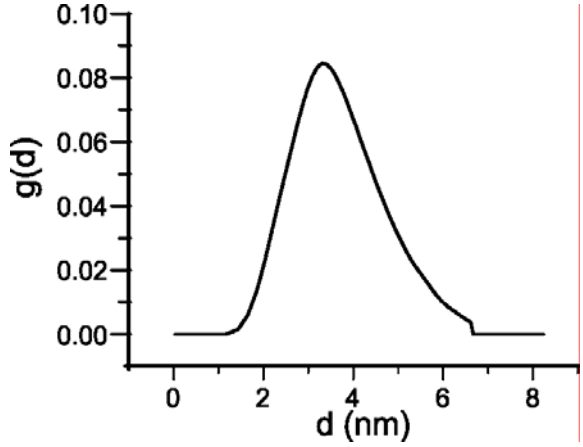

Figure 3.3 Particle size distribution obtained by AUC analysis of the as-synthesized SnO_2 nanoparticles. *d* is the diameter of the particles and *g(d)* is the differential distribution.

3.2.3 Reaction Mechanism of Nonaqueous Synthesis of SnO_2 Nanoparticles

As mentioned before, the organic byproducts of SnO_2 synthesis were identified by ^{13}C-NMR measurements. By retro-synthetical approach we are able to propose the formation mechanism of SnO_2 nanoparticles upon analyzing the processes leading to these organic species.

Interestingly, although benzyl alcohol is present as large excess in the beginning of the reaction (193.3 mmol benzyl alcohol to 8.54 mmol $SnCl_4$), it is found in the NMR

spectrum that dibenzyl ether is the byproduct having the largest amount after the reaction instead of benzyl alcohol. In contrast, only a small amount of benzyl alcohol is detected in the reaction solution, which indicates most of the benzyl alcohol has been transformed into dibenzyl ether. Besides, benzyl chloride is also found as one of the byproducts. Since dibenzyl ether, benzyl chloride and benzyl alcohol are the three main byproducts found in the solution after the synthesis of SnO_2 nanoparticles, the reaction mechanism is proposed as the following (shown in Scheme 3.1). Firstly, the chloride ligands of $SnCl_4$ are partially exchanged by benzyl alcohol, which results in the formation of Sn alkoxide and the release of HCl [Scheme 3.1 (1)]. And then, the Sn-O-Sn bond is formed upon the condensation reaction of two molecules of Sn alkoxide under elimination of dibenzyl ether [Scheme 3.1 (2)]. Another possibility to form Sn-O-Sn bond is the reaction of $SnCl_4$ and Sn alkoxide, which releases benzyl chloride [Scheme 3.1 (3)]. As I mentioned before, almost all benzyl alcohol is transformed into dibenzyl ether during the reaction. Obviously, the formation of Sn-O-Sn cannot consume so much benzyl alcohol as benzyl alcohol is more than 20 times in excess of $SnCl_4$. Therefore, it seems that the roles of $SnCl_4$ and/or SnO_2 are more than just the molecular precursor/product of the reaction and may also catalyze the ether elimination/formation, which consumes all the rest of benzyl alcohol.

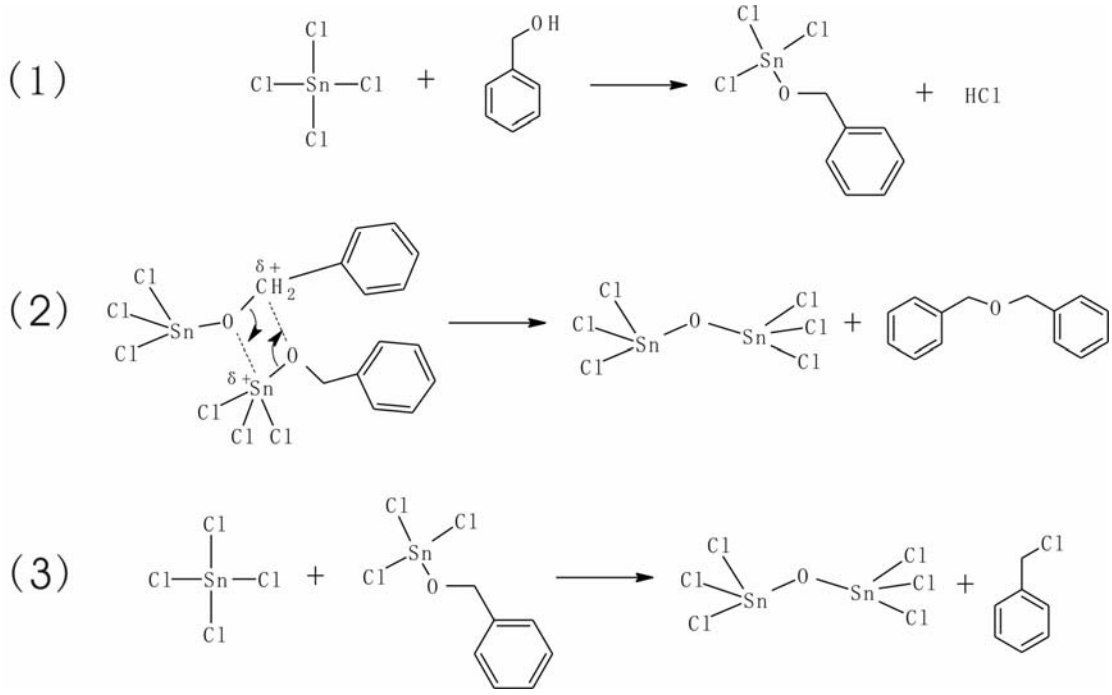

Scheme 3.1 Reaction mechanism of the Sn-O-Sn bond formation via ether elimination.

3.2.4 Conclusion

In conclusion, the nonaqueous synthesis of crystalline SnO_2 nanoparticles with a diameter of about 3.5 nm and with a narrow particle size distribution was presented. The nanoparticles can easily be transformed into a nanoparticle sol in THF without the use of any additional stabilizers, which makes them suitable building blocks for the block-copolymer-assisted preparation of crystalline mesoporous SnO_2.

The ^{13}C-NMR measurement exhibits a large amount of dibenzyl ether existing in the organic byproducts, which suggests the strong ability of molecular precursor $SnCl_4$ and/or SnO_2 nanocrystals to catalyze ether formation.

3.3 Nonaqueous and Halide-free Synthesis of Tin Doped Indium Oxide Nanocrystals

Transparent conducting oxides (TCOs) are important materials for optoelectronic

devices, because they combine optical transparency in the visible region with controllable electrical conductivity. The most widely used TCO in optoelectronics is tin-doped indium oxide (indium tin oxide, ITO).[62, 63] This material offers the best available performance in terms of conductivity and transmission, combined with excellent environmental stability, reproducibility, and good surface morphology.[64] The fastest growing application for ITO is the flat panel display technology, however, it is also the material of choice in a number of other applications,[62, 64] including functional glass,[65-68] solar cells,[69, 70] and gas sensing.[71, 72]

In the most cases, ITO is produced in form of thin films applying various methods like magnetron sputtering,[64] pulsed laser deposition,[73] chemical vapor deposition,[74] and spray pyrolysis.[75] However, these techniques are highly restricted with respect to substrate structure, substrate geometry, and cost effectiveness, and therefore liquid phase processing of ITO thin films became a widely applied alternative.[63, 76] Especially sol-gel approaches combined with deposition techniques such as spin- and dip-coating were highly successful in the preparation of ITO coatings.[77, 78] Nevertheless, in all these cases the main problem constitutes the amorphous nature of the as-deposited ITO layers and heat treatment at temperatures in the range of 400-700°C is required in order to achieve fully crystalline films.[79] A simple answer to this problem is the wet chemical deposition of dispersions containing crystalline nanoparticles.[80, 81] The work by Al-Dahoudi and Aegerter nicely illustrates the potential advantages of such processes, namely low cost and flexibility in the choice of the geometry as well as thermal stability of the substrate (i.e., allowing the use of plastic substrates).[82] However, this approach makes great demands on the properties of the ITO nanoparticles such as high electrical conductivity and high crystallinity, homogeneous composition, and uniform particle size and shape. Particle sizes below 50 nm are a prerequisite to lower the sintering temperatures and to prevent the scattering of light, so that high visible transparency is guaranteed.

There is a vast amount of literature on the synthesis of ITO nanoparticles by means of

soft chemistry approaches, mainly based on coprecipitation, often followed by hydrothermal and/or thermal treatments.[80, 83, 84] However, to the best of our knowledge the preparation of crystalline ITO nanoparticles with uniform particle shape and size in the range of about 10 nm has not yet been achieved. Recent work on the synthesis of metal oxide nanoparticles gave some strong evidence that on that small size scale nonaqueous reaction approaches are particularly successful.[18] In comparison to reactions in aqueous media, the synthesis of metal oxide nanoparticles in organic solvents provides better control over particle size, shape, crystallinity, and surface properties. However, the main advantage lies in the accessibility of highly crystalline products at moderate temperatures. This feature is strongly related to the fact that switching from aqueous sol-gel chemistry and its high reactivity of water to nonhydrolytic processes drastically decreases the reaction rates and leads to controlled crystallization. A large number of metal oxide nanoparticles have been prepared based on these routes, some of them relying on the use of surfactants as size and shape controlling agents,[85-87] some of them just taking advantage of the stabilizing effect of the organic solvents.[24, 25, 88-93]

Here I present a nonaqueous route to ITO nanoparticles with variable tin oxide content involving the solvothermal reaction of indium acetylacetonate and tin *tert*-butoxide in benzyl alcohol. The methodology is particularly attractive for several reasons: (i) all precursors are commercially available; (ii) it is a simple one pot reaction; (iii) there is by concept no contamination with halide ions; (iv) the as-synthesized nanoparticles are highly crystalline, nearly spherical in shape and with narrow size distribution; (v) the nanoparticles show good electrical conductivity without any post annealing steps.

The origin of the electrical conductivity of ITO is complicated. The optical and electrical properties of TCOs are mainly due to their defect crystal structures.[94] This is certainly true for ITO. The crystal structures of In_2O_3 and ITO are both of cubic bixbyite structure, which is shown in Figure 3.5. Each cation resides at the center of a

distorted cube, with six corners occupied by oxygen anions. The remaining two corners are empty and play an important role in the defect chemistry of ITO, as they are the location of oxygen interstitial anions (oxygen vacancies). The *b* site cation is coordinated to six oxygen anions at a distance of 2.18Å and two oxygen interstitial positions, which lie along a body diagonal of the cube. The *d* cation exhibits less symmetry, as they are coordinated to six oxygen anions at three distances (2.13, 2.19 and 2.23 Å) and to two oxygen interstitial sites along a face diagonal of the cube. Pure In_2O_3 is basically not conductive because it is an anion-deficient *n*-type semiconductor and the small oxygen vacancy population (~1% of the anions) limits the electron concentration. When a Sn^{4+} cation incorporates into the bixbyite structure by substituting an In^{3+} cation, a free electron from the Sn atom is available for electrical conduction due to the presence of oxygen vacancies in In_2O_3 crystal structure. Therefore, higher Sn-doping level, which means higher conduction electron concentration, directly induces higher conductivity of ITO. However, this principle is only correct at low Sn-doping level. If the concentration of Sn dopant is higher than certain value, the conductivity decreases because of the formation of neutral 2:1 Sn:O associates,[95] which do not contribute to the electrical conduction anymore.

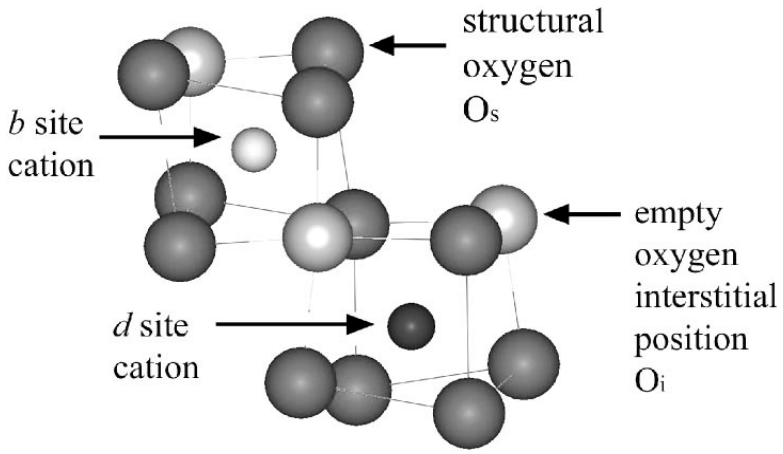

Figure 3.5 Nonequivalent cation sites in the cubic bixbyite structure.

3.3.1 Experimental

3.3.1.1 Synthesis of ITO nanoparticles

The synthesis was started in a glovebox. As a representative example, the protocol for ITO nanoparticles with 15 wt% SnO_2 is given (denoted by ITO-15). 1.53 mmol (0.6309 g) of $In(acac)_3$ (99.99+%, Sigma-Aldrich) and 0.25 mmol (0.1023 g) $Sn(O\mathit{t}Bu)_4$ (99.99+%, Sigma-Aldrich) were stirred in a glass vial with 20 ml benzyl alcohol for about 1 hour. The slightly turbid reaction mixture was transferred into the Teflon-lined steel autoclave. The autoclave was taken out of the glovebox and heated at 200°C for about 48 hours in a lab furnace. The ITO particles were collected by centrifugation, washed twice with chloroform and dried at 60°C for 12 hours in air. The yield of the as-synthesized dark blue product was about 40-45 %. The SnO_2 content was varied by changing the ratio of the two precursors from 2 wt% (ITO-2) to 30 wt% SnO_2 (ITO-30) (see Table 3.1).

In order to visualize the reaction process in the autoclave, several parallel syntheses of ITO-10 were performed together but stopped (by being removed from the furnace) after various reaction times, i.e. after 3 hours, 6 hours, 9 hours, 12 hours, 15 hours, 18 hours, 21 hours and 24 hours. These samples were then washed and collected for further characterization.

3.3.1.2 Characterizations

The as-synthesized ITO samples were characterized by various techniques including WAXS, TEM, SEM, high-resolution transmission electron microscopy (HRTEM), selected area electron diffraction (SAED), energy-dispersive X-ray (EDX) spectroscopy and X-ray photoelectron spectroscopy (XPS).

Conductivity measurements were performed on ITO pellets (13 mm in diameter) prepared from about 120 mg of powder in an evacuated press under a pressure of 10 tons. These cold-pressed pellets were directly used for the measurements without any additional thermal treatment. The pellets were contacted between the gold-plated

cylindrical electrodes (see Figure 3.6, Bürklin, 2 mm in diameter) acting both as voltage and current leads. Resistance across the pellet was measured by a digital multimeter (see Figure 3.6, Keithley Instruments, Model 2000) in a four-probe mode for eliminating the undesired resistance of measuring circuit. The specific conductivity σ was calculated from the measured resistance R as $\sigma = \delta/RS$, where S is the electrode area and δ is the pellet thickness.

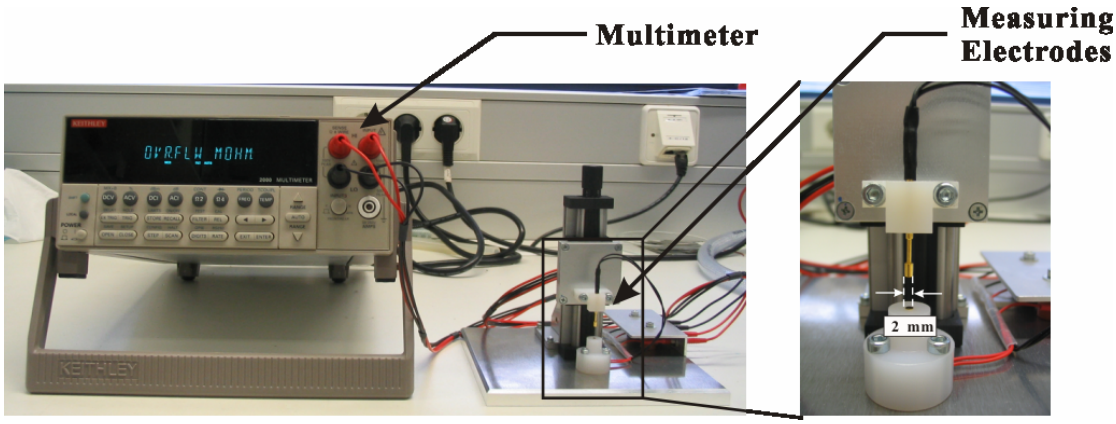

Figure 3.6 The experimental setup for the conductivity measurements of ITO pellets.

The samples which were obtained after different reaction times were studied by WAXS, TEM and HRTEM, respectively. Their conductivity was also measured.

In order to investigate the reaction mechanism of nonaqueous synthesis of ITO, the organic byproducts of ITO synthesis were identified by ^{13}C-NMR measurements after the removal of ITO particles. The ^{13}C-NMR measurements were performed using $CDCl_3$ as solvent, under ^{1}H-BB decoupling at 100 MHz.

3.3.2 Results and Discussion

3.3.2.1 As-synthesized ITO Nanoparticles

The use of benzyl alcohol as solvent has already proven to be a particularly versatile reaction medium for the nonaqueous and surfactant-free synthesis of metal oxide nanoparticles. Metal oxide precursors such as metal halides, metal alkoxides and metal acetylacetonates readily react with benzyl alcohol to the corresponding oxides. The particularity in the case of indium tin oxide lies in the simultaneous use of the

two chemically different precursors indium acetylacetonate and tin *tert*-butoxide. Obviously the reactivity of the precursors in benzyl alcohol matches each other in a way that formation of solid solution takes place, and at the same time the starting In-to-Sn ratio is closely reflected in the final composition of the ITO nanoparticles. This attractive feature enables the controlled preparation of indium tin oxide nanoparticles with varying tin oxide content over the range of 2-30 wt% (Table 3.1). The samples are named according to the starting concentrations, i.e., ITO-2 corresponds to an indium acetylacetonate-to-tin *tert*-butoxide ratio of 2 wt% SnO_2 doping in In_2O_3, ITO-6 to 6 wt% SnO_2 and so on.

Table 3.1 Electrical properties and crystallographic characteristics of the ITO nanoparticles prepared from different In-to-Sn starting ratios.

Sample No.	Starting In-to-Sn ratio (mol)	Starting SnO_2 Content (wt%)	SnO_2 Content in the Product* (wt%)	Crystallite Size# (nm)	Specific Conductivity (S/cm)
ITO-2	53.16	2	0.71	17.9	0.348
ITO-6	17.00	6	-	13.9	0.518
ITO-8	12.48	8	-	10.9	0.820
ITO-10	9.77	10	9.34	12.7	1.333
ITO-12	7.96	12	-	9.5	2.041
ITO-15	6.15	15	13.93	8.9	2.564
ITO-20	4.44	20	-	8.3	0.694
ITO-25	3.33	25	-	8.2	0.855
ITO-30	2.59	30	-	7.6	0.508

* From XPS measurements

WAXS using the Scherrer equation [(222) reflection]

Figure 3.7 displays the experimental XRD powder pattern of the ITO-15 sample (15 wt% SnO_2 according to the starting concentration) as representative example for all ITO samples. Independent of the SnO_2 content, the as-synthesized ITO nanoparticles are highly crystalline and all the diffractograms correspond to the cubic bixbyite structure of indium oxide (JCPDS, card no. 6-416) without any indication of crystalline SnO_2 as additional phase. This observation points to the formation of solid solutions rather than the mixture of indium oxide and tin oxide. The crystallite sizes of all ITO samples were determined by the Scherrer equation[60] from the line broadening of the (222) reflection and the results are summarized in Table 3.1. With increasing SnO_2 content, the crystallite sizes gradually decrease from 17.9 nm (ITO-2) to 7.6 nm (ITO-30), which clearly demonstrates the influence of the tin atoms on the formation of ITO crystallites and coincides well with the literature.[96] In this context it is interesting to recall that pure indium oxide nanoparticles obtained in benzyl alcohol exhibit a cube-like particle shape with an average side length of 20 nm.[22]

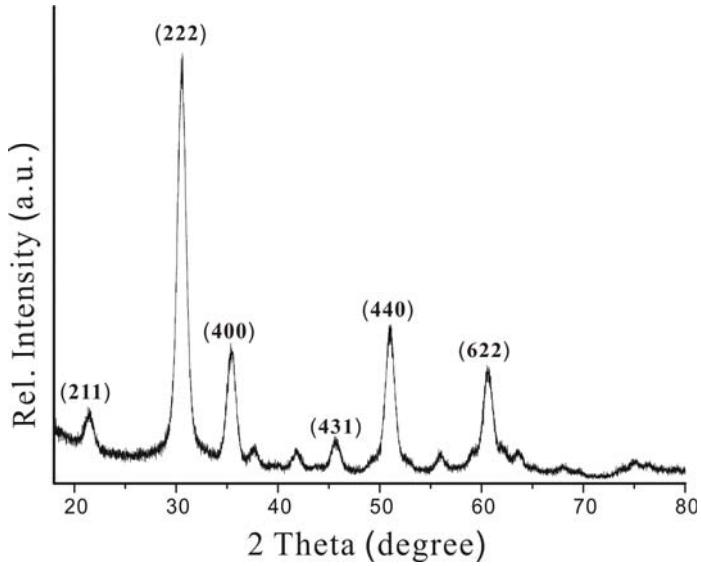

Figure 3.7 WAXS pattern of sample ITO-15.

As representative example, TEM images of sample ITO-10 are shown in Figure 3.8. An overview image (Figure 3.8a) illustrates that in addition to individual particles, also some agglomerates are present. A closer view on the area with well dispersed

particles demonstrates that the particle size distribution is in the range of 5 to 10 nm (Figure 3.8b), which is in good agreement with the crystallite sizes calculated by Scherrer equation. The particles are not only characterized by a relatively narrow particle size distribution, but also exhibit a nearly spherical and uniform particle morphology.

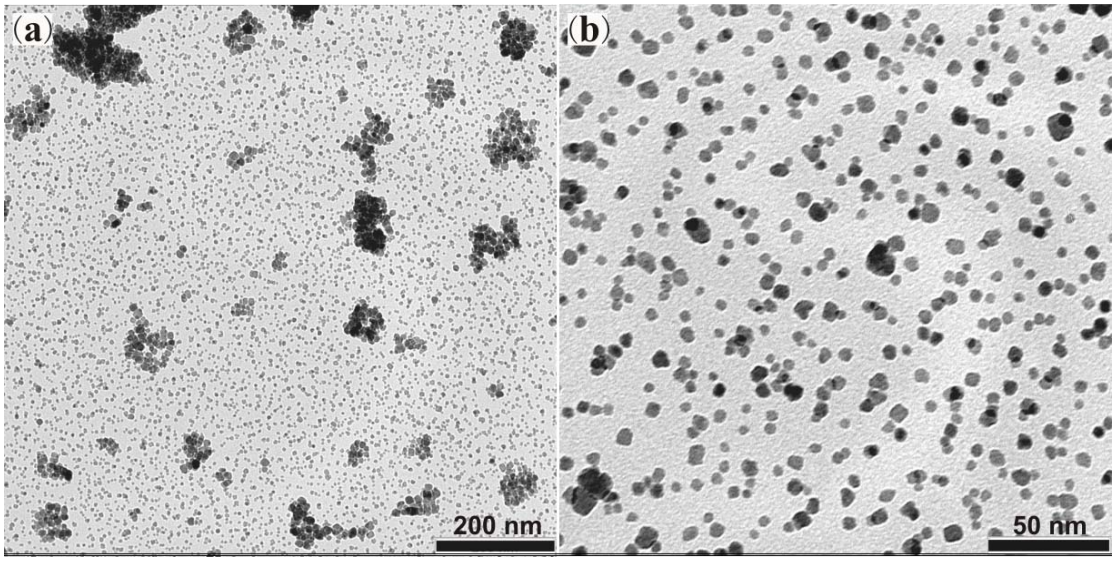

Figure 3.8 TEM overview images of sample ITO-10 at different magnifications.

Further studies on sample ITO-10 and ITO-15 by HRTEM and EDX gave additional insight into the crystal structure. Figure 3.9a depicts an SAED pattern of ITO-15 from a circular region of approximately 550 nm in diameter. The Debye-Scherrer rings clearly indicate the polycrystalline nature of the powder. The radial intensity diagram in Figure 3.9b perfectly matches the XRD pattern of sample ITO-15 (Figure 3.7) and illustrates that cubic bixbyite structure is the only crystal structure existing in the specimen. Several SAED measurements on different areas of the sample always resulted in the same SAED pattern, giving strong evidence for solid solution formation of indium oxide and tin oxide. The HRTEM images of sample ITO-10 at different magnifications are shown in Figures 3.9c and d. The well-developed lattice fringes are randomly oriented, which prove the high crystallinity of the sample and random orientation of the nanoparticles with respect to one another. The grain

boundaries are clearly visible on these HRTEM images, confirming a crystallite size of sample ITO-10 predominantly in the range from 5 to 10 nm. It is a notable feature that every particle consists of just one domain without any internal grain boundaries, which gives additional evidence for solid solution formation, but also clearly shows the single crystalline nature of every particle.

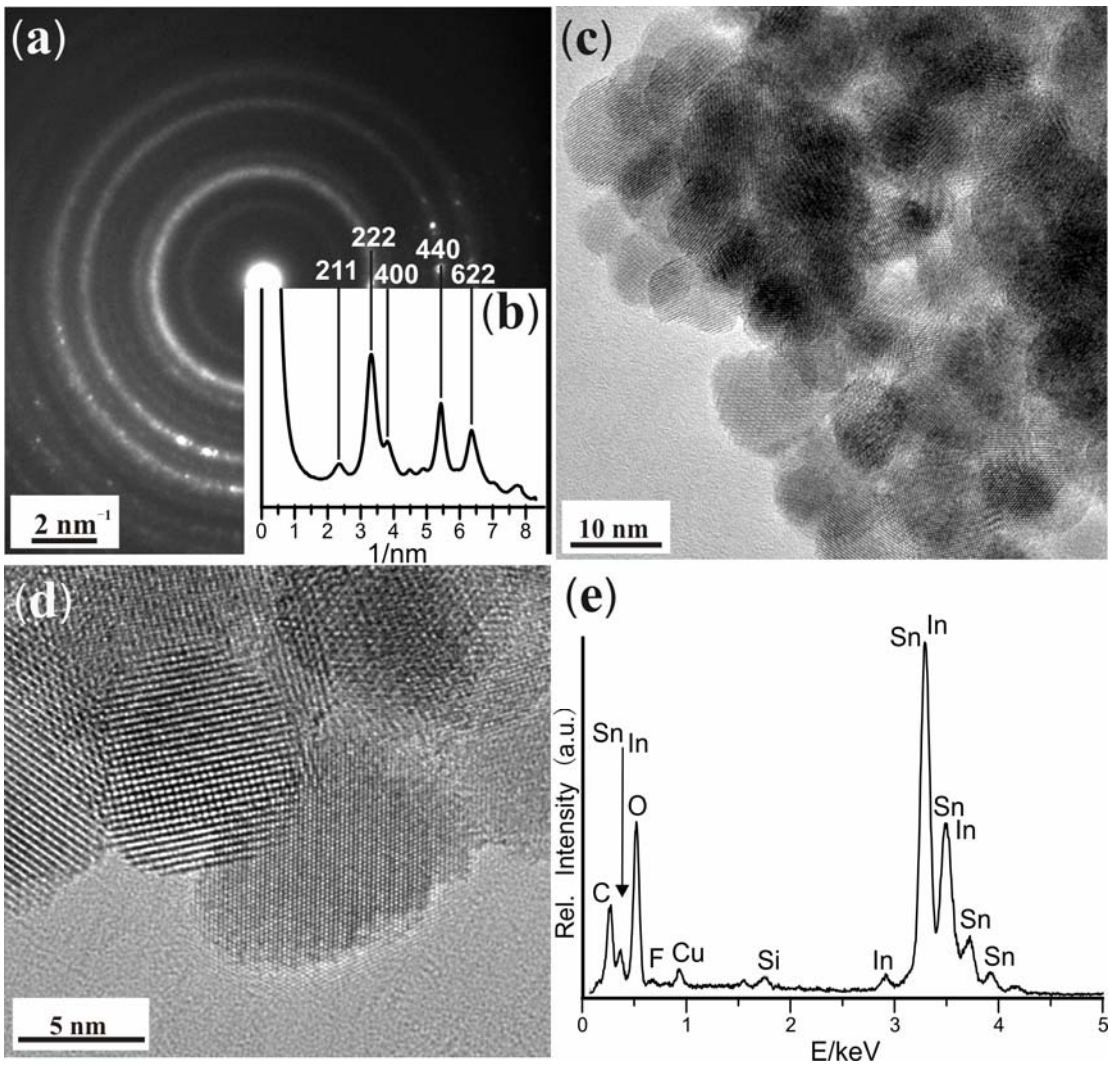

Figure 3.9 (a) SAED pattern of sample ITO-15 and (b) its corresponding radial intensity distribution, c-d) HRTEM micrographs of sample ITO-10, e) EDX spectrum of sample ITO-10.

The EDX spectrum of sample ITO-10 is presented in Figure 3.9e. Due to the closely related atomic number the peaks of indium and tin always overlap, which makes

quantitative analysis by EDX impossible. In addition to indium, tin, oxygen and carbon as main species, also copper (from the TEM grid) and traces of silicon and fluorine were detected.

In order to gain further insights into the chemical composition and into the atomic ratio of In, Sn and O in the ITO nanoparticles, the samples were analyzed by means of X-ray photoelectron spectroscopy (XPS). These measurements also provide information about the final composition of the ITO nanoparticles, i.e., the final concentration of the SnO_2 doping in In_2O_3, with respect to the starting indium acetylacetonate-to-tin *tert*-butoxide ratio, a crucial issue for synthesis planning.

As representative examples, ITO-2, ITO-10 and ITO-15 were investigated. In consideration of the fact that the usual X-ray penetration depth is about 2-3 nm at an electron take-off angle of $\theta = 45°$ and that the samples are highly homogeneous with small and uniform particle sizes, it is reasonable to regard the obtained data as characteristic for the whole specimen. Figure 3.10a shows the typical survey spectrum of ITO, which is similar for all three samples. Apart from a C1s peak positioned at 284.6 eV, which stems from carbon containing molecules adsorbed onto the nanoparticle surface (mainly benzyl alcohol and its derivatives),[97] only In, Sn and O related core levels were detected, proving the high purity of the samples. Beside the wide-scan, high-resolution spectra of the In3d (Figure 3.10b), Sn3d (Figure 3.10c), O1s and C1s regions were recorded at three different locations of every sample. Due to so-called "final-state"-effects, the In3d and Sn3d region consists of a single doublet at binding energies of 451.6 eV for $In3d_{3/2}$ and 444.1 eV for $In3d_{5/2}$, and 494.6 eV for $Sn3d_{3/2}$ and 486.1 eV for $Sn3d_{5/2}$. These values are in good agreement with literature data.[98] The positions of the In3d and Sn3d peaks as well as the symmetry of the line shape strongly point to the exclusive presence of both species in the oxidation state (III) and (IV), respectively, without any indication for the formation of metallic components. Calculations of the areas of the $In3d_{5/2}$ and $Sn3d_{5/2}$ emission lines (sensitivity factors: 4.51 for $In3d_{5/2}$, 4.89 for $Sn3d_{5/2}$) resulted in the atomic In-to-Sn

ratio of 146.1 for ITO-2, 10.53 for ITO-10 and 6.71 for ITO-15, which is generally slightly smaller as compared to the starting recipes. In the case of ITO-2, the tin concentration is close to the detection limit of XPS, which leads to a relatively large error. All these data are summarized in Table 3.1. Measurements for the estimation of the O-to-In,Sn ratio were also performed at three different positions of the samples. The acquired data for the O1s region revealed a peak with a slight hump on the high energy-side. Hence, the O1s spectrum was deconvoluted into two components at 529.6 eV and 530.7 eV, corresponding to bulk oxygen of ITO and to the OH group of benzyl alcohol on the surface of the nanoparticles, respectively. The peak analysis revealed certain oxygen sub-stoichiometry, which is indicative for the presence of oxygen vacancies. These vacancies contribute to the electron conductivity, providing the high concentration of free electrons, which also explains the dark blue color of the ITO nanoparticles.[95] The precise determination of the oxygen stoichiometry by XPS is however not possible. Investigations of the valence band structure of ITO revealed a band gap of about 3.3-3.4 eV and a slight hump at about 1.5-3 eV, which is usually correlated to the improved conductivity of ITO[99] and could provide an explanation for the good conductivity of the nanoparticles. In conclusion, the XPS investigations were indicative for the formation of chemically pure, n-type semiconductive ITO nanoparticles with SnO_2 content up to 15 wt%, which is considerably higher than the solubility limit of 6 at% reported for bulk ITO.[100]

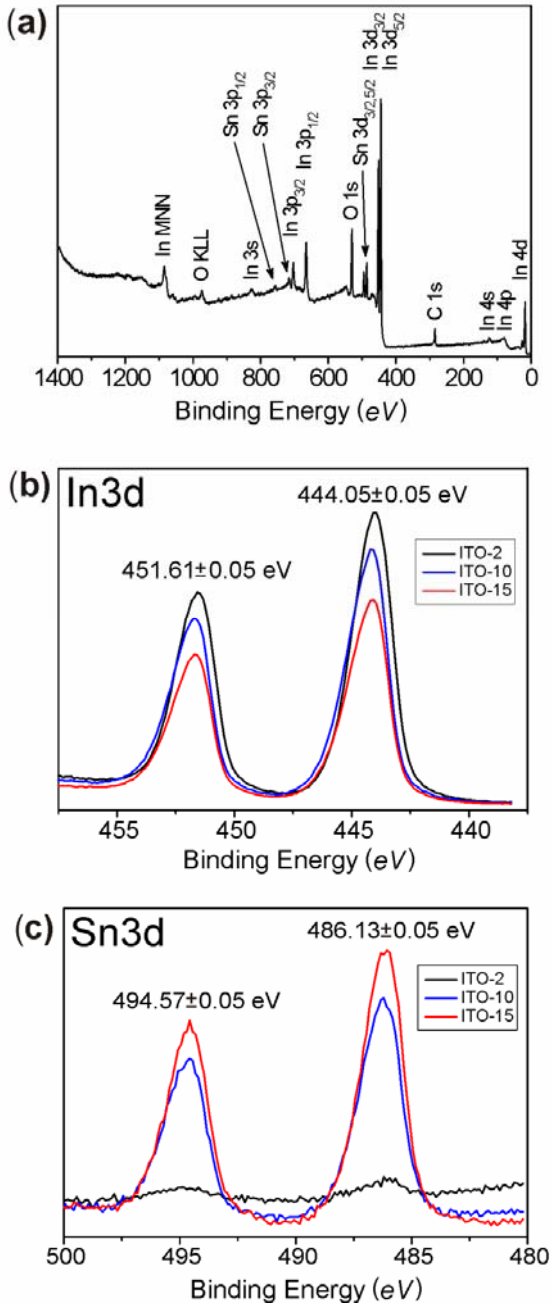

Figure 3.10 XPS investigations of ITO-2, ITO-10 and ITO-15. a) Survey spectrum (similar for all three samples), b) high-resolution In3d spectrum, c) high resolution Sn3d spectrum of the core levels.

The results of the electrical conductivity measurements performed on pelletized ITO nanopowders with different SnO_2 content are summarized in Table 3.1. Figure 3.11a represents these measurements graphically by plotting the tin oxide content (based on

the starting concentrations) versus specific conductivity. The change of conductivity is not linear, but follows a trend often observed for ITO materials.[63, 101] With increasing SnO_2 doping also the conductivity of the ITO samples gradually increases, due to the higher level of electron doping, reaching a maximum at 15 wt% of SnO_2. However, larger SnO_2 concentrations lead to a drastic drop in the conductivity of about 70-80 % compared to the maximum value. This observation is attributed to the formation of stable tin-oxygen associates for high tin doping levels, which do not contribute to the electrical conduction.[75, 79, 94, 102-104] Since all our ITO samples are highly crystalline, the change in the electrical properties of the various samples is mainly a consequence of the variation of the electron doping level in their lattice, and not of the degree of crystallinity. However, grain boundary and sintering effects stemming from different crystal sizes cannot be excluded. One has to note that the optimum Sn doping level of 15 wt% associated with the maximum conductivity is higher than the majority of the values reported in literature for ITO. Apart from some exceptions (e.g., 17 wt% of SnO_2 in ITO films prepared by the evaporation technique[71]) the optimum SnO_2 content was generally reported to be in the range of 5-12 wt%, depending on the preparation method and preparation conditions.[105-107] The higher optimum SnO_2 level in ITO nanoparticles prepared by our method might indicate the larger solubility and better distribution of tin in the indium oxide matrix compared to the conventionally prepared ITO materials. This feature is usually attributed to the non-equilibrium preparation conditions that prevent tin from forming a segregate oxide phase,[102] in contrast to the materials prepared by the traditional powder route. In comparison to commercially available ITO powders (Sigma-Aldrich, 10 wt% SnO_2, 25-45 nm mean particle size) measured under similar conditions, the conductivity of our ITO samples is almost an order of magnitude higher. Figure 3.11a shows that the two samples with 10 wt % SnO_2 exhibit a conductivity of 1.33 S/cm for our solvothermally prepared ITO and 0.15 S/cm for the commercial one. As mentioned before, the blue color of the nanoparticles points to the presence of a high concentration of charge carriers in the conduction band,[108] generated both by oxygen vacancies and by reduction of donor Sn species under removal of interstitial oxygen

ions. This observation is additionally confirmed by the fact that annealing of the ITO pellets in air at 600°C leads to a slight decrease in conductivity due to saturation of the oxygen vacancies and oxidation of activated donor species, leveling the expected improvement in conductivity due to sintering of the particle and decreasing of the grain boundary effects. In contrast, the conductivity of the pellets prepared from commercially available ITO powder increases after similar treatment.

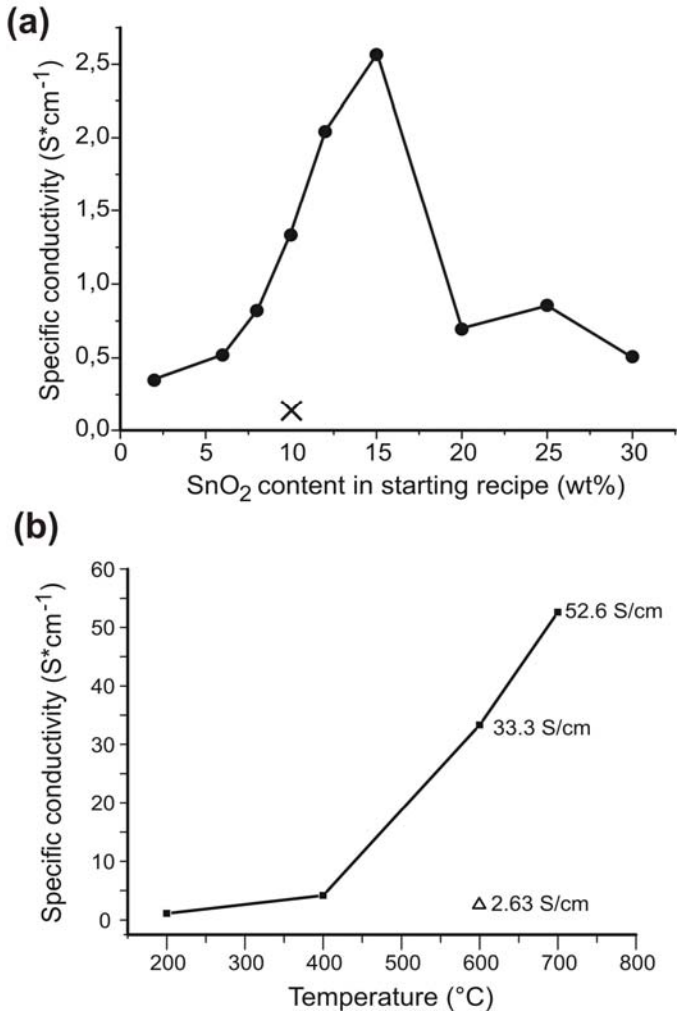

Figure 3.11 (a) Specific conductivity of the solvothermally prepared ITO nanopowders in dependence on the initial Sn content, together with commercially available ITO nanopowders (Aldrich, 10 wt % SnO_2) as comparison (cross). (b) Diagram of specific conductivity of sintered ITO nanopowders under nitrogen versus sintering temperature, together with ITO nanopowders sintered under air as comparison (triangle).

In order to further probe the influence of post thermal treatments on the conductivity of the ITO powders, the pellets of sample ITO-15 were sintered at 200°C, 400°C, 600°C and 700°C for two hours under nitrogen. We found that the conductivity of ITO-15 increased after high temperature (400°C, 600°C and 700°C) sintering while decreased or remains constant after the sintering at 200°C (see Figure 3.11b). Particularly, the conductivity increased dramatically from 2.56 S/cm to 52.6 S/cm (20 times higher), which indicates the good potential to enhance the conductivity of our ITO pellets. The conductivity changes of ITO-15 are presented in Figure 3.11b by plotting the specific conductivity versus temperature. The conductivity of ITO-15 sintered at 600°C under oxygen is also marked as a triangle.

In the case of using inert gas such as nitrogen, the thermal treatment has a positive impact on the conductivity of the ITO pellets. It enhances the mechanical contact between the nanoparticles, the growth of the crystallites and the decrease of the grain boundaries. If oxygen is used instead of inert gas, the oxygen vacancies in the crystal structure of ITO are saturated and the concentration of the free charge carriers are therefore reduced, which counteract the positive effect of sintering at high temperature. This explains why the conductivity of ITO samples decreased after being annealed at 600°C under oxygen.

The maximum conductivity of 2.56 S/cm for 15 wt% SnO_2, however, is still far below the reported values of up to $1 \cdot 10^4$ S/cm for the dense epitaxially grown ITO films.[64] The main reason for the lower conductivity lies in the charge scattering on the grain boundary contacts between the nanoparticles. One has to keep in mind that the measurements were performed on the as-synthesized powders without thermal treatment. Therefore, the values obtained should be considered as the apparent conductivity of the particle ensemble and they are expected to be much lower than the real bulk conductivity of the ITO lattice of a single particle. Because just the mixture of indium and tin oxides as separated phases is not conductive, the good conductivity of the ITO samples strongly confirms the presence of solid solution formation.

As the main application of ITO, the conductive films made of ITO attract the most interests. In order to probe the possibility to make conductive films using our solvothermally synthesized ITO nanoparticles, I prepared some ITO films by both dip coating and simply casting the ITO suspension of ethanol on glass wafers. However, the conductivity measurements proved that the films are not conductive. The reason is that, in contrast to the dense films made by other techniques, such as magnetron sputtering or chemical vapor deposition, the films made by dip coating or casting are so loose that the ITO nanoparticles are not in close contact with each other, which make it impossible for the electrons to find a continuous pathway to go through the film. The very loose surface morphology has been proven by the SEM images shown in Figure 3.12a and b. As a comparison, the surface morphology of the compressed pellet of ITO nanoparticles is shown in Figure 3.12c. One can see that the ITO pellet is much denser than the film, which makes it much more conductive than the films made by dip coating or casting. One of the possible solutions to make dense films is to functionalize the surface of the ITO nanoparticles by surfactants or ligands to achieve high dispersibility without formation of large agglomerates. However, this is out of the scope of the thesis.

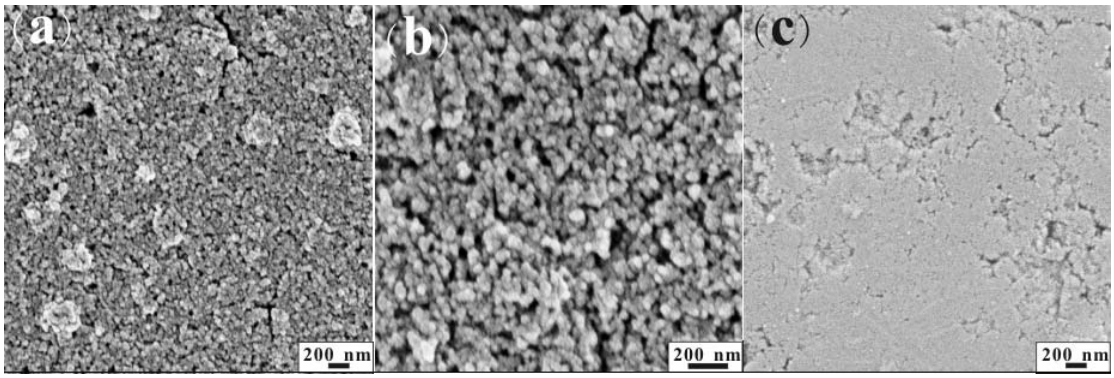

Figure 3.12 (a), (b) SEM images of ITO films made by casting ITO suspension of ethanol on glass wafer; (c) SEM image of surface morphology of the compressed ITO pellet.

3.3.2.2 ITO Nanoparticles in dependence on the reaction time

In order to visualize the crystal structure transformation, the morphology as well as the conductivity change of ITO nanoparticles depending on the reaction time, various samples of ITO-10 were synthesized with reaction times in the range of 3-24 hours in 3-hours steps, i.e. 3 hours, 6 hours, 9 hours and so forth, and these products were studied by WAXS, TEM and HRTEM. The samples are named according to their reaction times, i.e., ITO-3H corresponds to the product after 3 hours reaction, ITO-24H corresponds to the product after 24 hours reaction, and so on. The results were surprising. Great changes were observed in crystal structure, particle morphology and conductivity of the as-synthesized ITO nanoparticles at different reaction times.

The WAXS patterns of ITO samples after different reaction times are plotted in the same diagram and presented in Figure 3.13, in which an evolution of WAXS patterns from an ITO precursor species to real ITO nanoparticles can be clearly seen. Firstly, after 3 hours, a pattern with the most intense reflection peak located at 2θ=34.8° is observed. However, this pattern cannot be assigned to any crystal structures of In_2O_3 or SnO_2. Latter analyses on the WAXS patterns indicated that sample ITO-3H has a meta-stable crystal structure, which presumably is structurally related to the cubic bixbyite structure of ITO. The conductivity measurement on ITO-3H indicates that the product is not conductive. However, after being sintered at 500°C for 2 hours, the WAXS pattern of the powder completely transformed into the typical pattern of ITO (data not shown) and the powder became conductive. This fact indicates that all the "ingredients" needed to form ITO nanoparticles as well as the right cubic bixbyite phase have been already incorporated into the precursor material formed after 3-hours reaction. The rest of the reaction is basically the transformation of the unidentified precursor material to real ITO. TGA measurement was also performed on ITO-3H and indicates that the mass loss of the as-synthesized powders is ~20 wt% up to 500°C, which means that there are some organic compounds incorporated into the powder.

With increasing reaction time, the relative intensity of the most intense peak in the pattern of ITO-3H decreases in the pattern of ITO-6H and a peak arises at 2θ=30.5°, which was not observed in the pattern of ITO-3H and seems to be the embryo of the (222) reflection of ITO. In the pattern of ITO-9H, no great change is observed. The intensity of the peak at 2θ=30.5° increases continuously. Besides, a tiny peak also appears in the pattern of ITO-6H and is possibly the embryonic form of the (440) reflection. When the reaction was carried out for 12 hours, the WAXS pattern doesn't change much. The only apparent difference between the patterns of ITO-6H and ITO-12H is that, for the first time, the embryonic peak of the (222) reflection of ITO becomes more intense than the peak at 2θ=34.8°, however the conductivity measurement indicates that the product is not conductive yet.

Great changes happen in the WAXS pattern of sample ITO-15H. Different from the previous patterns, the pattern of ITO-15H is very similar to the pattern of ITO-10 shown in Figure 3.7 including relative intensities and shapes of the peaks. All the main reflection peaks of ITO, such as (222), (200), (440), (622) and (211) reflections, can be clearly seen in the pattern of ITO-15H. The (222) reflection peak becomes much more intense and sharper in comparison to the pattern of ITO-12H. The (440) and (622) reflections also become very intense and sharp rather than the tiny peaks seen in the patterns of ITO-6H and ITO-12H. The reflection of (211), which is invisible before, arises after 15 hours of reaction. One of the two main peaks in the pattern of ITO-3H, located at 2θ=25.3°, which is also present in the patterns of ITO-3H and ITO-12H, almost completely vanish in the pattern of ITO-15H indicating a dramatic phase transformation in the crystal structure of ITO. Moreover, the crystallite size of ITO-15H is almost 3 nm larger than ITO-12H, which is a steep increase in the crystallite size (see Table 3.2). All these phenomena illustrate that the crystal structure transformation from the meta-stable phase to the cubic bixbyite structure has been basically completed after 15 hours of reaction. The only indication of the presence of the former meta-stable crystal structure is the tiny peak at 2θ=43.6°, which is much less intense than in the previous patterns. In addition to the WAXS data,

the conductivity measurement on sample ITO-15H shows that it is conductive, although its conductivity of ~0.75 S/cm is lower than the one of ITO-10. All the aforementioned observations indicate that significant changes in terms of both crystal structure and electrical conductivity occur in between the reaction time of 12 and 15 hours. One can also conclude that cubic bixbyite structure is the exclusive crystal structure responsible for the electrical conductivity in this reaction system. When and only when the cubic bixbyite structure becomes the major crystal structure, the obtained powders can exhibit electrical conductivity.

No considerable change was observed in the pattern of ITO-18H comparing with the pattern of ITO-15H. The only indication of the small amount of the meta-stable phase present in the pattern of ITO-15H, the peak at 2θ=43.6°, completely disappears in the pattern of ITO-18H, which indicates that all phases have been completely transformed into bixbyite structure. Besides, the intensity of the (440) reflection becomes higher than the reflection of the (200) one. All these changes match the pattern of ITO-18H perfectly with the pattern of ITO-10, indicating that the chemical reaction towards tin-doped indium oxide has been nearly finished after 18-hours reaction. The patterns of ITO-21H and ITO-24H further confirm above conclusion because no apparent change is observed anymore.

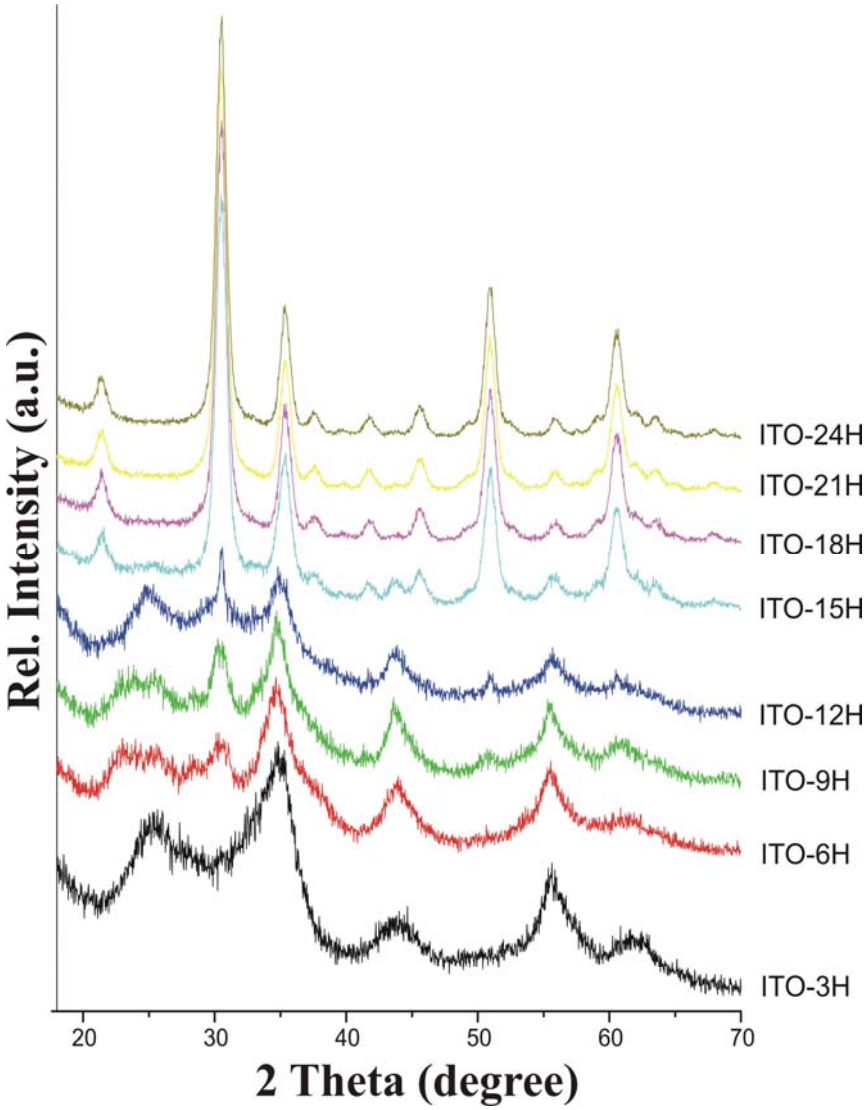

Figure 3.13 WAXS patterns of ITO samples after different reaction times.

The crystallite sizes at different reaction times are calculated by the Scherrer equation and recorded in Table 3.2. According to the data in Table 3.2, a diagram is plotted and shown in Figure 3.14. Obviously, the crystallites grow rapidly in the first 15 hours of the reaction with a growth rate of around 0.2 nm per hour. And then, the growth rate is strongly decreased after the transformation into cubic bixbyite structure (0.1 nm per hour). This significant difference of crystallite growth rate after 15 hours of reaction demonstrates that crucial changes occur in between 12 and 15 hours of reaction, which well fit the conclusions from the crystal structure analysis.

Table 3.2 The increase of the crystallite size of ITO-10 in dependence on the reaction time.

Sample No.	Crystallite Size (nm)*
ITO-3H	3.11
ITO-6H	4.40
ITO-9H	5.98
ITO-12H	6.22
ITO-15H	9.24
ITO-18H	9.53
ITO-21H	9.83
ITO-24H	10.16
ITO-10	12.7

* WAXS using the Scherrer equation [the peak at 2θ=43.6° for ITO-3H, 6H, 9H, 12H and (222) reflection for ITO-15H, 18H, 21H, 24H]

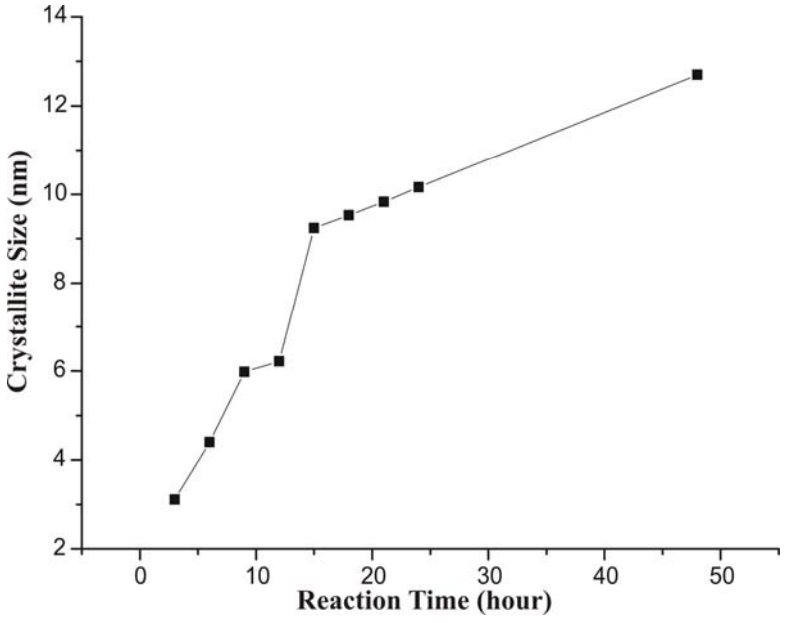

Figure 3.14 The increase of crystallite size of ITO-10 in dependence on reaction time.

The TEM images of sample ITO-3H, 6H, 9H, 12H and 24H are presented in Figure 3.15. As one can expect, a great difference is also observed regarding the particle

morphology.

The morphology of sample ITO-3H in the electron microscope is surprising. Instead of nanoparticles, many elongated sheet-like ribbons are observed (Figure3.15 a1). They are about a few hundreds of nanometers in width and close to 1 micrometer in length, which is extremely large comparing with the crystallite size calculated from the WAXS pattern (3.11 nm). From the observations in Figure 3.15 (a1) and (a2), one may deduce that those ribbons consist of many nanocrystals oriented in the direction perpendicular to the elongated one. However, Figure 3.15 (a3) and (a4) demonstrate that the orientations of the nanocrystals are completely random without any preferences. This indicates that the WAXS pattern of ITO-3H (shown in Figure 3.13) is reliable to be used as an indication of its polycrystallinity, which is also proven by the Debye-Scherrer rings present in the SAED pattern of ITO-3H (data not shown). Most of the crystallites seen in Figure 3.15 (a3) and (a4) are quite small and in the size of less than 5 nm, which perfectly matches the crystallite size calculated from its WAXS pattern (3.11 nm). The partially broken, partially connected morphology of the ribbons might be due to the presence of a lot of organic compounds in between the “rows” formed by the nanocrystals. The organics physically function as the glue, which sticks the nanocrystals together and extends the sheet-like morphology of the ribbons into the micrometer scale.

Since the nanocrystals are randomly oriented, the question arises why all the ribbons are only elongated in one specific direction rather than in all the directions? The observations in the TEM images of sample ITO-6H (Figure3.15 b) offer us more perspectives on the morphology evolution of ITO nanoparticles and might answer this question. In Figure 3.15 (b), two kinds of morphologies, elongated (b1) and non-elongated (b2) sheet-like ribbons, are observed. My argument is that the non-elongated morphology of the ribbons is their original state before centrifugation and washing procedure. Their elongated morphology is mainly induced mechanically and should not be considered as the initial morphology of the formation of ITO

nanoparticles. Figure 3.15 (b3) and (b4) nicely show the alignment of the nanocrystals in the huge ribbons. Particularly, Figure 3.15 (b4) demonstrates that the nanocrystals align in the rows with completely random orientations, with crystallite sizes are around 5 nm. And the area in between each row formed by the nanocrystals is probably where the organics are and approximate 3±1 nm in width. Obviously, the cohesion of the organic part is the weakest area of this hybrid material. Once external mechanical forces are applied, the organic adhesion can be easily broken along the direction of the nanocrystals alignments and induce the partially disconnected elongated morphology in large scale.

Figure 3.15 (c), (d) and (e) are indeed demonstrating the evolution from sheet-like ribbons to individual separated nanoparticles. With the increase of the reaction time, the huge sheet-like ribbons are completely broken up (Figure 3.15 c, d) and finally vanish (Figure 3.15 e), which enables the formation of much smaller nanoparticles. The shape of the nanocrystals is firstly irregular (Figure 3.15c4) and then becomes more cubic (Figure 3.15 d4) accompanied by a growth of the crystallites. When the reaction is further going on, the nanocrystals become more and more spherical (Figure 3.15 e4) and finally end up with the shape and size that was observed in Figure 3.9. It's also noticeable that the conductivity of the product cannot be detected as long as the alignments of the nanocrystals still exist (Figure 3.15 d2). Similarly, the cubic bixbyite phase is not visible in the WAXS pattern until the sheet-like morphology has completely disappeared.

Assuming that every nanocrystal in the hybrid ribbon structure consists of an inorganic crystalline core coated by an organic shell (mainly benzyl alcohol), the thickness of the organic shell is approximately 8Å (the size of the benzyl alcohol molecule). In the case of sample ITO-3H, its crystallite size is 3.11 nm and the volume fraction of the inorganic core is calculated to be less than 30 %. This means that the features of the nanocrystals of ITO-3H are mainly dominated by the organic coating on the inorganic core and they behave more like organic components rather

than inorganic particles, which explains why they form 2D sheet-like structures instead of individual inorganic particles. In contrast, the volume fraction of the inorganic core of sample ITO-24H is around 65 %, which means that the inorganic core dominates the morphology of the hybrid material. In addition, the extremely small nanocrystals (3.11 nm) of ITO-3H have much higher mobility to be manipulated to form a well-structured hybrid material than the large nanocrystals of ITO-24H (10.16 nm), in which the sheet-like morphology disappears.

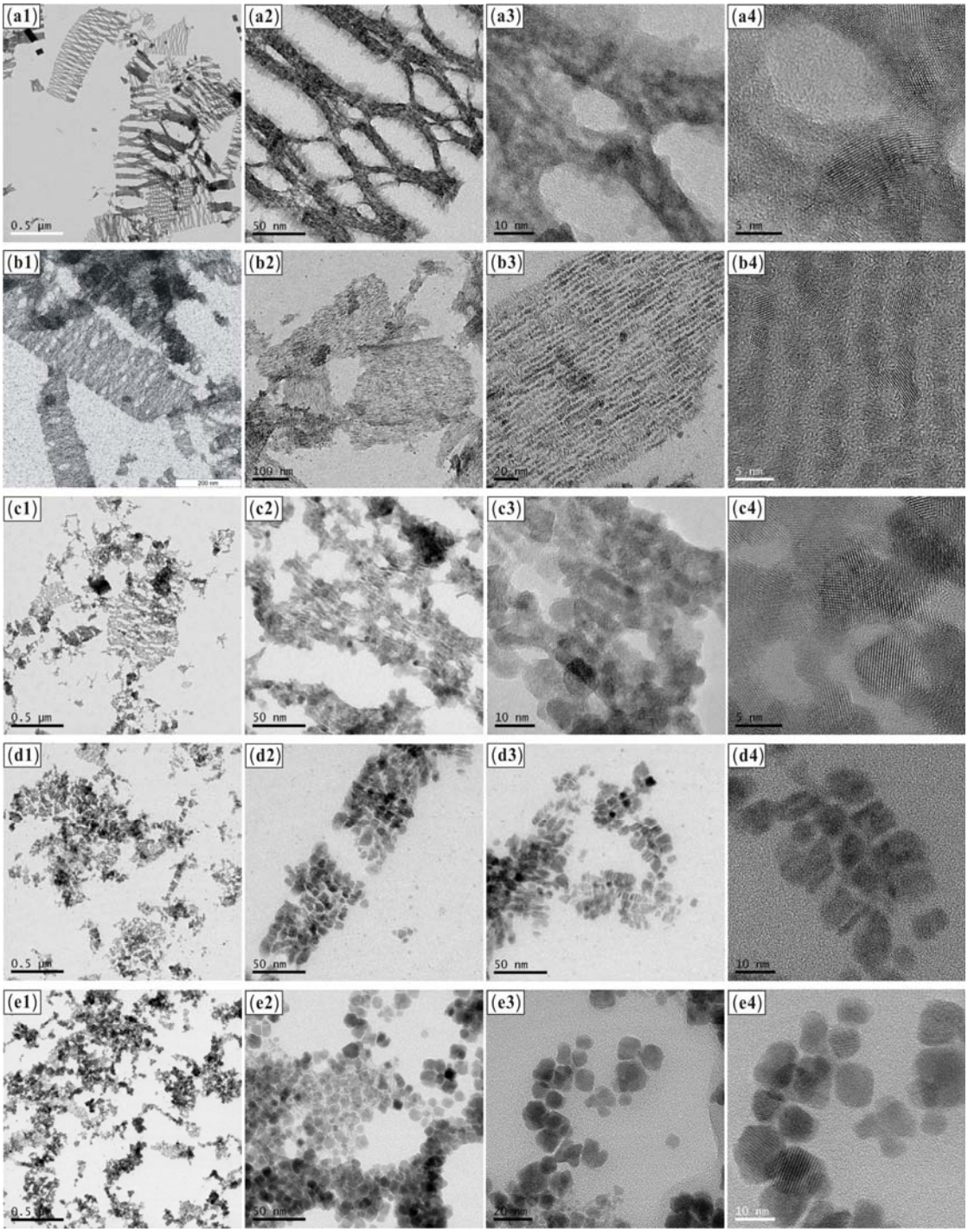

Figure 3.15 TEM and HRTEM images of sample ITO-3H (a), ITO-6H (b), ITO-9H (c), ITO-12H (d) and ITO-24H (e).

Sample ITO-3H was also investigated by SEM. The images are shown in Figure 3.16. Its morphology is very similar to what was observed on the TEM images (Figure 3.15 a). There are both large agglomerates and many broken small pieces present in the

images. And for the large agglomerates, their sizes basically fit the observation from the TEM images, which are a few hundreds of nanometers to one micrometer in width. However, different from the TEM images, one can only see rod-like aggregates instead of the elongated and partially-disconnected ribbons present in the TEM images. This is mainly due to the different preparation procedures for TEM and SEM specimens. For the TEM measurement, organic solvents, such as ethanol, were used to disperse the sample, which well preserved the original morphology of ITO-3H. In contrast, the SEM specimen was simply prepared from dried and ground powders. That is the reason for the formation of the rod-like aggregates and gives an explanation why the size of the agglomerates is so irregular.

Furthermore, similar to the TEM images of ITO-3H (Figure 3.15 a), there are basically no individual nanoparticles observed in the SEM images and only large and small pieces of rod-like agglomerates can be seen. This points to directionally aligned nanoparticles, which might form supercrystals and confirms that the sheet-like ribbons are the only morphology of the product after 3 hours of reaction.

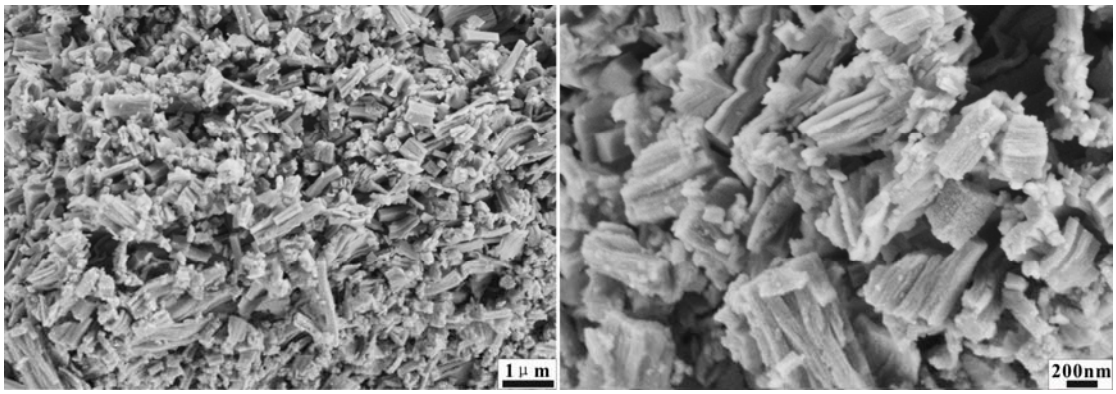

Figure 3.16 SEM images of sample ITO-3H with different resolutions.

3.3.3 Reaction Mechanism of Nonaqueous Synthesis of ITO Nanoparticles

Similar to the reaction mechanism analysis of SnO_2, retro-synthetical approach was also used to study the formation mechanism of ITO nanoparticles upon the identification of the organic byproducts of ITO synthesis by ^{13}C-NMR measurement.

Upon the ^{13}C-NMR measurement, benzyl acetate, 2-methyl-4-phenyl-2-butanol and 4,4-dimethyl-2-pentanone were identified as the main reaction products. The reaction mechanism of ITO synthesis is proposed as the following (shown in Scheme 3.2). Benzyl alcohol attacks one carbonyl group of the acetylacetonates ligand (1). Alcoholysis leads to benzyl acetate and an enolate ligand coordinate to the In center (2). And then, benzyl alcohol coordinate to the In center and benzyl acetate is released in a ligand exchange reaction. This is where benzyl acetate comes from. The resulting compound then attacks tin-*tert*-butoxide (3) and a typical aldol coupling happens (4), which results in 4,4-dimethylpentanone and $(O\textit{t}Bu)_3Sn$-OH. The latter resultant is cable for further condensation reaction to form Sn-O-Sn or Sn-O-In bonds. Because the exact reaction mechanism is highly complex and still under investigation, further details are out of the scope of the present thesis.

2-Methyl-4-phenyl-2-butanol is the product of a side mechanism that involves a C-C coupling reaction as what was observed in earlier publications by Niederberger et al.[28] The reaction mechanism is shown in Scheme 3.2 (3).

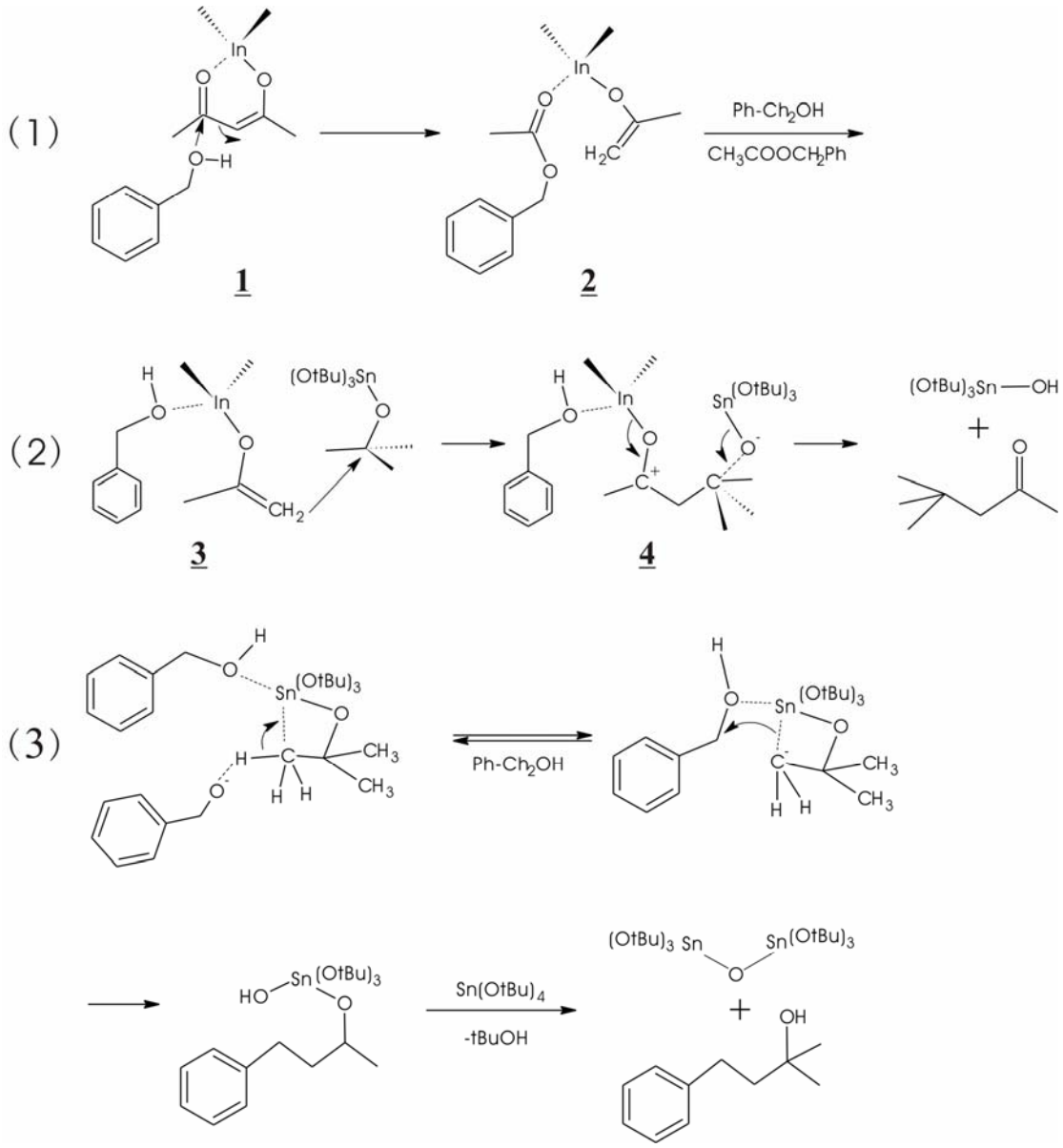

Scheme 3.2 Main reactions occurring during nonaqueous synthesis of ITO nanoparticles in benzyl alcohol.

3.3.4 Conclusion

The solvothermal reaction between indium acetylacetonate and tin *tert*-butoxide in benzyl alcohol provides a comfortable nonaqueous route to crystalline ITO nanoparticles with uniform spherical shape and sizes in the range of 5-10 nm. The simple variation of the tin oxide content from 2-30 wt% enables the preparation of this transparent conducting oxide with a maximum electrical conductivity at a doping level of 15 wt% of 2.56 S/cm, which is one order of magnitude higher than for

commercially available nanopowders. The electrical conductivity of solvothermally synthesized ITO nanoparticles can be much impoved by sintering the particles under nitrogen. The conductivity of ITO-15 sintered at 700°C under nitrogen was determined to be 52.6 S/cm.

By studying the products obtained after different reaction times, a crystal structure transformation from an unknown structure to cubic bixbyite structure was observed. Furthermore, TEM and HRTEM images of samples obtained after different reaction times present the morphological transformation from sheet-like ribbons consisting of randomly oriented nanocrystals alignments to spherical ITO nanoparticles. These investigations offer the chance to monitor the morphological pathway to the formation of ITO nanoparticles.

The reaction mechanism of this nonaqueous synthesis of ITO in benzyl alcohol was also proposed.

3.4 Experiments towards the Solvothermal Synthesis of YBCO Superconductor

The phenomenon that the electrical resistivity of some compounds drops suddenly to zero when the specimen is cooled to a sufficiently low temperature is called superconductivity. It was first discovered in mercury metal by Kamerlingh Onnes in Leiden in 1911. The critical temperature (T_c) at which mercury becomes superconducting is 4.1 K. Subsequently, other materials, mainly metallic elements and alloys, were discovered to be superconducting. A slow and steady rise of T_c took place, resulting in a T_c of 23 K for Nb_3Ge in 1975.[109] However, this T_c is still far away from the temperature necessary for the superconductors to be really applicable and it was predicted theoretically that T_c would never be higher than 30K. A breakthrough occurred in 1986 when Bednorz and Müller published their historic paper in Zeitschrift für Physik, announcing their discovery of a lanthanum-based cuprate perovskite material, which had a transition temperature of 35 K. Shortly later in early

1987 it was found that replacing the lanthanum with yttrium, i.e. making $YBa_2Cu_3O_7$, raised the critical temperature to 92 K. This is certainly marked as a milestone of high temperature superconductors (HTS) investigation and opened a new era of the science of superconductors. Since 1994, HTSs started showing their good potential in pre-commercial applications, such as thin films, wires, levitated vehicles, etc.

The material with most research behind HTSs is $YBa_2Cu_3O_7$, which is abbreviated as YBCO or Y-123. The crystal structure of YBCO (shown in Figure 3.17) is an oxygen-defect modification of the perovskite structure. The primitive cell is developed from a tetragonal perovskite tripled along the *c* axis. Per formula unit of $YBa_2Cu_3O_7$, the positive ion valencies based on Y^{+3}, Ba^{+2}, Cu^{+2} are 13 and the negative (oxygen) valency is –14. Therefore, there is one excess charge carrier in YBCO structure, which is necessary for its superconductivity. It is know that parallel sheets of CuO_2 are a structural feature of all HTSs with T_c>40 K. In YBCO crystal structure shown in Figure 3.17, the CuO_2 planes are parallel to the plane of the *ab* axes in the orthorhombic primitive cell. Two of these planes, those through the interior of the cell, are the dominant conducting pathways. The oxygen content per cell can be changed reversibly from 7.0 to 6.0 atoms by pumping oxygen in and out of the parallel chains of CuO that run along the *b* axis of the figure. It's interesting to note that, at the composition of $YBa_2Cu_3O_6$, the crystal is an insulator; however, an increase in oxygen above $O_{6.5}$ makes the crystal metallic, non-magnetic and superconducting.

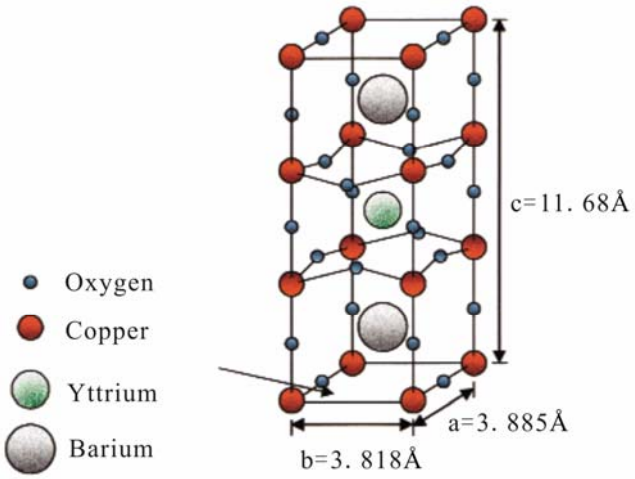

Figure 3.17 Crystal structure of YBCO.

Since the discovery of YBCO, enormous efforts have been dedicated into optimizing the methods of synthesizing YBCO, with the particular focus on reducing the sintering temperature as well as the formation of phase pure YBCO. Besides, another challenge that the scientists working on HTSs have to face is how to bring HTSs into real applications. In practical cases, the use of YBCO very much depends upon the ability to sinter powders of this material into strong dense compacts. Because sintering is driven by a decrease in surface free energy, good sinterability requires a powder comprised of small particles. In addition, it is particularly difficult to make superconducting wires several meters long with YBCO[110] due to its mechanical properties, which completely blocks the possibility to make superconducting wires with YBCO, which is one of the major applications of superconductors. One solution is to deposit YBCO powders on single- or multi-layer tapes. Very fine YBCO powders are also important here for post sintering process so as to remove the grain boundaries between YBCO particles and form continuous superconducting YBCO layer. From both aforementioned points of view, it's favorable for the utilizations of YBCO to minimize the size of YBCO particles. However, this mission still remains extremely difficult.

One of the main techniques used to synthesize YBCO powders is solid state chemistry.

Typically, the precursor of YBCO, a fine mixture containing yttrium, barium and copper compounds, e.g. oxides, is sintered at high temperature (around 900°C) under inert gas to obtain single phase YBCO. And then, the mixture is further annealed under air or oxygen for one or two days to enrich the oxygen content so that $YBa_2Cu_3O_x$ ($x>6.5$) is surely formed. Similar to other solid state reactions, the drawbacks of this method to synthesize YBCO are long and complicated high temperature processes, complicated reaction mechanisms, high efforts to avoid impurities, which strongly impact the superconducting properties of YBCO, and great difficulties to control particle size, morphology and size distribution. Besides solid state chemistry routes, some thin-film techniques were also used to synthesize YBCO particles. But those techniques are rather expensive and not applicable for large scale synthesis. Similar to other stories of making metal oxide fine particles, sol-gel chemistry including both aqueous and nonaqueous sol-gel process was thereby introduced to synthesize YBCO powders. Conventionally, aqueous sol-gel methods are frequently used. Yet, no matter if there is water involved in the reaction, sintering process is unavoidable to achieve the correct crystal structure of YBCO, which makes the control of particle size, morphology and size distribution comparably difficult, analogous to the solid state approach.

The solvothermal sol-gel approach typically using benzyl alcohol as solvent was particularly useful and versatile to synthesize various binary and ternary metal oxide nanoparticles with high purity, uniform particle morphology and narrow particle size distribution. Especially, this method shows a strong ability to synthesize ternary metal oxide nanoparticles having a perovskite structure, such as $BaTiO_3$, $SrTiO_3$, $BaZrO_3$, etc, with well controlled particle size and shape. As mentioned before, the primitive cell of YBCO is developed from a tetragonal perovskite tripled along the *c* axis (Figure 3.17). Therefore, this benzyl alcohol route might possibly offer better opportunity to synthesize the specific crystal structure of YBCO. Consequently, the aforementioned features of this solvothermal sol-gel approach inspired us to explore the possibility of fabricating YBCO nanoparticles with well controlled morphological

properties. In addition, as no synthesis approach with sintering temperature less than 600°C has ever been reported in literatures, we were also hoping to realize YBCO at rather moderate temperature upon our experience of synthesizing highly crystalline metal oxides nanoparticles at 200°C to 250°C. Even if we are not able to directly achieve YBCO nanoparticles with the correct crystal structure, we may obtain some nanoscale YBCO precursor, which could be further transformed into the right phase of YBCO after being calcined at relatively low temperature because the sintering temperature could be very much reduced by bringing the components into nanometer scale. Unfortunately, it turned out finally that all my attempts to synthesize YBCO nanoparticles by solvothermal sol-gel approach were not successful. Nevertheless, the results are summarized in here as a reference for future work.

3.4.1 Experimental

In the very beginning, following the same idea to synthesize $BaTiO_3$ nanoparticles, we also intended to use metallic barium to introduce Ba element. For yttrium and copper elements, yttrium *iso*-propoxide and copper acetylacetonate or copper ethoxide were used as the precursors of yttrium and copper oxide. However, it was known that yttrium *iso*-propoxide forms lamellar organic-inorganic nanohybride materials in benzyl alcohol.[111] In order to avoid forming this specific structure, acetophenone was then used as solvent instead of benzyl alcohol when yttrium *iso*-propoxide was used as precursor. When the solvent was switched to benzyl alcohol, different metal alkoxides (except yttrium *iso*-propoxide) and acetylacetonates were then used as precursors, which means that there are many combinations available to try various recipes to synthesize YBCO. In addition, benzyl amine was used as solvent when YBC carbonate was taken as the precursor of YBCO.

All the reactions using different solvents are summarized in Table 3.3. The recipes followed the same stoichiometric ratio of yttrium, barium and copper in $YBa_2Cu_3O_7$ (1:2:3). Yttrium iso-propoxide [$Y(i\text{OPr})_3$] and yttrium acetylacetonate [$Y(acac)_3 \cdot xH_2O$] were used as the precursors of the Y element; metallic barium, barium iso-propoxide

[Ba(iOPr)$_2$] and barium acetylacetonate [Ba(acac)$_2$·xH$_2$O] were used as the precursors of the Ba element; copper ethoxide [Cu(OEt)$_2$] and copper acetylacetonate [Cu(acac)$_2$] were used as the precursors of the Cu element.

Table 3.3 Solvothermal reactions for the synthesis of YBCO nanoparticles*

Solvent / Precursor	Acetophenone				Benzyl alcohol				Benzyl amine
	R1	R2	R3	R4	R5	R6	R7	R8	R9
Y(iOPr)$_3$	+	+							
Y(acac)$_3$·xH$_2$O			+	+	+	+	+	+	
Barium	+	+	+	+					
Ba(iOPr)$_2$					+	+			
Ba(acac)$_2$·xH$_2$O							+	+	
Cu(OEt)$_2$	+		+		+		+		
Cu(acac)$_2$		+		+		+		+	
YBC carbonate									+

*All the reactions are presented by "Rx", where x is one of the numbers between 1 to 9. The chemicals involved in each reaction can be found in the column below corresponding "Rx" and are marked with symbol "+".

Because the YBCO nanoparticles couldn't be achieved directly in all the reactions summarized in Table 3.3, we also tried to sinter every product obtained after each reaction at temperature up to 900°C for more than 5 hours to see if we were able to succeed in getting YBCO powders.

3.4.2 Discussion

WAXS measurements proved that none of the experiments presented in Table 3.3 was successful. To learn from these failures. It is necessary to discuss here why we were not able to achieve YBCO nanoparticles, even after high temperature sintering.

I believe that the intrinsic reason of our failure is that the crystal structure of superconducting YBCO is thermodynamically and/or kinetically unfavorable at relatively low temperature, e.g. <500°C. This explains why YBCO powders have only been obtained after long-term high temperature (>600°C) treatment, which indicates that a lot of energy is necessary for the formation of crystal structure of YBCO. Solvothermal sol-gel approach using benzyl alcohol and its derivatives as solvents is a powerful and versatile method to synthesize highly crystalline metal oxides nanoparticles with high purity, uniform particle morphology and narrow particle size distribution, but it is definitely not universal. Some examples, such as the synthesis of PZT materials, indicate that this approach may fail in synthesizing crystalline materials directly without post thermal treatment.[112] One should not expect to change the energetic characteristic of YBCO's crystal structure with this method.

Another important reason is, to realize the right crystal structure of YBCO, yttrium, barium and copper elements should at least incorporate into the substance following the ratio of 1:2:3, regardless if this substance has the right crystal structure of YBCO or not. However, our unsuccessful work indicates that the three precursors involved into the solvothermal reactions have different reaction rates in benzyl alcohol or acetophenone, which makes the formation of homogeneous three-component inorganic network having 1:2:3 ratio of yttrium, barium and copper impossible. If the substances obtained after the solvothermal reactions don't possess the right ratio of Y, Ba and Cu, YBCO can never be achieved, no matter which post sintering process is applied.

Despite the negative experience, we can conclude based on the above discussion, that YBCO superconductors might be synthesized successfully by aforementioned solvothermal sol-gel approach once we find a synthesis recipe including the precursors with matchable reaction rates in certain high-boiling-point alcohols, ketones or amines. Obviously, the number of reactions that were tried is small in comparison to the possible combinations of many different yttrium, barium and

copper alkoxides and high-boiling-point alcohols, ketones and amines, which could be utilized either as precursors or solvents. This means that there is still plenty of "space" left for further exploration of the validity of the solvothermal sol-gel approach in synthesizing YBCO nanoparticles. Furthermore, the subsequent substance obtained via the solvothermal reaction doesn't have to have the right crystal structure of YBCO; it even doesn't have to be crystalline. As long as it contains the right 1:2:3 ratio of yttrium, barium and copper, it can be later transformed into the crystal structure of YBCO by high temperature sintering. If the obtained substance has an average particle size in the range of tens of nanometers or even less, there is still a high probability to reduce the sintering temperature significantly, which is one of the main goals for the synthesis of YBCO nanoparticles.

3.4.3 Conclusion

Various precursors of yttrium, barium and copper including metallic barium, metal alkoxides, metal acetylacetonates and YBC carbonate were used to synthesize YBCO nanoparticles following the solvothermal sol-gel approach. None of the reactions (summarized in Table 3.3) was successful. However, there are still good chances to synthesize YBCO nanoparticles via this method. The major task in the future is to find the precursor combination, which has the same or similar reaction rates for all precursors, so that the preparation of a homogeneous three-component inorganic network of YBCO or its precursor is possible.

References

[1] C. Burda, X. Chen, R. Narayanan, M. A. El-Sayed, *Chem. Rev.* **2005**, *105*, 1025.

[2] A. P. Alivisatos, *J. Phys. Chem.* **1996**, *100*, 13226.

[3] A. Henglein, *Chem. Rev.* **1989**, *89*, 1861.

[4] M. L. Steigerwald, L. E. Brus, *Acc. Chem. Res.* **1990**, *23*, 183.

[5] M. A. El-Sayed, *Acc. of Chem. Res.* **2004**, *37*, 326.

[6] R. Rossetti, S. Nakahara, L. E. Brus, *J. Chem. Phys.* **1983**, *79*, 1086.

[7] R. Rossetti, J. L. Ellison, J. M. Gibson, L. E. Brus, *J. Chem. Phys.* **1984**, *80*, 4464.

[8] B. L. Cushing, V. L. Kolesnichenko, C. J. O'Connor, *Chem. Rev.* **2004**, *104*, 3893.

[9] M. Jansen, *Angew. Chem. Int. Ed.* **2002**, *41*, 3747.

[10] J. Gopalakrishnan, *Chem. Mater.* **1995**, *7*, 1265.

[11] L. G. Hubert-Pfalzgraf, *J. Mater. Chem.* **2004**, *14*, 3113.

[12] J. Livage, M. Henry, C. Sanchez, *Prog. Solid St. Chem.* **1988**, *18*, 259.

[13] E. Matijevic, *Chem. Mater.* **1993**, *5*, 412.

[14] A. W. Dearing, E. E. Reid, *J. Am. Chem. Soc.* **1928**, *50*, 3058.

[15] A. Vioux, *Chem. Mater.* **1997**, *9*, 2292.

[16] J. N. Hay, H. M. Raval, *Chem. Mater.* **2001**, *13*, 3396.

[17] T. Hyeon, *Chem. Commun.* **2003**, 927.

[18] M. Niederberger, G. Garnweitner, N. Pinna, G. Neri, *Prog. Solid State Chem.* **2005**, in print.

[19] Y. W. Jun, J. H. Lee, J. S. Choi, J. Cheon, *J. Phys. Chem. B* **2005**, *109*, 14795.

[20] M. Niederberger, M. H. Bartl, G. D. Stucky, *Chem. Mater.* **2002**, *14*, 4364.

[21] N. Pinna, M. Antonietti, M. Niederberger, *Colloids Surf., A* **2004**, *250*, 211.

[22] N. Pinna, G. Neri, M. Antonietti, M. Niederberger, *Angew. Chem. Int. Ed.* **2004**, *43*, 4345

[23] M. Niederberger, G. Garnweitner, J. Buha, J. Polleux, J. Ba, N. Pinna, *J. Sol-Gel Sci. Tech.* **2005**, submitted.

[24] N. Pinna, G. Garnweitner, M. Antonietti, M. Niederberger, *Adv. Mater.* **2004**, *16*, 2196.

[25] M. Niederberger, N. Pinna, J. Polleux, M. Antonietti, *Angew. Chem. Int. Ed.* **2004**, *43*, 2270.

[26] M. Niederberger, G. Garnweitner, F. Krumeich, R. Nesper, H. Cölfen, M. Antonietti, C*hem. Mater.* **2004,** *16,* 1202.

[27] J. Ba, J. Polleux, M. Antonietti, M. Niederberger, *Adv. Mater.* **2005,** *17,* 2509.

[28] M. Niederberger, G. Garnweitner, N. Pinna, M. Antonietti, *J. Am. Chem. Soc.* **2004,** *126,* 9120.

[29] D. F. R. Jianhua Ba, Armin Feldhoff, Torsten Brezesinski, Igor Djerdj, Michael Wark, Markus Niederberger, C*hem. Mater.* **2006,** submitted.

[30] G. Eranna, B. C. Joshi, D. P. Runthala, R. P. Gupta, *Crit. Rev. Solid State Mater. Sci.* **2004,** *29,* 111.

[31] N. Barsan, M. Schweizer-Berberich, W. Göpel, *Fresenius J. Anal. Chem.* **1999,** *365,* 287.

[32] Y. Zhang, A. Kolmakov, Y. Lilach, M. Moskovits, *J. Phys. Chem. B* **2005,** *109,* 1923.

[33] C. P. Nicholas, T. J. Marks, *Nano Lett.* **2004,** *4,* 1557.

[34] Y. Idota, T. Kubota, A. Matsufuji, Y. Maekawa, T. Miyasaka, *Science* **1997,** *276,* 1395.

[35] A. C. Arias, J. R. de Lima, I. A. Hümmelgen, *Adv. Mater.* **1998,** ***10,*** 392.

[36] A. Andersson, N. Johannsson, P. Bröms, N. Yu, D. Lupo, W. R. Salaneck, *Adv. Mater.* **1998,** *10,* 859.

[37] S. de Monredon, A. Cellot, F. Ribot, C. Sanchez, L. Armelao, L. Gueneau, L. Delattre, *J. Mater. Chem.* **2002,** *12,* 2396.

[38] Y. L. Wang, X. C. Jiang, Y. N. Xia, *J. Am. Chem. Soc.* **2003,** *125,* 16176.

[39] B. Cheng, J. M. Russell, W. Shi, L. Zhang, E. T. Samulski, *J. Am. Chem. Soc.* **2004,** ***126***, 5972.

[40] Z. R. Dai, Z. W. Pan, Z. L. Wang, Adv. *Funct. Mater.* **2003,** *13*, 9.

[41] J. Hu, Y. Bando, Q. Liu, D. Golberg, *Adv. Funct. Mater.* **2003,** *13*, 493.

[42] Z. Liu, D. Zhang, S. Han, C. Li, T. Tang, W. Jin, X. Liu, B. Lei, C. Zhou, *Adv. Mater.* **2003,** *15*, 1754.

[43] P. D. Yang, D. Y. Zhao, D. I. Margolese, B. F. Chmelka, G. D. Stucky, *Nature* **1998,** *396*, 152.

[44] B. Smarsly, D. Grosso, T. Brezesinski, N. Pinna, C. Boissiere, M. Antonietti, C. Sanchez, *Chem. Mater.* **2004,** *16*, 2948.

[45] T. Brezesinski, M. Antonietti, M. Groenewolt, N. Pinna, B. Smarsly, *New J. Chem.* **2005,** *29,* 237.

[46] D. Grosso, C. Boissiere, B. Smarsly, T. Brezesinski, N. Pinna, P. A. Albouy, H. Amenitsch, M. Antonietti, C. Sanchez, *Nat. Mater.* **2004,** *3*, 787.

[47] K. G. Severin, T. M. Abdel-Fattah, T. J. Pinnavaia, *Chem. Commun.* **1998,** 1471.

[48] L. Qi, J. Ma, H. Cheng, Z. Zhao, *Langmuir* **1998,** *14***,** 2579.

[49] F. Chen, M. Liu, Chem. *Commun.* **1999,** 1829.

[50] Y. D. Wang, C. L. Ma, X. D. Sun, H. D. Li, *Mater. Lett.* **2001,** *51*, 285.

[51] B. Yuliarto, H. Zhou, T. Yamada, I. Honma, K. Asai, *Chem. Lett.* **2003,** *32***,** 510.

[52] R. W. J. Scott, N. Coombs, G. A. Ozin, *J. Mater. Chem.* **2003,** *13***,** 969.

[53] H. Miyata, M. Itoh, M. Watanabe, T. Noma, *Chem. Mater.* **2003,** *15*, 1334.

[54] T. Toupance, O. Babot, B. Jousseaume, G. Vilaca, *Chem. Mater.* **2003,** *15***,** 4691.

[55] C. Y. Tung, N. L. Wu, I. A. Rusakova, *J. Mater. Res.* **2003,** *18*, 2890.

[56] M. S. Wong, E. S. Jeng, J. Y. Ying, *Nano Lett.* **2001,** *1***,** 637.

[57] F. Bosc, A. Ayral, P. A. Albouy, L. Datas, C. Guizard, *Chem. Mater.* **2004,** *16,* 2208.

[58] A. Corma, P. Atienzar, H. Garcia, J. Y. Chane-Ching, *Nat. Mater.* **2004,** *3***,** 394.

[59] A. S. Deshpande, N. Pinna, B. Smarsly, M. Antonietti, M. Niederberger, *Small* **2005,** *1***,** 313.

[60] H. P. a. A. Klug, X-ray *Diffraction Procedures for Polycrystalline and Amorphous Materials,* Wiley Interscience, New York, **1974**.

[61] H. Cölfen, T. Pauck, *Colloid Polym. Sci.* **1997,** *275,* 175.

[62] D. S. Ginley, C. Bright, *MRS Bulletin* **2000,** *25,* 15.

[63] T. Minami, *Semicond. Sci. and Technol.* **2005,** *20,* S35.

[64] B. G. Lewis, D. C. Paine, *MRS Bulletin* **2000,** *25,* 22.

[65] W. A. Gazotti, G. Casalbore-Miceli, A. Geri, A. Berlin, M. A. De Paoli, *Adv. Mater.* **1998,** *10,* 1522.

[66] F. Pichot, S. Ferrere, R. J. Pitts, B. A. Gregg, *J. Electrochem. Soc.* **1999,** *146,* 4324.

[67] C. G. Granqvist, A. Hultaker, *Thin Solid Films* **2002,** *411,* 1.

[68] C. Y. Xu, L. Liu, S. E. Legenski, D. Ning, M. Taya, *J. Mater. Res.* **2004,** *19,* 2072.

[69] H. Kobayashi, T. Ishida, Y. Nakato, H. Tsubomura, *J. Appl. Phys.* **1991,** *69,* 1736.

[70] M. A. Martinez, J. Herrero, M. T. Gutierrez, *Thin Solid Films* **1995,** *269,* 80.

[71] V. S. Vaishnav, P. D. Patel, N. G. Patel, *Thin Solid Films* **2005,** *487,* 277.

[72] A. Forleo, L. Francioso, M. Epifani, S. Capone, A. M. Taurino, P. Siciliano, *Thin Solid Films* **2005,** *490,* 68.

[73] J. P. Zheng, H. S. Kwok, *Appl. Phys. Lett.* **1993,** *63,* 1.

[74] T. Maruyama, K. Fukui, *J. Appl. Phys.* **1991,** *70,* 3848.

[75] G. Frank, H. Kärstlin, *Appl. Phys. A: Mater Sci. Process.* **1982,** *27,* 197.

[76] M. A. Aegerter, J. Puetz, G. Gasparro, N. Al-Dahoudi, *Opt. Mater.* **2004,** *26*, 155.

[77] S. Kundu, P. K. Biswas, *Chem. Phys. Lett.* **2005,** *414,* 107.

[78] M. Epifani, R. Diaz, J. Arbiol, P. Siciliano, J. R. Morante, *Chem. Mater.* **2006,** *18*, 840.

[79] M. J. Alam, D. C. Cameron, *Thin Solid Films* **2002,** *420-421*, 76.

[80] C. Goebbert, R. Nonninger, M. A. Aegerter, H. Schmidt, *Thin Solid Films* **1999,** *351,* **7**9.

[81] J. Ederth, P. Johnsson, G. A. Niklasson, A. Hoel, A. Hultaker, P. Heszler, C. G. Granqvist, A. R. v. Doorn, M. J. Jongerius, D. Burgard, *Phys. Rev. B* **2003,** *68,* 155410.

[82] N. Al-Dahoudi, M. A. Aegerter, *J. Sol-Gel Sci. Technol.* **2003,** *26,* 693.

[83] H.-R. Xu, G.-S. Zhu, H.-Y. Zhou, A.-B. Yu, *Mater. Lett.* **2005,** *59,* 19.

[84] S.-M. Kim, K.-H. Seo, J.-H. Lee, J.-J. Kim, H. Y. Lee, J.-S. Lee, *J. Eur. Ceram. Soc.* **2006,** *26,* 73.

[85] P. D. Cozzoli, A. Kornowski, H. Weller, *J. Am. Chem. Soc.* **2003,** *125*, 14539.

[86] J. Park, K. An, Y. Hwang, J. G. Park, H. J. Noh, J. Y. Kim, J. H. Park, N. M. Hwang, T. Hyeon, *Nat. Mater.* **2004,** *3,* 891**.**

[87] M. Epifani, J. Arbiol, R. Diaz, M. J. Peralvarez, P. Siciliano, J. R. Morante, *Chem. Mater.* **2005,** *17,* 6468.

[88] B. C. Gaskins, J. J. Lannutti, *J. Mater. Res.* **1996,** *11,* 1953.

[89] H. Kominami, J. Kato, Y. Takada, Y. Doushi, B. Ohtani, S. Nishimoto, M. Inoue, T. Inui, Y. Kera, *Catal. Lett.* **1997,** *46,* 235.

[90] M. Niederberger, M. H. Bartl, G. D. Stucky, *J. Am. Chem. Soc.* **2002,** *124,* 13642.

[91] G. Garnweitner, M. Antonietti, M. Niederberger, *Chem. Commun.* **2004,** 397.

[92] N. Pinna, G. Garnweitner, M. Antonietti, M. Niederberger, *J. Am. Chem. Soc.* **2005,** *127,* 5608.

[93] J. Polleux, A. Gurlo, M. Antonietti, M. Niederberger, *Angew. Chem. Int. Ed.* **2006,** *45,* 261.

[94] G. B. Gonzalez, T. O. Mason, J. P. Quintana, O. Warschkow, D. E. Ellis, J. H. Hwang, J. P. Hodges, J. D. Jorgensen, *J. Appl. Phys.* **2004,** *96, 3*912.

[95] A. J. Freeman, K. R. Poeppelmeier, T. O. Mason, R. P. H. Chang, T. J. Marks, *MRS Bulletin* **2000,** *25,* 45.

[96] M. Quaas, C. Eggs, H. Wulff, *Thin Solid Films* **1998,** *332,* 277.

[97] J. Polleux, N. Pinna, M. Antonietti, C. Hess, U. Wild, R. Schlögl, M. Niederberger, *Chem. Eur. J.* **2005,** *11,* 3541.

[98] J. F. Moulder, W. F. Stickle, P. E. Sobol, K. D. Bomben, Handbook of *X-ray Photoelectron Spectroscopy: A Reference Book of Standard Spectra for Identification and Interpretation of XPS Data, Physical Electronics Division.* **1992.**

[99] B. Pujilaksono, U. Klement, L. Nyborg, U. Jelvestam, S. Hill, D. Burgard, *Mater. Charact.* **2005,** *54,* 1.

[100] G. Frank, H. Kötlin, A. Rabenau, *Phys. Status Solidi A* **1979,** *52,* 231.

[101] N. Nadaud, N. Lequeux, M. Nanot, J. Jove, T. Roisnel, *J. Solid State Chem.* **1998,** *135,* 140.

[102] P. Parent, H. Dexpert, G. Tourillon, J. M. Grimal, *J. Electrochem. Soc.* **1992,** *139,* 282.

[103] J. H. Hwang, P. P. Edwards, H. K. Kammler, T. O. Mason, *Solid State Ionics* **2000,** *129,* 135.

[104] G. B. Gonzalez, J. B. Cohen, J. H. Hwang, T. O. Mason, J. P. Hodges, J. D. Jorgensen, *J. Appl. Phys.* **2001,** *89,* 2550.

[105] M. J. Alam, D. C. Cameron, *Thin Solid Films* **2000,** *377,* 455.

[106] S. Seki, Y. Sawada, T. Nishide, *Thin Solid Films* **2001,** *388,* 22.

[107] S. R. Ramanan, *Thin Solid Films* **2001,** *389,* 207.

[108] J.-S. Lee, S.-C. Choi, *J. Eur. Ceram. Soc.* **2005,** *25,* 3307.

[109] A. W. Sleight, *Science* **1988,** *242,* **1519.**

[110] R. F. Service, *Science* **2002,** *295,* 787.

[111] N. Pinna, G. Garnweitner, P. Beato, M. Niederberger, M. Antonietti, *Small* **2005,** *1,* 112.

[112] G. Garnweitner, J. Hentschel, M. Antonietti, M. Niederberger, *Chem. Mater.* **2005,** *17,* 4594.

Chapter 4 Self-Assembly of Preformed Crystalline Metal Oxides Nanoparticles towards Mesoporous Structure

4.1 Introduction

Since the first successful discovery of mesoporous (2 nm-50 nm[1]) silicate materials, the family of molecular sieves MCM-41 and M41S,[2, 3] numerous efforts have been dedicated to fabricate silicate- or non-silicate-based materials with mesoporous structures and many fascinating mesoporous materials have been achieved.[2-9] The idea behind it was to combine the evaporation induced self-assembly (EISA)[10] with block copolymer templating techniques to produce mesoporous metal oxides, using either molecular precursors or preformed crystalline nanoparticles (nanobuilding blocks, NBBs).[2]

Typically, the molecular precursors, such as tetraethylorthosilicate (TEOS) and transition metal chlorides such as $TiCl_4$, $ZrCl_4$, WCl_6,[5] which are able to form 3-D molecular networks by hydrolysis and condensation reactions, are always employed as the starting materials for the formation of mesopores. Under the direction of proper templates, mesopores are built up and fixed by a crystalline inorganic framework via the removal of templates during thermal treatment. Although the molecular precursors functioned well and many silicate- and non-silicate-based materials with fine mesoporous structures have been achieved,[2-9, 11-14] the disadvantages of molecular precursors are still not neglectable. The unsatisfying thermal stability, serious shrinkage during calcination and sensitive synthesis conditions are the reasons, why scientists continue to search for alternative routes to mesoporous materials. The utilization of preformed nanoparticles is a particularly advantageous approach, because there is a large toolbox of readily available nanoparticles covering a wide range of compositions, sizes and shapes.[15] Furthermore, the use of nanoparticles generally simplifies the preparation of mesoporous metal oxides, since control over hydrolysis and condensation of the molecular precursors as well as over the

crystallization process during calcination can be avoided. Accordingly, the synthesis route to mesoporous metal oxides starting from preformed crystalline NBBs is generally highly reproducible. The use of nanocrystals keeps the shrinkage of the metal oxide framework negligible during the removal of the organic template by calcination, an important factor for the persistence of the mesopores. The pore accessibility of the interior of the mesoporous materials is enhanced, because of the particle-particle interstice. Finally, the nanoparticle approach offers the possibility to mix several different metal oxide nanoparticles in order to obtain mesoporous materials with highly complex compositions. J. Y. Ying et al. made the first attempt to produce crystalline mesoporous metal oxides with preformed nanoparticulate precursors.[7] In their approach nanocrystalline tungstated zirconia was utilized to construct the wall of the mesopores. A block copolymer, Pluronic P-123, was added as the templating surfactant and led to the formation of mesopores as the effect of hydrophilic-hydrophobic interaction. After removal of the organic compounds, relatively monodisperse pore sizes (4-7 nm) and high thermal stability were realized. Following their work, several groups have achieved different mesoporous materials with highly ordered mesostructure and various pore sizes by using different crystalline nanoparticles.[16-18]

Among the numerous metal oxides, we focused our research interests mainly on the use of TiO_2 and SnO_2 as NBBs for the formation of mesoporous materials. Titanium oxide is a nontoxic material with various applications such as catalysis, optics, photovoltaics etc. Tin oxide attracts significant interests for gas sensing,[19, 20] catalysis,[21, 22] electrochemistry[23] and optoelectronic devices[24, 25] etc. The sols of these two metal oxides have been realized successfully in our group[26-28] and the sizes of the nanoparticles are nearly monodisperse. The nanoparticles can easily be stabilized in certain solvent such as water or THF, which is one of the prerequisites to perform EISA process for the formation of mesoporous materials.

Furthermore, in order to detect the possibility of making mesoporous mixtures of two

different metal oxides, we also produced mesoporous mixtures of TiO_2 and CeO_2, SnO_2 and $BaTiO_3$, respectively. Cerium oxide exhibits excellent properties as catalysts[28, 29] high temperature ceramics[16] and for the use in fuel cells. Barium titanate is probably the best-known ferroelectric material,[30] because of its high dielectric constant[31, 32] and ferroelectric properties[33, 34] that are essential for its use in electroceramic.[35-38] The combination of TiO_2 and CeO_2, SnO_2 and $BaTiO_3$ shows the potential to produce bi-functional mesoporous metal oxides, which have the outstanding properties of both compositions on the nanoscale, and therefore, extend potential applications of these metal oxides into new areas.

The idea behind this project was to employ the metal oxide nanoparticles as building blocks, which construct the mesoporous framework under the direction of micelles formed by PB-PEO [polybutylene-block-poly(ethylene oxide)] block copolymer due to the hydrophilic-hydrophobic interactions. By evaporating the solvents completely, the mesostructures are "frozen", and then maintained by the NBBs after the removal of all organics by calcination. The schematic diagram of this process is given in Scheme 4.1. Firstly, a homogenous sol is formed by mixing two components, preformed crystalline nanoparticles and block copolymer template, in a proper solvent. And then, depending on different applications, films or bulk material can be obtained by dip coating or drying in Petri dish, respectively. After drying at room temperature and then in the oven at 100° C, the resultant material is calcined at 470° C or 500° C, by which the template is removed and the desired mesoporous material is achieved.

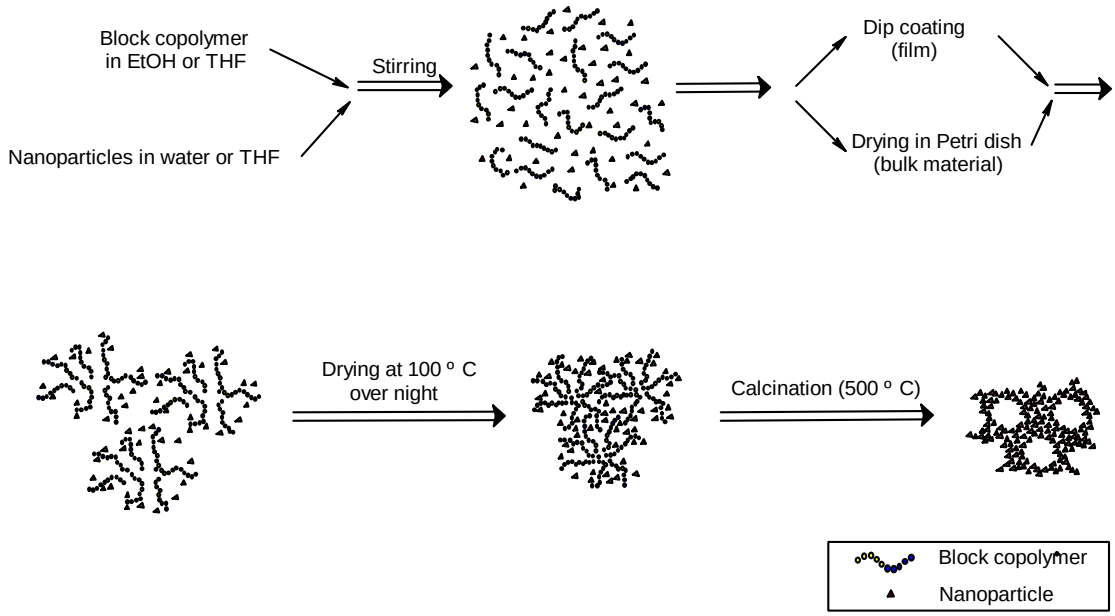

Scheme 4.1 Synthesis process of mesoporous metal oxide by using crystalline nanoparticles as NBBs and block copolymers as templates.

It's worth noticing that in order to form a homogeneous sol of nanocrystal precursor and polymer template, one has to find a proper way to disperse both components, especially the crystalline nanoparticles. This task is truly the tricky point for the formation of desired mesoporous structure. Crystalline nanoparticles normally prefer to form large agglomerates and then precipitate out of the solvent. Therefore, one has to minimize the agglomeration behavior by functionalization of the particle surface so that the nanoparticle precursor can be stabilized in the solvent.

Another crucial point is the selection of polymer template for the formation of the mesopores. A useful polymer template should not only be able to form stable micelles, but also has to provide good thermal stability and relatively long chain length.[39] It should be thermally stable because violent physical and chemical changes occur during calcination procedure. Without good thermal stability, the polymer template won't be able to support the porous structure before the inorganic network is able to maintain the mesopores during calcination. On the other hand, once the stable porous structure is achieved, the block copolymer has fulfilled its role and should be gone

completely. Practically, the procedures of the removal of polymer template and the formation of stable pore structure always overlap. In other words, the decomposition of the template starts before the "stable" pore structure forms. But as long as the template is still able to support the mesoporous structure till the nanoparticles take over the role to maintain the mesopores, one could finally achieve mesoporous material. The consideration of the necessary chain length is due to the large nanocrystal size. One of the main functions of the polymer template is to direct the particles to construct the porous structure. In order to manipulate the nanoparticles and fit them into the wall of the mesopores, long polymer chain length, which means strong interaction with nanoparticles and ability to form large micelles, is definitely necessary.

4.2 Synthesis of Mesoporous TiO_2

4.2.1 Experimental

I concentrated my attention on producing bulk material of mesoporous TiO_2 in this project, although part of my work related to mesoporous materials was dealing with the films. So far, most of the success in making mesoporous metal oxides by using molecular precursors was achieved by fabricating films on certain substrates (silicon or glass wafers).[5, 13, 40-42] In contrast to the use of molecular precursors, preformed crystalline nanoparticles offer better opportunity to produce bulk mesoporous metal oxides, which could be at least as thick as 1 mm.

Concerning the polymer template, there are several well-known commercially available block copolymer templates, such as Pluronic P-123 or F-127 etc. But none of them worked on the nanocrystals used in my project. This is reasonable because none of them is able to fulfill the demands that have been mentioned previously. The major problem is that their chain lengths are too short to manipulate the crystalline nanoparticles (a few nanometers large) to build up mesopores. For example, the chain length of hydrophilic block of Pluronic P-123 is only 7.5 nm. There are also some

block copolymer candidates available in our institute with larger block lengths, such as KLE [poly(ethylene-*co*-butylene)-*block*-poly(ethylene oxide)][43] and PB-BEO [39] synthesized by Schlaad's group. A. Thomas and T. Brezesinski's work[43-46] has proven that KLE is an excellent polymer template for the synthesis of mesoporous metal oxides using molecular precursors. Both KLE and PB-PEO were used to make mesoporous TiO_2 with crystalline nanoparticles. The obtained results confirmed that they all functioned well in templating mesoporous structure.

4.2.1.1 Synthesis of Mesoporous TiO_2 Films

The major purpose of this project was to synthesize mesoporous bulk TiO_2. However, in order to investigate the influence of different parameters, such as the volume ratio of inorganic particles and polymer template ($V_{n/p}$), the humidity during the evaporation of the solvent and the different techniques used to make films etc., mesoporous TiO_2 films were fabricated prior to the bulk material. They were more realizable with fewer raw materials, i.e. nanoparticles and polymer template, and less time consuming than bulk material. Among all these parameters, $V_{n/p}$ was supposed to play an important role in the formation of mesoporous structure according to previous work done by using molecular precursors.

A typical synthesis procedure of mesoporous TiO_2 film was performed as the following. A homogeneous TiO_2 aqueous sol (3 wt%,) was obtained by the addition of 0.3 g dopamine modified TiO_2 nanoparticles[26] into 9.7 g water. Meanwhile, 0.2 g PB-PEO-23 was dissolved in 5 ml ethanol. These two solutions were then mixed together so that a dark red transparent colloidal dispersion ($V_{n/p}$=0.4) formed and was ready for further treatments. In the case of making mesoporous TiO_2 films, a piece of single-crystal silicon wafer in the size of 3 cm × 2 cm was placed on a dip coater (picture shown in Figure 4.1) and dipped into the aforementioned TiO_2 sol and then withdrawn at the speed of 6 mm/s under constant relative humidity (~40%). The obtained film was left at room temperature for several hours and kept in the oven at 100°C overnight. The dry film was then calcined following certain program (shown in

Scheme 4.2) under air, after which the mesoporous TiO_2 film was achieved and termed F-Ti-PP-4.

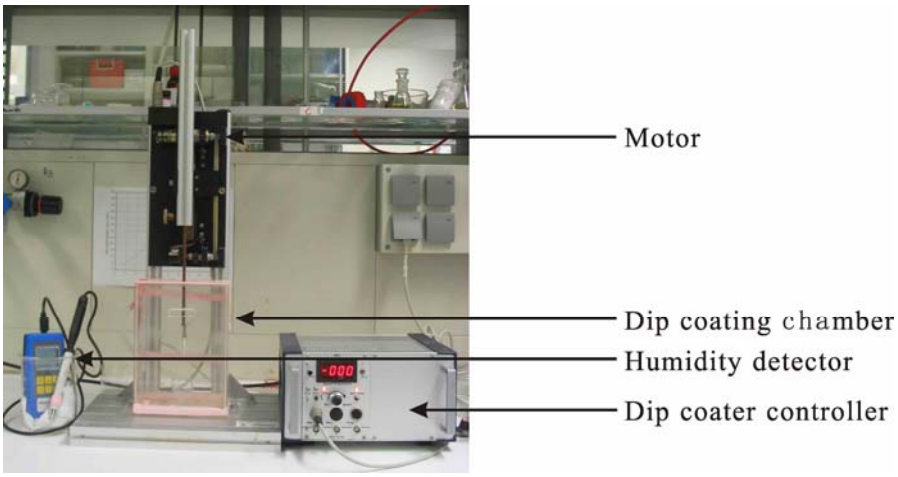

Figure 4.1 Dip-coater used for the synthesis of mesoporous TiO_2 films.

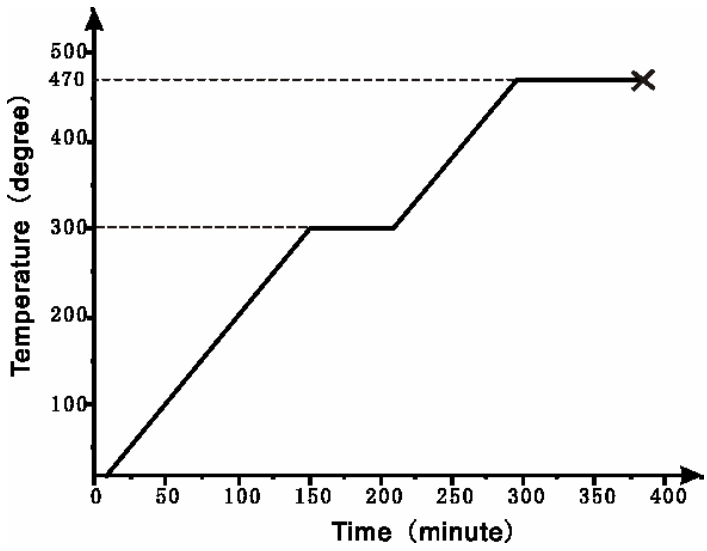

Scheme 4.2 Calcination program for the formation of mesoporous TiO_2 films.

The entire temperature enhancement is operated at the speed of 2°C/min. The little cross in the diagram in Figure 4.2 is the point that the program ends. After that, the oven is cooled down to room temperature automatically without any additional cooling system.

All the films made in this section were presented in Table 4.1 including their relevant

parameters.

Table 4.1

Sample name	$V_{n/p}$	Polymer template	Dip/Spin coating	Relative humidity
F-Ti-PP-1	0.1	PB-PEO-23	D	~40%
F-Ti-PP-2	0.2	PB-PEO-23	D	~40%
F-Ti-PP-3	0.3	PB-PEO-23	D	~40%
F-Ti-PP-4	0.4	PB-PEO-23	D	~40%
F-Ti-PP-5	0.4	PB-PEO-23	D	~10%
F-Ti-PP-6	0.4	PB-PEO-23	D	~20%
F-Ti-PP-7	0.4	PB-PEO-23	D	~30%
F-Ti-PP-8	0.4	PB-PEO-23	S	~40%
F-Ti-KLE-1	0.4	KLE-22	D	~40%
F-Ti-KLE-2	0.5	KLE-22	D	~40%

4.2.1.2 Synthesis of Mesoporous TiO_2 Bulk Material

The preparation of mesoporous TiO_2 bulk material was similar to the synthesis procedure of TiO_2 films. After the mixing of TiO_2 aqueous solution and the solution of polymer template PB-PEO-23 in ethanol, the obtained homogeneous colloidal dispersion ($V_{n/p}$=0.4) was directly poured into a Petri dish (5 cm in diameter) and dried at room temperature for 3-5 days so that most of the solvent, both water and ethanol, were gone via evaporation. Afterwards, the remaining substance was scratched from the Petri dish and kept in the oven at 100°C for 2 days. Finally, the dry pieces of the mixture of TiO_2 and PB-PEO-23 were calcined using the similar program as demonstrated in Scheme 4.2 (the time remaining at 470°C was prolonged to 2 hours) to remove all the organics. After the calcination, a white, fragile material was obtained and termed as B-Ti-PP.

All the samples discussed in this chapter, including films and bulk material, only refer to the samples after calcination.

4.2.1.3 Characterizations

All the mesoporous TiO_2 films were mainly investigated by TEM to qualify their porous structures and find out the optimum synthesis conditions. Additionally, sample F-Ti-PP-4 was also studied by SEM, WAXS and by krypton adsorption to probe its surface morphology, crystal structure and specific surface area, respectively.

Sample B-Ti-PP was fully characterized by most of the typical characterization techniques of porous materials, such as SAXS, WAXS, BET, TEM, SEM, HRTEM and TGA.

4.2.2 Results and Discussion

4.2.2.1 TEM studies of mesoporous TiO_2 films

Representative TEM images of sample F-Ti-PP-1, 2, 3 and 4 are shown in Figure 4.2 and 4.3, respectively. The positive information from these images is that mesoporous TiO_2 films had been achieved successfully and their pore sizes were all the same, about 20-25 nm in diameter with 15 nm of wall thickness. It seems that $V_{n/p}$=0.4 offered the best porous structure and seemed to be the optimum parameter for the synthesis of mesoporous TiO_2. $V_{n/p}$=0.1 gave the worst pore structure. One can also find that the porous structures of F-Ti-PP-3 ($V_{n/p}$=0.3) and F-Ti-KLE-2 ($V_{n/p}$=0.5, TEM image shown in Figure 4.5c) are quite similar to F-Ti-PP-4. Without other techniques, one can hardly prove that $V_{n/p}$=0.4 is surely the best parameter to use. Nevertheless, it would be safe to say that $V_{n/p}$ in between 0.3 and 0.5 gives good mesoporous structure. This is sufficient for further working on producing mesoporous bulk TiO_2 materials.

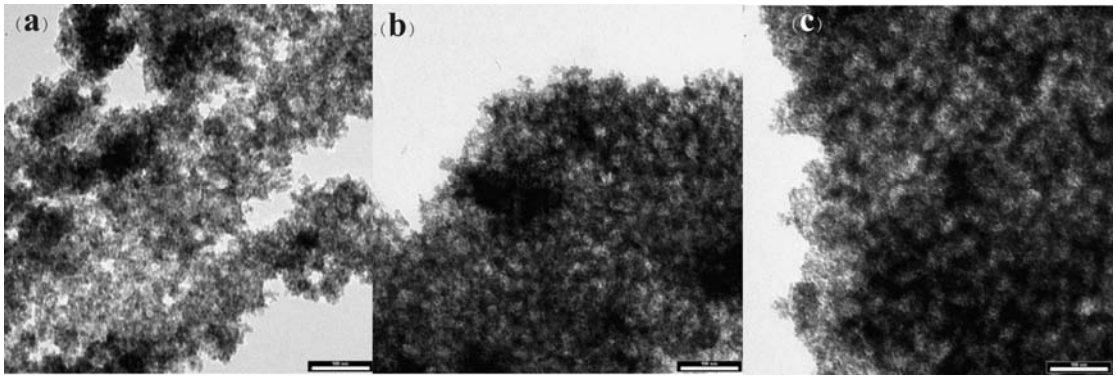

Figure 4.2 (a), (b) and (c) TEM images of sample F-Ti-PP-1, 2, 3, respectively. The scale bars in all three images are 100 nm.

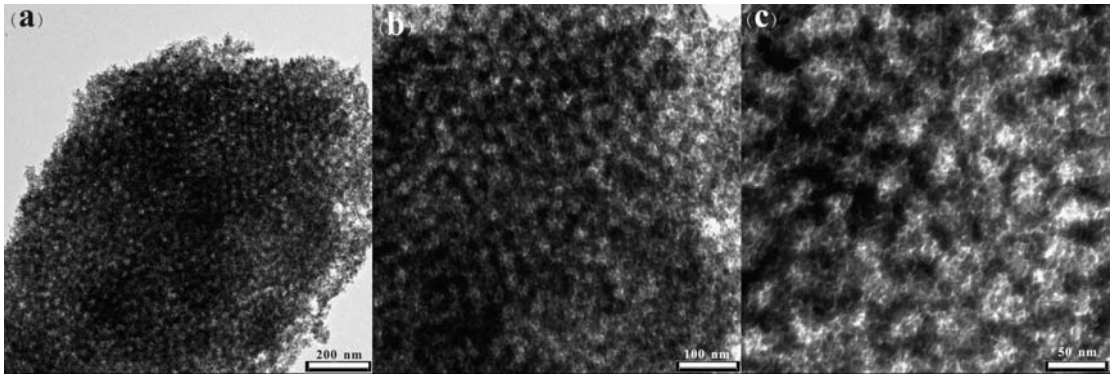

Figure 4.3 TEM images of sample F-Ti-PP-4 with different magnifications.

The only difference between samples F-Ti-PP-1, 2, 3, 4 was that they had different $V_{n/p}$, which was varied from 0.1 to 0.4. It's expected that the porosity of those samples would vary dramatically due to the huge changes in the amount of template, which increased 4 times from $V_{n/p}$=0.4 to $V_{n/p}$=0.1. However, the information one could extract from the TEM images in Figure 4.2 and 4.5 (c) is that one is only able to achieve mesoporous structure TiO_2 with highly randomly ordered pores. My further work on this project had proven that, no matter how one adjusts the synthesis conditions carefully, no conversion from disordered to highly ordered porous structure would happen as long as we use dopamine functionalized TiO_2 nanoparticles as NBB. This is due to the intrinsic characteristics of the row materials we use and will be further discussed in the end of this chapter. On the other hand, this phenomenon also proves that, basically, no rigorous synthesis conditions are necessary for the formation of mesoporous metal oxides when preformed nanocrystals are used as NBBs.

In the case of using molecular precursors to make mesoporous metal oxide films, humidity is one of the important factors to form highly ordered porous structures and has to be well controlled.[42] In order to observe the influence of surrounding humidity during solvent evaporation on the porosity of the TiO_2 films, the relative humidity of the dip-coating chamber was varied from 10% to 40%. The TEM images of sample F-Ti-PP-5, 6, 7 are presented in Figure 4.4. By comparing the TEM images in Figure 4.3 and 4.4, one can easily see that higher humidity induces better porous structures. It could be explained as the following. There are two kinds of solvent existing in the precursor solution, water and ethanol. The boiling point of ethanol is 78.3°C at 1 atm, much lower than water (100°C), which means ethanol evaporates faster than water. Therefore, water is the dominant substance of the EISA process as well as the formation of mesoporous structure. When the ambient humidity decreases, the evaporation rate of ethanol doesn't change much, whereas the evaporation of water becomes faster due to the larger vapor pressure difference. During EISA process, the evaporation of solvent allows at first the formation of micelles and then the packing of the micelles into certain ordered or not well ordered structure depending on the characteristics of the templates. If the solvent leaves too fast, the micelles won't have enough time to manipulate the NBBs and form well ordered structure before all the solvent is gone and the structure is fixed. This is why the porous structure of sample F-Ti-PP-5 (Figure 4.4a) is worse than other samples. However, if the humidity is high enough, the evaporation rate of water won't impact the final porous structure very much and other factors become more influential on the formation of resulting structure. And this could be proven by the fact that the porous structure looks quite similar when the humidity is varied from 30% (Figure 4.4c), 40% (Figure 4.3a) to 50% (image not shown). For the practical operation, 40% is used as the standard humidity for the synthesis of further samples.

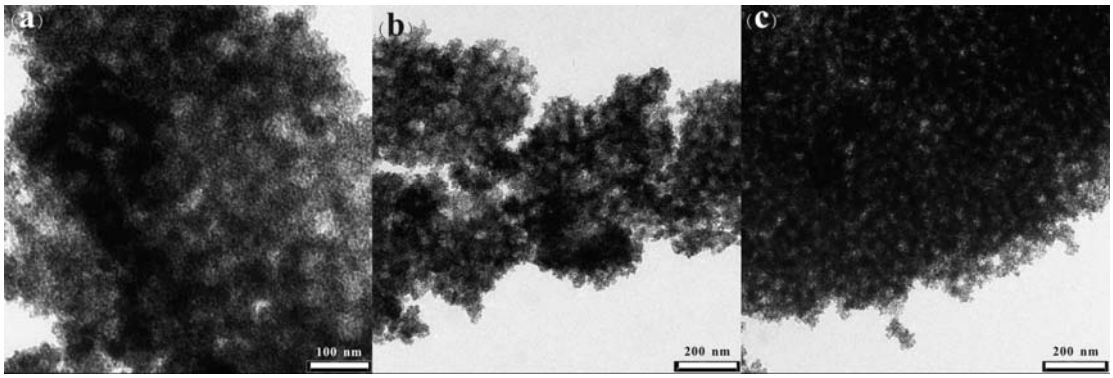

Figure 4.4 (a), (b), (c) TEM images of sample F-Ti-PP-5, 6, 7, respectively.

As mentioned before, in addition to PB-PEO-23, KLE-22 was also used as the template in this project. The TEM images of obtained films using KLE-22 as template are presented in Figure 4.5. They demonstrate that KLE-22 is also able to function as template to form mesoporous TiO_2 with dopamine functionalied TiO_2 as NBBs. Because its chain length is shorter than PB-PEO-23, the pore size templated by KLE-22, which has approximate 15 nm in diameter and 10 nm of wall thickness, is smaller than the pores formed under the templating of PB-PEO-23. Regardless of pore size, the other structural features of mesoporous TiO_2 using KLE-22 as template are quite similar to the samples using PB-PEO-23: highly porous but no regular pore ordering. Besides, by comparing Figure 4.5a and c, one can barely tell if different $V_{n/p}$ values, in other words, different polymer amount, give significantly various porous structures, which fits the conclusion made in the case using PB-PEO-23. The porous structure of sample F-Ti-KLE-1 in Figure 4.5a might look better than sample F-Ti-KLE-1 in Figure 4.5c. However, this could be due to TEM specimen preparation.

Furthermore, the successful attempt to make mesoporous TiO_2 by using KLE-22 as template exhibits good possibility to tune the pore size of mesoporous TiO_2. By carefully selecting proper block copolymer with different chain lengths, one is able to control the pore size as well as the pore structure of TiO_2 in certain scale range using preformed crystalline NBBs.

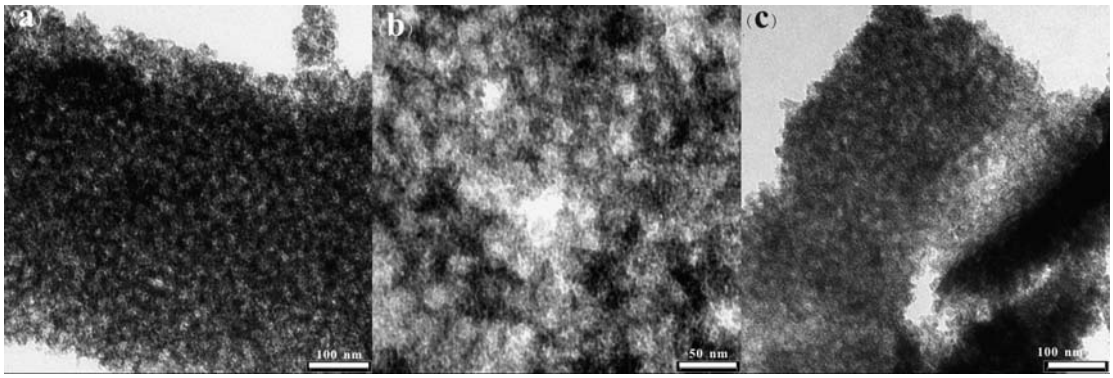

Figure 4.5 (a), (b) TEM images of sample F-Ti-KLE-1 with different magnifications; (c) TEM image of sample F-Ti-KLE-2.

After the preliminary study via electron microscopy on pore structure of mesoporous TiO_2 samples, we can now basically draw a conclusion regarding the optimum conditions, which are the synthesis conditions of sample F-Ti-PP-4, to make mesoporous TiO_2 for further detailed investigations.

4.2.2.2 Detailed Characterizations of Mesoporous TiO_2 film

The WAXS pattern of sample F-Ti-PP-4 after calcination is shown in Figure 4.6. The WAXS pattern of as-prepared dopamine functionalized TiO_2 nanoparticles is also plotted in the same diagram for comparison. Due to the extremely small amount of material on the substrate, the quality of the pattern of sample F-Ti-PP-4 is not satisfying. Only one pronounced peak of (101) reflection at 2θ=25.3^o can be clearly seen and two other tiny peaks of (004) and (200) reflections can be roughly located. Certainly, the crystal structure of sample F-Ti-PP-4 remained as anatase phase of TiO_2 after 470^{o}C calcination, which could be taken as a proof of the thermal stability of preformed TiO_2 nanocrystals.

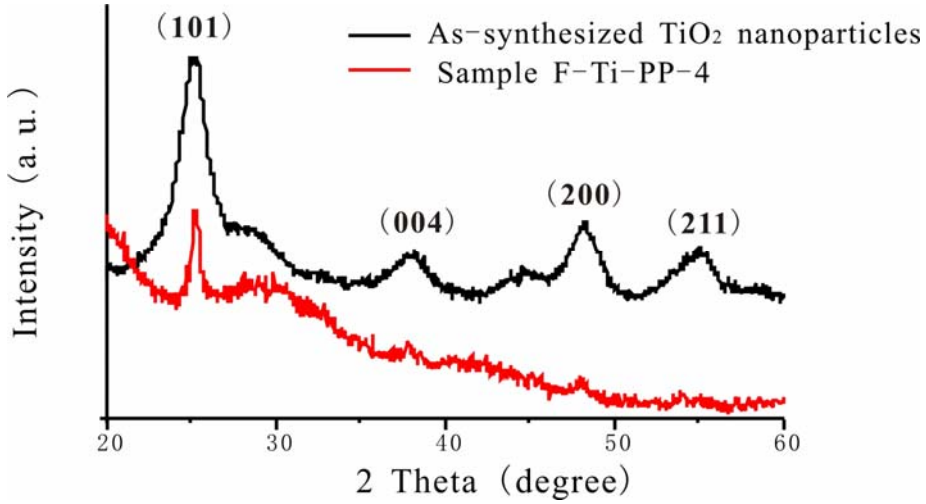

Figure 4.6 WAXS pattern of sample F-Ti-PP-4 and as-synthesized TiO_2 nanoparticles.

SEM images of sample F-Ti-PP-4 are presented in Figure 4.7. Figure 4.7b shows that the surface of the TiO_2 film is rather flat and with many pores and some large cracks, indicating good accessibility of the pores to the exterior. As we've seen in the TEM images before, there is no pore ordering at all. The pore size varies in the range of about 10 nm to 40 nm. In Figure 4.7a, one can see on the cross section part that the porous structure is mainly constructed by loose particle clusters and pores among the clusters. This, on one hand, certifies the completely irregular pore ordering, on the other hand, gives a hint that this material has high surface area.

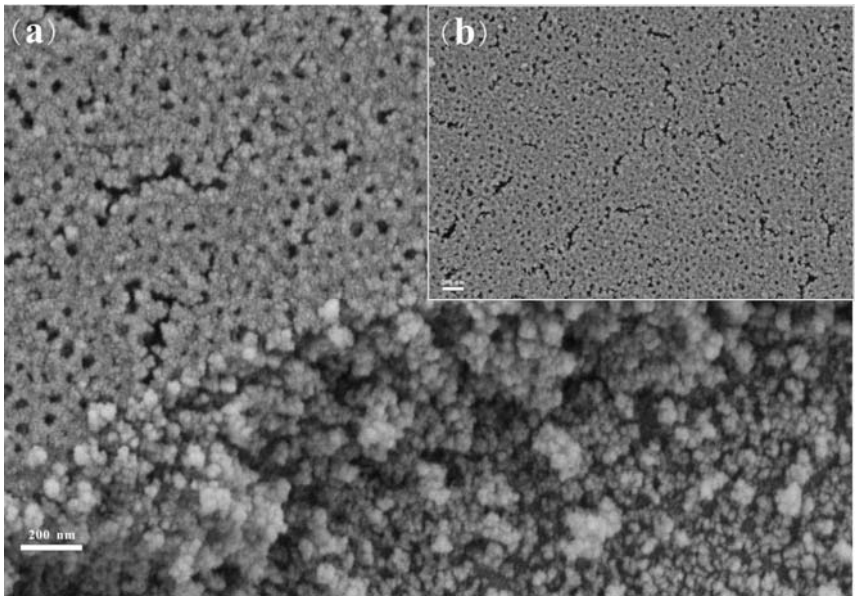

Figure 4.7 SEM images of sample F-Ti-PP-4: (a) the cross section and (b) the overview on the surface of the film. All scale bars represent 200 nm.

Due to the difficulty of making large amount of mesoporous TiO_2 films, krypton was used to perform BET measurement for the specific surface area instead of nitrogen. The krypton adsorption isotherm is given in Figure 4.8, by which the specific surface area is then calculated to be 200 m^2/g. When the relatively large pore size (~20 nm) and irregularity of the pore distribution are taken into account, this value is already along theoretical expectation. Besides, this value is also very close to the BET specific surface area of mesoporous TiO_2 films in the literatures,[5, 17] which were 205 m^2/g and 190 m^2/g, respectively. The correlation coefficient of the krypton adsorption measurement is 0.999321, which indicates the very high accuracy of the measurement.

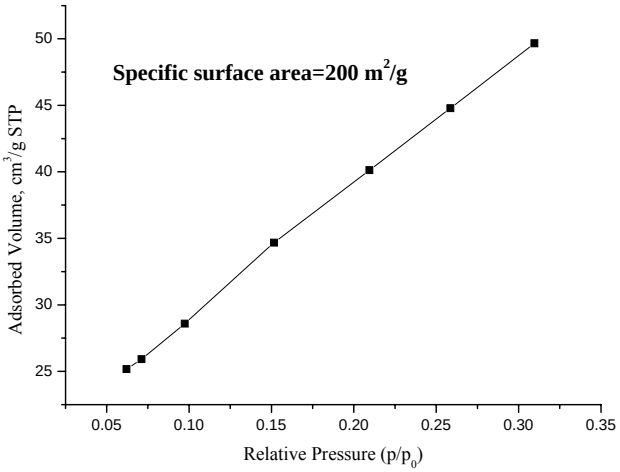

Figure 4.8 Krypton adsorption isotherm of sample F-Ti-PP-4.

Due to the tiny amount of sample, it was not possible to perform any SAXS measurements on the Kratky camera.

4.2.2.3 Characterizations of Mesoporous TiO_2 Bulk Material

The WAXS patterns of sample B-Ti-PP and as-synthesized dopamine functionalized TiO_2 nanoparticles are shown in Figure 4.9. The pattern of sample B-Ti-PP can be clearly assigned to the anatase structure of TiO_2 (JCPDS, card no. 21-1272) without any indication of impurities or preferred orientations. The narrower and more intense

diffraction peaks in the pattern of B-Ti-PP than in the pattern of as-synthesized TiO_2 nanoparticles implies the higher crystallinity and larger particle size, which is totally logical because sample B-Ti-PP had been calcined at 500°C. Because the little "shoulder" nearby the (101) diffraction peak in the pattern of as-synthesized particles, which indicates the small amounts of either amorphous intermediates or brookite present in the sample, makes it difficult to clarify the range of the (101) peak, the (004) reflection line was selected to calculate the crystallite sizes of sample B-Ti-PP and as-synthesized TiO_2 nanoparticles by using Scherrer equation. The crystallite size of sample B-Ti-PP is 7.4 nm and larger than the crystallite size of as-synthesized TiO_2 nanoparticles of 4.6 nm, which quantitively proves the growth of the TiO_2 nanoparticles during calcination.

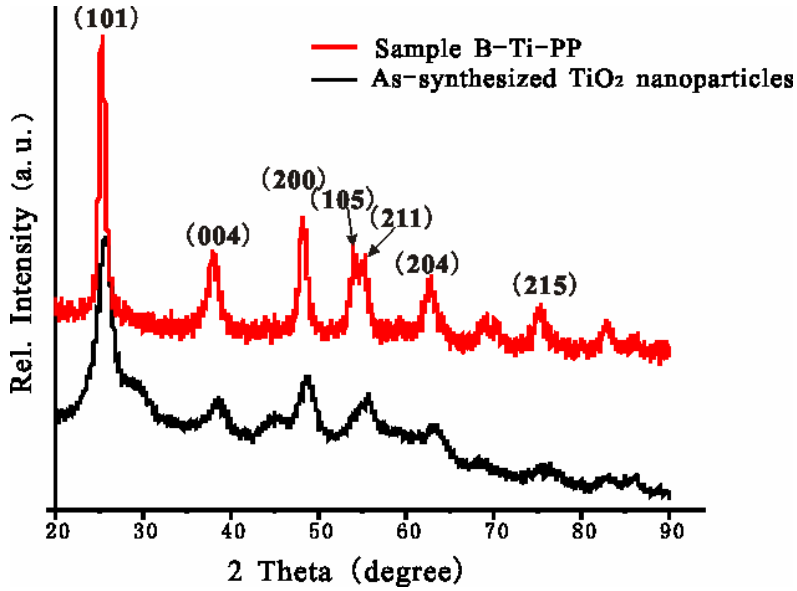

Figure 4.9 WAXS patterns of sample B-Ti-PP and as-synthesized TiO_2 nanoparticles.

The SAXS pattern of sample B-Ti-PP is shown in Figure 4.10. The relatively pronounced reflection peak in the pattern statistically confirms the presence of mesoporous structure and corresponds to a *d* value of 34.2 nm. However, no higher order reflection can be observed in the pattern, which confirmed the rather poor ordering of the mesopores.

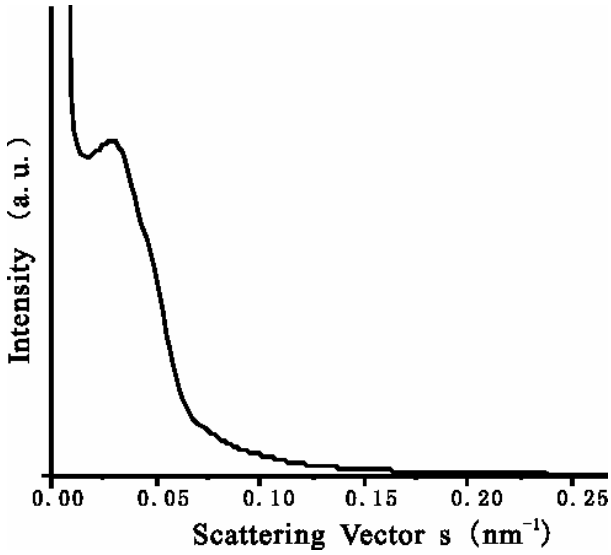

Figure 4.10 SAXS pattern of sample B-Ti-PP.

The TEM images of sample B-Ti-PP are shown in Figure 4.11. Similar to what we have seen in **4.2.2.1**, sample B-Ti-PP is highly porous, but all the pores are randomly organized. This observation also explains the lack of higher order reflections in the SAXS pattern. The pores are approximately 20 nm in diameter and the wall thickness of the pores is about 15 nm, which perfectly matches with the *d* value from the SAXS pattern in Figure 4.10 (34.2 nm). Furthermore, if we recall our observation from the TEM images of sample F-Ti-PP-4 (Figure 4.3), we would find that the pore size of mesoporous TiO_2 film is the same as the pore size of mesoporous TiO_2 bulk material. The same porous structures and the same pore sizes of sample B-Ti-PP and F-Ti-PP-4 demonstrate that the macroscopic forms of mesoporous TiO_2 produced in this project do not impact its mesoporous morphology at all.

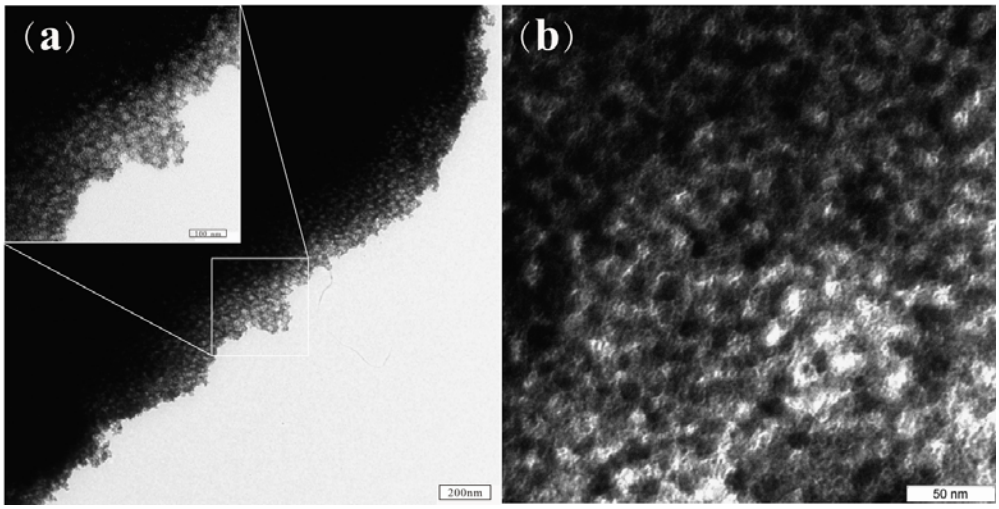

Figure 4.11 TEM images of sample B-Ti-PP having different magnifications.

The high crystallinity of TiO_2 nanoparticles as well as the pore morphology were further characterized by HRTEM. An image of one of the mesopores is shown in Figure 4.12 (the bright area is the center of the pore). It is obvious that the nanoparticles building up the wall of the pores are all highly crystalline. Moreover, the nanocrystals attach to each other randomly without any preferred orientation, which coincides with the conclusion drawn on the WAXS pattern (Figure 4.9) of the same sample. The pore shape in this image looks quite irregular, which was also observed in TEM images (Figure 4.11). However, previous study has proven that the regularity of the pore shape and the porous structure are not very important for the surface area and the catalytic properties of the sample.[47, 48]

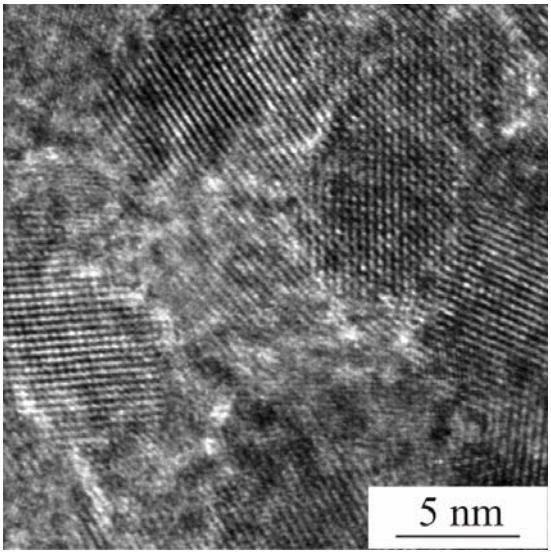

Figure 4.12 HRTEM image of sample B-Ti-PP.

SEM images of sample B-Ti-PP are shown in Figure 4.13. In Figure 4.13a, one can see that the surface of sample B-Ti-PP is very flat and with many disordered pores open to the surface, which is similar to what was seen in Figure 4.7. What is different from the surface of sample F-Ti-PP-4 is that it's completely crack-free. Actually, except the defects made during SEM specimen preparation, there were no cracks observed over several microns on the surface of sample B-Ti-PP.

Figure 4.13b and c present the internal structure of sample B-Ti-PP. They confirm the highly porous structure of sample B-Ti-PP, similar to TEM images (Figure 4.11). The pore size is quite monodisperse and the mesopores are completely disordered. These figures also give us a very straightforward feeling that the material has high surface area, which is later on proven by nitrogen adsorption measurement.

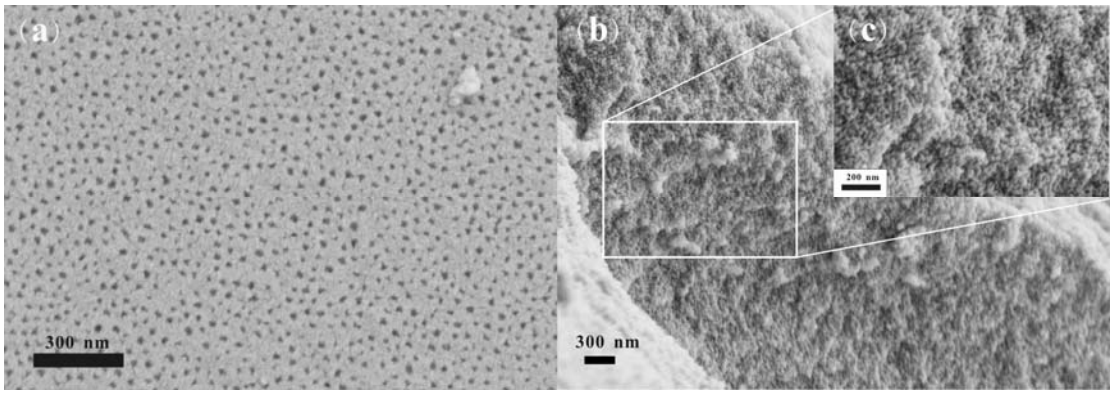

Figure 4.13 SEM images of (a) overview of the surface and (b) cross section of sample B-Ti-PP, (c) magnified image on the cross section of sample B-Ti-PP (scale bar corresponds to 200 nm).

Nitrogen adsorption-desorption isotherm of sample B-Ti-PP is shown in Figure 4.14. It corresponds to type-IV adsorption-desorption isotherm with an H2-type hysteresis.[49] According to IUPAC's definition on the dimension of mesopores,[1] this isotherm confirms that sample B-Ti-PP is mesoporous. Its specific surface area from BET measurement is approximately 130 m^2/g. It is apparently lower than the value obtained via krypton adsorption measurement on sample F-Ti-PP-4 (Figure 4.8). One of the reasons is that those two measurements were performed by using different

gases, i.e. krypton and nitrogen. Certainly, they have different adsorption-desorption properties and interactions with the surface of TiO_2 nanoparticles, which would strongly impact the measurement results. Furthermore, the tiny amount of the film sample made it difficult to measure the mass properly, leading to experimental errors. Nevertheless, the nitrogen-sorption measurement on sample B-Ti-PP offers strong proof of its mesoporosity and relatively high surface area.

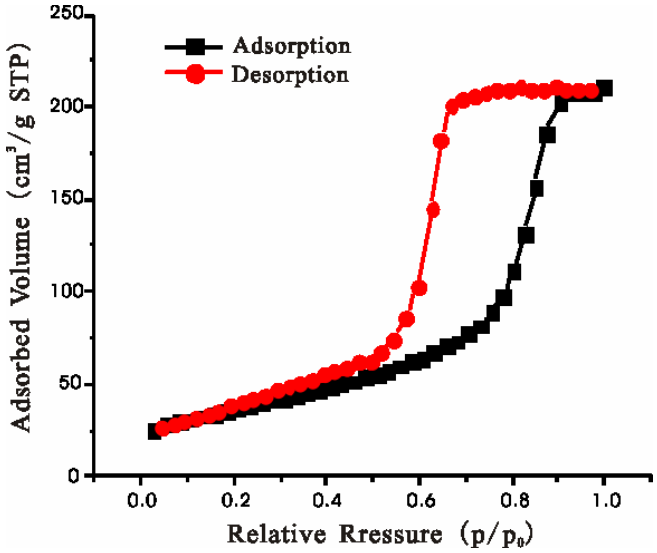

Figure 4.14 Nitrogen adsorption-desorption isotherm of sample B-Ti-PP.

In order to check if the polymer template had been removed completely, TGA measurement was performed on the uncalcined sample B-Ti-PP (TGA pattern shown in Figure 4.15). The heating rate was 20°C /min. When the temperature was below 100°C, the mass loss was mainly from the desorption of the water in the pores. In between approximately 100°C and 220°C, there is a flat stage indicating that there was basically no mass loss. After this stage, the mass loss increased dramatically and the curve went down steeply until the mass loss stopped when the temperature reached to 480°C. Afterwards, there was basically no mass loss till the end of the measurement at 933°C. The huge mass loss in between 220°C and 480°C can be easily attributed to the removal of the polymer template. Although the highest temperature that we used to calcine the sample was 470° C, lower than the ending temperature of mass loss in Figure 4.15 of 480°C, it is still safe to say that all the

organics had been removed completely by using the calcination program demonstrated by Scheme 4.2. The reason is that the heating rate of TGA measurement was 20°C /min, in contrast to only 2°C /min in the calcination program. This very high heating rate induced significant hysteresis of mass loss, which means that the mass loss should have been finished when the temperature was much lower than 480°C. Whereas in the calcination program, besides the very low and well controlled heating speed, there was an additional constant temperature stage at 300°C for one hour so that the time for the decomposition of polymer template was sufficient (the polymer template starts to decompose at approximately 220°C). Moreover, the calcination temperature was maintained at 470°C for two hours, which further ensured the complete removal of the organics. An analogous TGA experiment was also done on the sample after calcination. There was basically no mass loss observed from about 100°C to 933° C (data not shown), which strongly proves that the polymer template had been removed completely.

Figure 4.15 also shows that the total mass loss was around 60 wt% during calcination. Apart of ca. 5 wt% mass loss from water, 55 wt% of organics had been removed in total. However, the starting mass ratio of polymer template in solid materials was only 40 wt% (0.2 g PB-PEO and 0.3 g TiO_2 nanoparticles). Therefore, ca. 15 wt% mass loss can only be attributed to the removal of organic modifier, mainly dopamine, attached to the surface of TiO_2 nanoparticles.

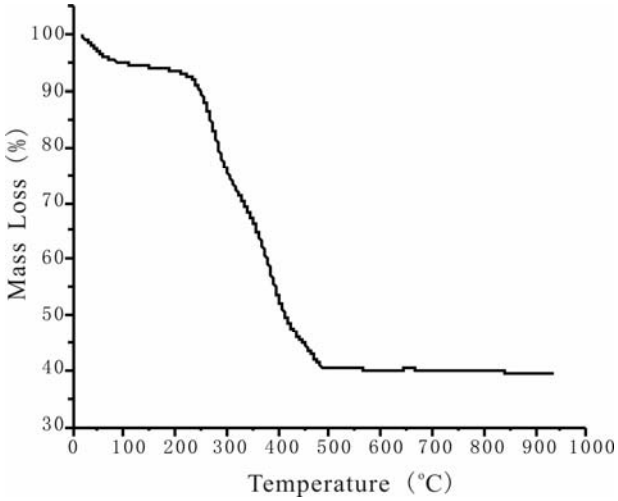

Figure 4.15 TGA measurement of sample B-Ti-PP.

4.2.3 Conclusion

In this part of the PhD work, both mesoporous TiO_2 films and bulk material have been successfully produced. WAXS, TEM, SEM and BET measurements elucidated their high crystallinity, highly porous structure, relatively high surface area and very good thermal stability up to 470^{o} C. In addition, more characterizations on mesoporous TiO_2 bulk material, i.e. SAXS, HRTEM and TGA, revealed the detailed features of its porous structure and the successful removal of the polymer template.

As a conclusion, these results give good evidence for the promising potential to employ preformed nanocrystals as NBBs in EISA process for the formation of mesoporous metal oxides. This conclusion will be further confirmed by the successful synthesis of mesoporous SnO_2 in the following context.

4.3 Synthesis of Mesoporous SnO_2

In chapter 3.2, a nonaqueous synthesis approach and characterizations of nearly monodisperse crystalline tin oxide nanoparticles with an average diameter of 3.5 nm were presented. The as-synthesized SnO_2 nanoparticles exhibit very good potential for the formation of mesoporous SnO_2 via EISA procedure because of their high dispersibility in THF (details given in chapter 3.2).

Therefore, the strategy of this project was to produce mesoporous SnO_2 by the addition of PB-PEO block copolymer as template to the THF solution of SnO_2 nanoparticles, which subsequently induces the cooperative assembly of the nanoparticles and the PB-PEO block-copolymer micelles via EISA and finally results in the formation of a 3D network of mesoporous SnO_2. It's actually very similar to the formation of mesoporous TiO_2 presented in chapter 4.2, however with different solvents. In the case of TiO_2, the mixture of water and ethanol was the dispersing solvent, whereas for SnO_2 only THF was used.

4.3.1 Experimental

In chapter 4.2, we discussed the influence of volume ratio between nanoparticles and polymer template, $V_{n/p}$, on the porous structure of TiO_2, with the best results for $V_{n/p}$=0.4. In this project, we also tried to vary the $V_{n/p}$ value and found out that the mesostructures obtained with $V_{n/p}$ in the range of 0.4 to 0.6 exhibit good long-range order of the pores. In the following, mesoporous SnO_2 obtained with $V_{n/p}$=0.5, i.e., 33.3 vol% SnO_2 and 66.7 vol% block copolymer, was selected as a representative sample and denoted as B-Sn.

4.3.1.1 Synthesis Procedure

In a typical synthesis procedure, 28.8 mg PB-PEO block copolymer were dissolved in 1.25 ml tetrahydrofuran (THF). 2.5 g of the SnO_2 nanoparticle sol (3 wt%) were added to the polymer solution leading to the formation of a cloudy mixture, which was then poured into a Petri dish with a diameter of 5 cm and dried in air at room temperature.

After two days, the Petri dish was transferred to a furnace and dried for another two days at 100°C. Finally, the thick film was peeled off the Petri dish and calcined under air following the similar calcination program shown in Scheme 4.2 except the highest calcination temperature was enhanced up to 500°C and the time remaining at this temperature was prolonged to 2 hours. The subsequently achieved material was sample B-Sn.

4.3.1.2 Characterizations

Many techniques, such as WAXS, SAXS, TEM, HRTEM, SEM and nitrogen adsorption, etc., revealed the characteristics of porous mesostructure of sample B-Sn.

4.3.2 Results and Discussion

The WAXS pattern of the sample is shown in Figure 4.16 in comparison with as-synthesized SnO_2 nanoparticles. It corresponds to the cassiterite structure (JCPDS,

card no. 41-1445) without any indication of other crystalline byproducts or preferred orientation. This is, of course, predictable from the crystal structure of as-synthesized SnO_2 nanoparticles and implies the thermal stability of the cassiterite structure of tin oxide. Comparing with as-synthesized SnO_2 nanoparticles, the narrowing and higher intensity of the peaks in the pattern of sample B-Sn indicates the growth of the particle size after thermal treatment. The particle size of sample B-Sn calculated by Scherrer equation from the line broadening of the (110) diffraction line is 10.3 nm, which is a lot larger than the particle size of as-synthesized ones (3.7 nm) and quantitatively proves the growth of the nanoparticles.

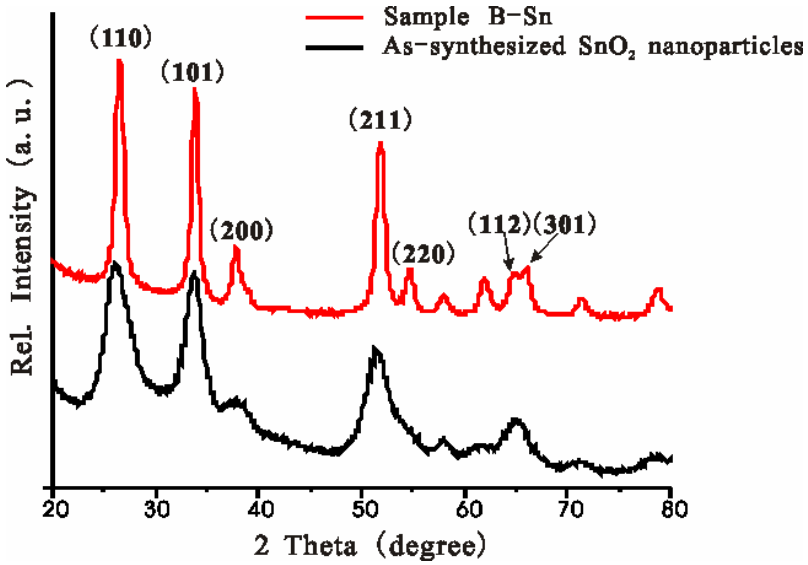

Figure 4.16 WAXS patterns of sample B-Sn and as-synthesized SnO_2 nanoparticles.

The SAXS data of sample B-Sn is presented in Figure 4.17. The pattern shows a sharp and well-resolved high-intensity first order reflection corresponding to a *d* value of 31.7 nm and also a low-intensity second-order reflection, suggesting a high degree of mesostructural order. However, one is not able to determine the structure of the mesophase unambiguously because it's impossible to locate the position of the secondary-order reflection.

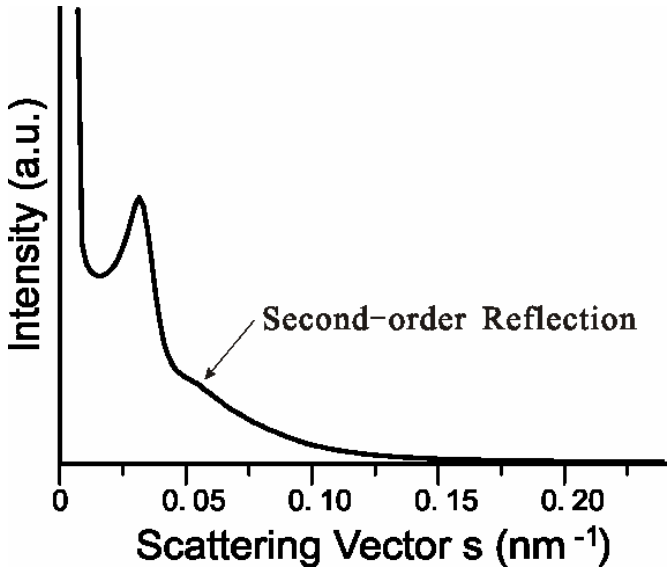

Figure 4.17 SAXS pattern of sample B-Sn.

The TEM image displayed in Figure 4.18 proves the high quality of the mesostructure obtained from preformed nanocrystalline building blocks after thermal removal of the template. Over a large area the tin oxide sample exhibits a highly ordered, cubic-like arrangement of spherical pores. Evaluation of several TEM images showed that the diameter of the pores is about 18-20 nm. Note that the size of the tin oxide nanoparticles is considerably larger in the calcined mesostructure (around 6-8 nm, which is however slightly smaller than calculated by Scherrer equation) than in the starting nanoparticle sol leading to the conclusion that the pore walls with a thickness of 12-18 nm consist of about 2 layers of nanoparticles (see also HRTEM images below), which seems to be a key parameter for the high thermal stability of the structure.

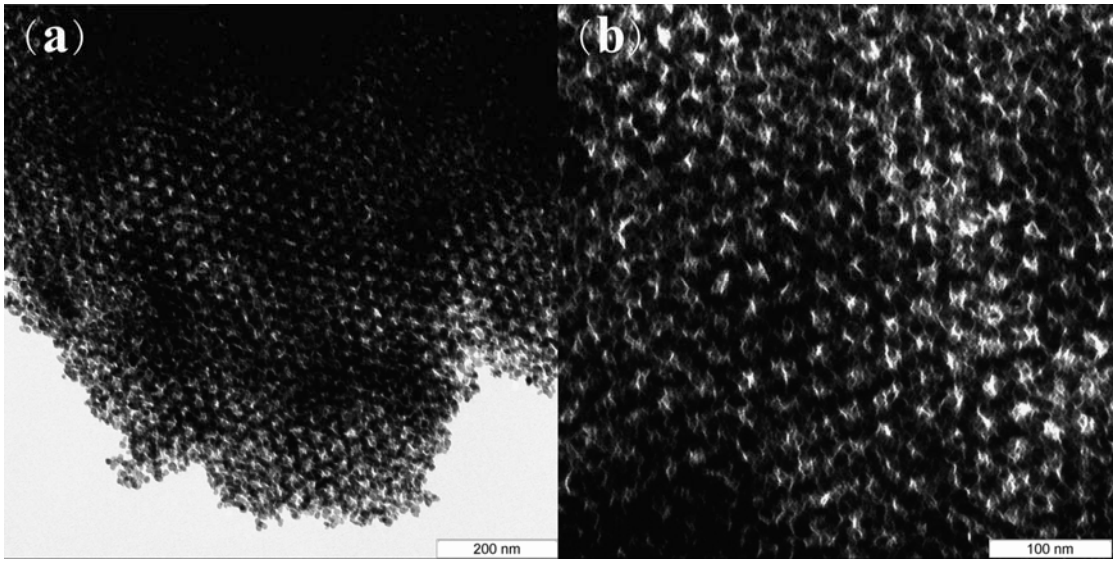

Figure 4.18 TEM images of sample B-Sn with different resolutions.

High-resolution TEM investigations give further insight into the structural features of the mesostructure (Figure 4.19). The *d*-spacings corresponding to the diffraction rings of the selected area electron diffraction (SAED) pattern (Figure 4.19a) are in agreement with the cassiterite structure (JCPDS 41-1445). The orientation of the nanoparticles within the walls is clearly seen in the HRTEM image in Figure. 4.19b. The well-defined lattice planes prove the high crystallinity of the pore walls, however there is no specific orientation of the nanoparticles with respect to each other. The power spectrum of this image displays a ring pattern, typical for non-oriented nanocrystallites (Figure 4.19c), which has been proven previously by WAXS measurement (Figure 4.16).

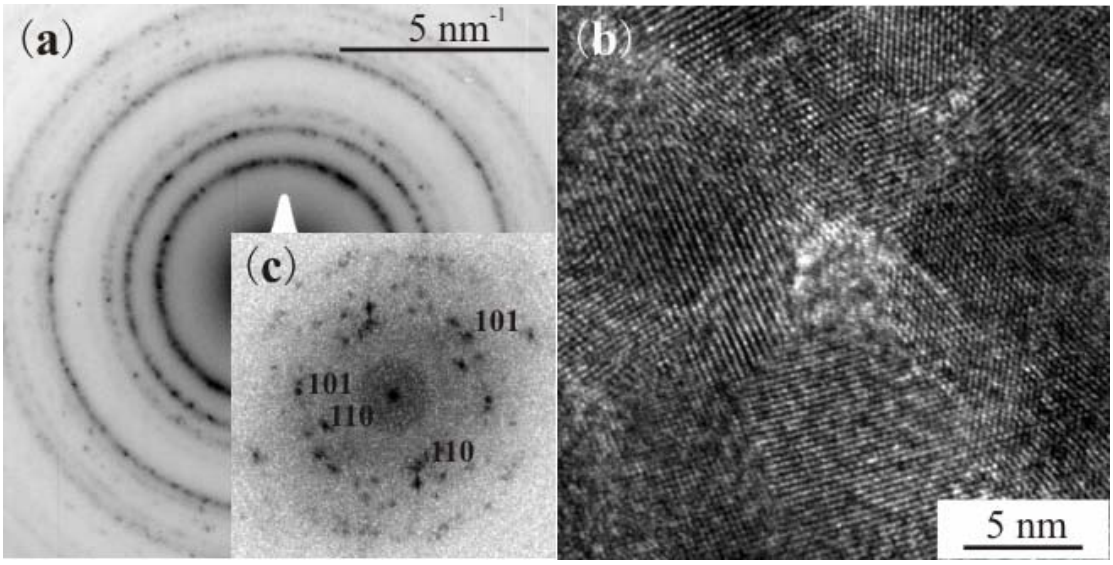

Figure 4.19 High-resolution studies on sample B-Sn. (a) SAED pattern, (b) HRTEM image and (c) corresponding power spectrum.

The SEM images of sample B-Sn in Figure 4.20 give further evidence of the porous structure of the material and underline the homogeneous size and the regular distribution of the pores. Figure 4.20a and 4.20b show the large scale of the highly ordered mesostructure over several microns. In addition to the main part of the regular mesostructure, some mesophases with different orientations can also be seen in Figure 4.20a. This is only the inhomogeneity of the mesostructure in large scale, but will not influence the properties, such as porosity, surface area or catalytic properties etc., of the material. Figure 4.20c demonstrates the highly ordered mesostructure of sample B-Sn with rather closer view and is in good agreement with the TEM images shown in Figure 4.18. The size and wall thickness of the pores can also be determined from Figure 4.20. They all fit the results obtained via SAXS and TEM measurements, which are ca. 20 nm in pore size and 12~15 nm in the wall thickness. In contrast to the perfectly aligned porous structure in Figure 4.20c, an obvious defect is observed in Figure 4.20d, in which two different directions of pore arrangement are highlighted by arrow A and B. The circle denotes the spot where defect formation occurs. The pores following direction B change its original alignment and fits into direction A. As we discussed before, it is impossible to determine the mesostructure of B-Sn upon its

SAXS pattern because it's impossible to locate the position of the secondary-order reflection. The structural defects we observed in Figure 4.20d should be one of the reasons that the intensity of secondary-order reflection was too low.

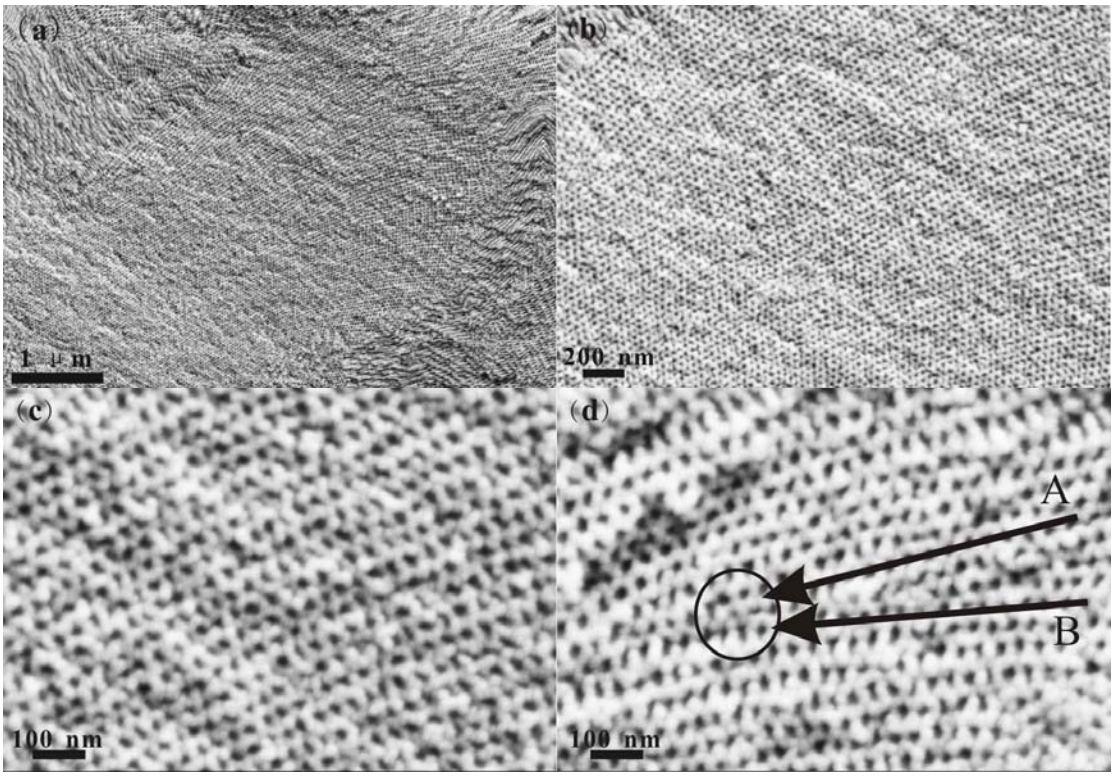

Figure 4.20 SEM images of sample B-Sn with different resolutions.

Nitrogen sorption studies carried out on sample B-Sn show a type IV adsorption-desorption isotherm with an H2-type hysteresis, confirming that the sample is mesoporous (Figure 4.21). The BET surface area is 66 m^2/g. Comparing with sample B-Ti-PP (130 m^2/g), the apparently low specific surface area is due to the high density of SnO_2 (6.95 g/cm^3 for SnO_2 and 3.84 g/cm^3 for TiO_2). The total pore volume amounted to 0.28 cm^3g^{-1}. Considering the bulk density of SnO_2 (1g SnO_2 corresponds to a volume of 0.14 cm^3), this result corresponds to an inorganic walls-to-pore volume ratio of 0.5, reflecting the volume ratio of SnO_2 nanoparticle sol and block copolymer in the starting mixture exactly. Moreover, this observation proves that there is no shrinkage of the pores during calcination, which is a distinct advantage of crystalline nanobuilding blocks as starting materials compared to sol-gel approaches based on the use of molecular precursors, where strong uniaxial shrinkage

is observed.

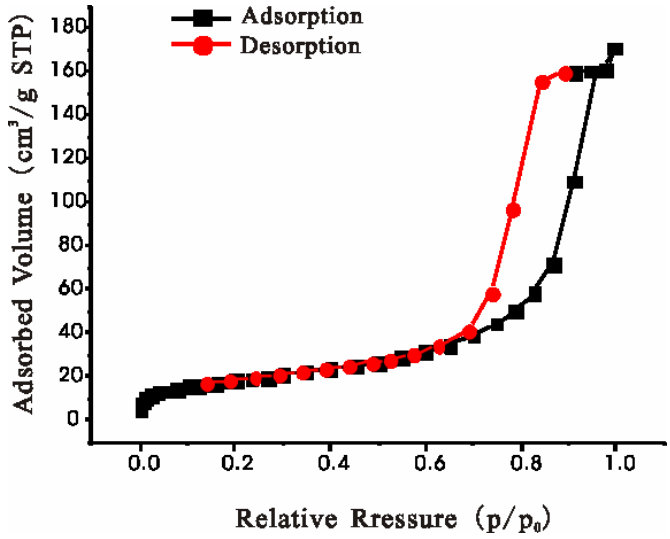

Figure 4.21 **Nitrogen adsorption-desorption isotherm of sample B-Sn.**

TGA measurement was carried out on sample B-Sn to check if the polymer template was removed completely. There was basically no mass loss in the temperature range from 100°C to 933°C (data not shown), which is also observed in TGA measurement of sample B-Ti-PP and confirms that no polymer template or organic substances were left after calcination.

4.3.3 Conclusion

In conclusion, the addition of PB-PEO block-copolymer as template to the THF solution of SnO_2 nanoparticles and subsequent evaporation of the solvent induces the cooperative assembly of the nanoparticles and the PB-PEO block-copolymer micelles, finally resulting in the formation of particularly large mesopores with an exceptionally high degree of ordering in terms of pore shape and 3D arrangement. The material is characterized by large mesopores of about 20 nm in a cubic-like arrangement and exhibits a significantly higher degree of crystallinity and pore ordering compared to previous studies. It is a peculiar feature of this approach that throughout the process no water is required.

4.4 Synthesis of Mesoporous Mixtures of Two Different Metal Oxides

As one of the main advantages of using crystalline nanoparticulate precursors to synthesize mesoporous materials, it is possible to obtain homogeneous mesoporous mixtures of more than one metal oxide by simply mixing different metal oxide nanocrystals, whereas using molecular precursors of different metal oxides usually ends up with corresponding solid solutions or leads to large scale phase separation.[5, 50] Depending on the concrete applications of the mesoporous mixtures, one is able to tune the compositions of different metal oxides in the final products by changing the ratios between various nanoparticulate precursors.

Because we were able to produce colloidal dispersions of CeO_2[18] in the mixture of water and ethanol, TiO_2 in water, SnO_2 in THF and $BaTiO_3$ in THF, the strategy of this project was to mix the nanoparticles that can be stabilized in the same solvents, i.e. CeO_2 and TiO_2, SnO_2 and $BaTiO_3$, so that the stable dispersions of two different kinds of nanoparticles could be obtained and mesoporous mixtures of corresponding metal oxides can be formed following similar EISA process we used before.

The purpose of this part of my work was to prove the possibility to synthesize mesoporous materials with complex composition by using mixtures of nanoparticulate precursors. I concentrated my work mainly on the study of structural features of the obtained mesoporous materials. Therefore, the specific properties of these materials in comparison to the corresponding pure metal oxides has not been included yet and potential applications of these two mesoporous metal oxide mixtures remain to be investigated in future work.

4.4.1 Experimental

4.4.1.1 Synthesis of Mesoporous Mixtures of CeO_2 and TiO_2, $BaTiO_3$ and SnO_2

In both cases, the volume ratio of two metal oxide components was set as 1:1 and the value of $V_{n/p}$ is adjusted to be 0.4 in the case of CeO_2/TiO_2 mixture and 0.5 in the case of $BaTiO_3/SnO_2$ mixture to compare with pure mesoporous TiO_2 ($V_{n/p}$=0.4) and SnO_2

($V_{n/p}$=0.5).

A typical synthesis procedure of mesoporous CeO_2/TiO_2 is as the following. 0.1 g (1.25 mmol, 0.026 cm^3) dopamine-functionalized TiO_2 nanoparticles were dispersed in 3.23 g water and then mixed with 2.85 g CeO_2 sol in the mixture of water and ethanol[51] (6.5 wt%) containing 1.08 mmol CeO_2 (0.026 cm^3). Meanwhile, 0.143 g polymer template, PB-PEO-23, was dissolved in 5 ml ethanol. The polymer solution in ethanol was then poured into the sol of CeO_2 and TiO_2 nanoparticles and a homogeneous solution was obtained. Similar to the procedure of making mesoporous TiO_2 previously given in **4.2.1.2**, the solution was first dried at room temperature and then in the oven at 100°C. After being calcined in the oven at 500°C, the mesoporous mixture of CeO_2 and TiO_2 was obtained and termed B-CeTi.

The tricky point of synthesizing mesoporous mixture of $BaTiO_3$ and SnO_2 was how to obtain a stable colloidal dispersion of $BaTiO_3$ in THF. Previously, a novel method to synthesize $BaTiO_3$ nanoparticles having high purity and monodisperse particle size was reported by M. Niederberger and his coworkers[52]. In order to improve the dispersibility of nanoparticulate $BaTiO_3$ in organic solvent, pentanol was used as solvent and surface function agent in addition to benzyl alcohol. After the routine synthesis procedure described in the paper, the wet precipitation obtained by centrifugation was directly dispersed in certain amount of THF so that a short-term stable (within a few days) $BaTiO_3$ sol in THF (2 wt%) can be achieved. 2.19 g $BaTiO_3$ sol (0.19 mmol, 0.0072 cm^3) was then mixed with 1.25 g SnO_2 sol in THF (0.33 mmol, 0.0072 cm^3). Then, 1.5 ml THF solution containing 0.030 g polymer template, PB-PEO-23, was poured into the mixture sol of $BaTiO_3$ and SnO_2 and a homogeneous solution was obtained. Similar to the procedure of making mesoporous SnO_2 described in **4.3.1.1**, after drying and calcination processes, mesoporous mixture of $BaTiO_3$ and SnO_2 was attained and denoted as B-BaSn.

4.4.1.2 Characterizations

In order to study the structural characteristics of the mesoporous mixtures of CeO_2/TiO_2 and $BaTiO_3/SnO_2$, various techniques, such as WAXS, EDX, SAXS, TEM and BET were performed on both samples, B-CeTi and B-BaSn.

4.4.2 Results and Discussion

In order to highlight the similarities and the differences between these two mesoporous metal oxide mixtures, their characterization results are presented parallel to each other in the following.

The WAXS patterns of sample B-CeTi and sample B-BaSn are shown in Figure 4.22a and b (black curves), respectively. Interestingly, instead of observing mixed patterns consisting of all the diffraction peaks from both components of the mixtures, the patterns of mixed metal oxides can only be assigned to one of the two components and the pattern of another component is completely missing. Only CeO_2 is observed in the pattern of sample B-CeTi and only SnO_2 can be detected in the pattern of sample B-BaSn. The WAXS patterns of the corresponding as-synthesized pure metal oxide nanoparticles are plotted in Figure 4.22a and b (red curves) as references. Although only one metal oxide is detected in WAXS, all elements are present as proven by EDX (see below).

One of the possible explanations is that, in both cases, one of the two components melts during calcination, i.e., the nanoparticles with lower melting point coat the other component and prevent it from melting. Considering the small crystallite size, the coating layer should be just a few Angstroms in the thickness, too thin to be detected by WAXS measurements. Therefore, only the crystallinity of the coated component could be observed under X-ray. The melting points of bulk CeO_2, TiO_2, SnO_2 and $BaTiO_3$ are presented in Table 4.2. Obviously, their melting points are all much higher than 500°C. However, it is known that the melting points of nanoparticles are much lower than the melting points of their bulk materials. It is still reasonable to consider

that one or both components melt during calcination at 500°C. For sample B-CeTi, because the melting point of TiO_2 is much lower than CeO_2, it is rational only crystalline CeO_2 can be observed in the WAXS pattern according to above interpretation. However, in the case of sample B-BaSn, above explanation does not apply. The melting point of $BaTiO_3$ is higher than SnO_2, which excludes the explanation given above.

Another explanation is that both components melt during calcination. Then, the more hydrophobic component would coat the less hydrophobic one. In principle, higher refractive index indicates higher hydrophobicity of the material, which also refers to the coating component that cannot be detected by X-ray measurement. The refractive indexes of CeO_2, TiO_2, SnO_2 and $BaTiO_3$ are collected in Table 4.2. In the case of sample B-CeTi, the reality exactly matches above refractive-index explanation. However, this explanation also fails in the case of sample B-BaSn. It seems that there is more complex mechanism behind what we observed here , which cannot be explained so far.

Table 4.2

	Melting Point (°C)	Refractive Index
CeO_2	~2600	2.0
TiO_2	1855	2.4
SnO_2	1127	1.94
$BaTiO_3$	1625	1.54

Another noticeable point is that the peaks of the patterns of sample B-CeTi and B-BaSn are almost as broad as the peaks of the as-synthesized samples, which means that the crystallites did not grow much and are still quite small, although high temperature thermal treatments up to 500°C was performed on both samples. The crystallite sizes of sample B-CeTi and as-synthesized CeO_2 nanoparticles can be calculated by using Scherrer equation from the line broadening of the (220) reflection

and are 3.2 nm and 2.6 nm, respectively. By choosing the line broadening of the (110) reflection in the patterns of sample B-BaSn and as synthesized SnO_2 nanoparticles, their crystallite sizes can be calculated to be 5.2 nm and 3.6 nm, respectively. Apparently, in both mesoporous mixtures, the nanoparticles grow 23% for sample B-CeTi and 45% for sample B-BaSn upon calcinations. The growth was much more pronounced in the case of pure mesoporous TiO_2 and SnO_2 (see chapter 4.2 and 4.3). This should be attributed to the fact that every nanocrystal in the mixture is surrounded by both identical and different nanocrystals (v/v=1/1). During calcination, the interpenetration of identical nanocrystals is very limited by another species of nanocrystals, which have completely different thermal and crystallographic properties. Therefore, the growth of the nanoparticles of both components is severely restricted. That's why the diffraction peaks are all rather broad in the WAXS patterns of the calcined samples.

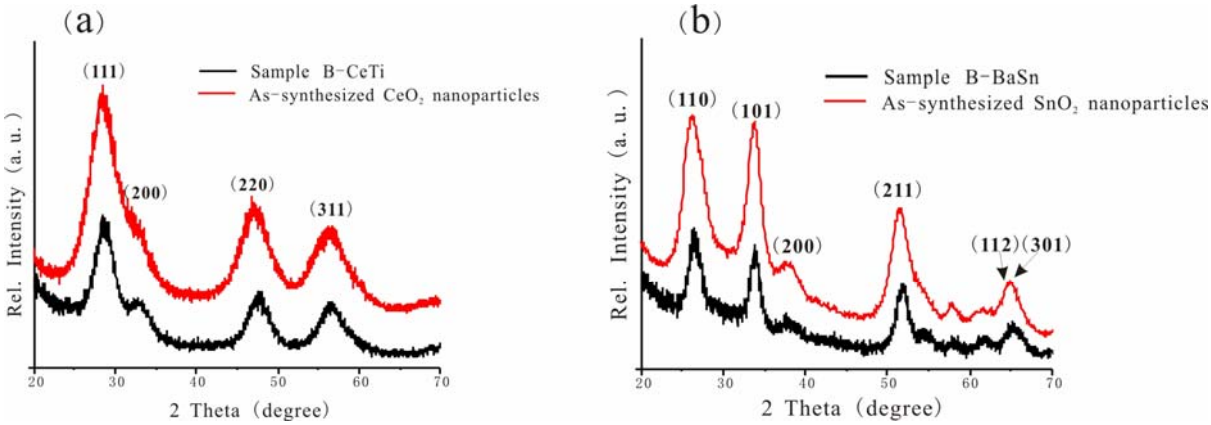

Figure 4.22 (a) WAXS patterns of sample B-CeTi and as-synthesized CeO_2 nanoparticles; (b) WAXS patterns of sample B-BaSn and as-synthesized SnO_2 nanoparticles.

Because the presence of one of the two components of both mesoporous metal oxide mixtures cannot be detected by WAXS measurement, EDX measurements were performed on both samples to prove the presence of both components. The EDX patterns of samples B-CeTi and B-BaSn are presented in Figure 4.23a and b,

respectively. Obviously, all the elements have been detected by EDX and none is missing. EDX measurements on different spots of the samples always gave the same patterns, which proves the homogeneity of the two samples.

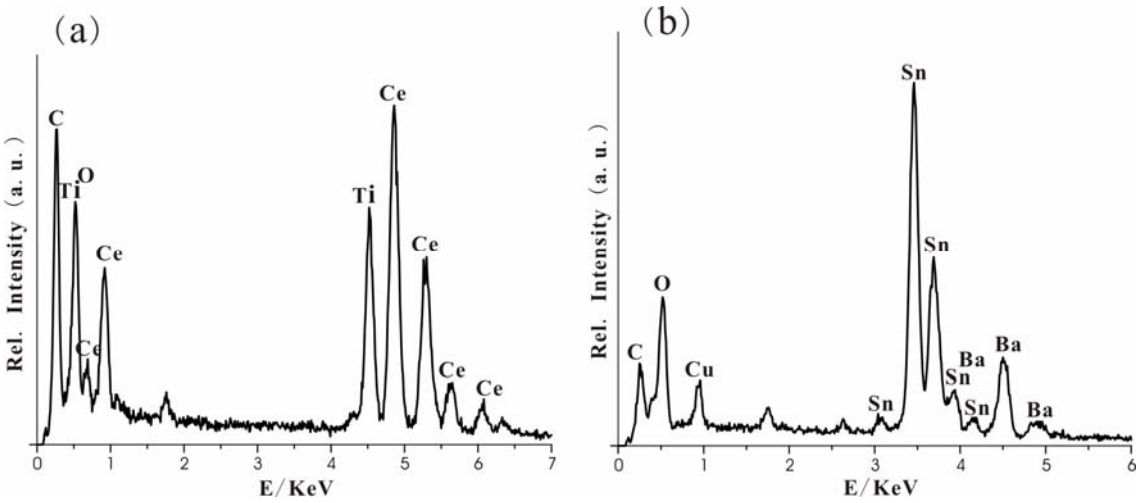

Figure 4.23 *EDX patterns of sample B-CeTi (a) and sample B-BaSn (b).*

The SAXS patterns of sample B-CeTi and B-BaSn are shown in Figure 4.24 a and b, respectively. Different from aforementioned mesoporous TiO_2 and SnO_2 (Figure 4.9 and 4.17), no pronounced reflection peaks can be observed in both patterns. Instead, only a little "shoulder" can be seen in each pattern. On one hand, this means that the mesostructures is still present in both samples; on the other hand, it is a clear indication of the poor ordering of the mesopores in both samples, which will be further proven by the TEM images in Figure 4.25. Because it is impossible to locate the exact position of each little "shoulders", the *d* values cannot be calculated.

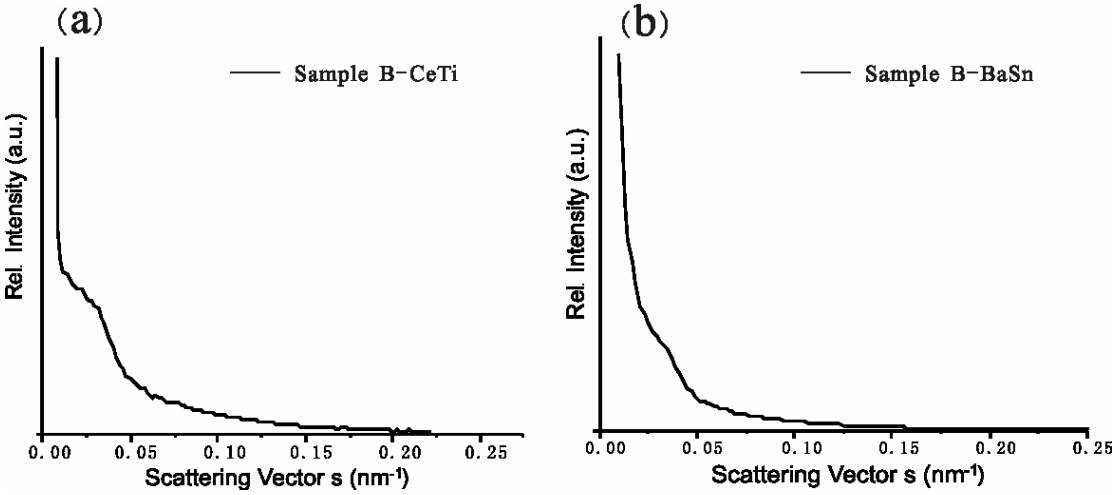

Figure 4.24 SAXS patterns of sample B-CeTi (a) and sample B-BaSn (b).

The TEM and HRTEM images of sample B-CeTi and B-BaSn are presented in Figure 4.25. The TEM images with low magnification (a and b) show that both samples are highly porous, and the pores are completely unordered, which agrees with the SAXS patterns in Figure 4.24. Closer views of two samples (c and d) reveal that their pores are very irregular in terms of both size and shape. This also explains why their SAXS patterns only show the tiny shoulders instead of pronounced peaks. Because the same polymer template was used as in the case of mesoporous TiO_2 and SnO_2, the pore sizes of both samples can be determined to be approximate 15-20 nm, close to the pore sizes of sample B-Ti-PP and B-Sn. The HRTEM images of the two samples (e and f) prove the small particle size and high crystallinity. In Figure 4.25e, the sizes of the crystallites of B-CeTi are all around 3 nm, which matches the result of crystallite size calculation via the line broadening of its WAXS pattern. Similarly, all the nanocrystals in Figure 4.25f are 5 nm or smaller, which are very close to the result (5.2 nm) calculated from the WAXS measurement.

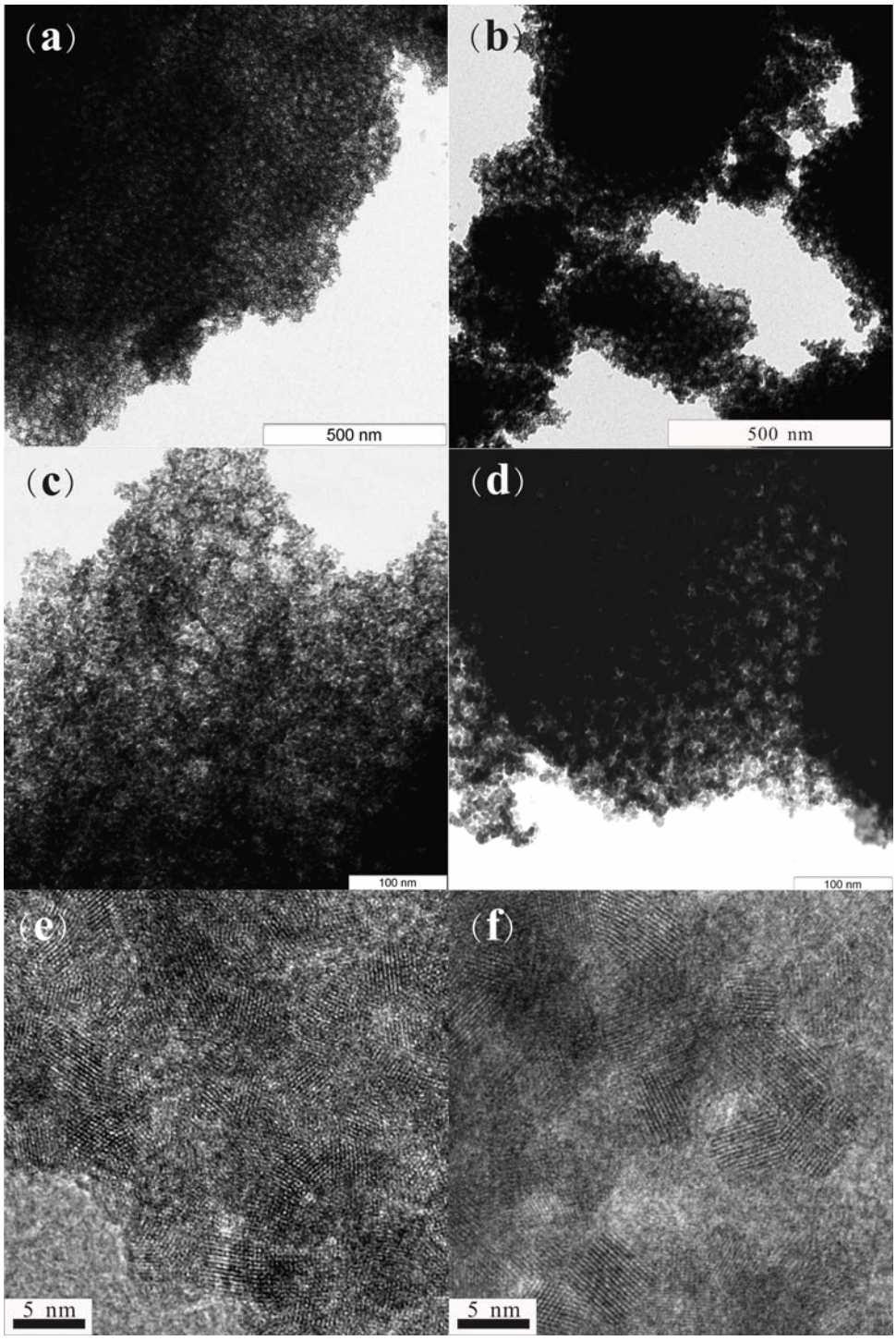

Figure 4.25 TEM images at different magnifications and HRTEM images of sample B-CeTi (a, c, e) and sample B-BaSn (b, d, f).

Figure 4.26a and b show the nitrogen adsorption-desorption isotherms of sample B-CeTi and b-BaSn. The isotherm of sample B-CeTi corresponds to type-IV adsorption-desoorption isotherm, which strongly confirms that sample B-CeTi is

mesoporous. Its specific surface area determined by BET measurement is approximately 170 m^2/g. It is higher than the specific surface area of sample B-Ti-PP (130 m^2/g) and mesoporous CeO_2 (87 m^2/g) reported in reference [18], although the same nanoparticulate precursors and synthesis procedures were used. This could be attributed to the smaller growth of the nanoparticles in sample B-CeTi during calcination. In the cases of mesoporous TiO_2 and CeO_2, the nanoparticles grew a lot during calcination and their crystallite sizes were 7.4 nm and 6.8 nm. However, the crystallite size of CeO_2 in sample B-CeTi is only 3.2 nm, much smaller than the particle size of pure mesoporous TiO_2 or mesoporous CeO_2. Smaller particle size means larger surface area, directly leading to the higher specific surface area of sample B-CeTi than pure mesoporous TiO_2 and CeO_2. Comparing with sample B-CeTi, the isotherm of sample B-BaSn is more complex (Figure 4.26 b). On the one hand, the hysteresis in the diagram is a unique sign of the mesoporosity of sample B-BaSn; however, on the other hand, the adsorbed volume increases dramatically in high relative pressure area (around 0.9 to 1.0), which is a feature of macroporous structure and indicates the presence of macropores in sample B-BaSn. Therefore, the porous structure of sample B-BaSn could be described as a coexistence of mesopores and macropores rather than simply saying that it is mesoporous. The specific surface area of sample B-BaSn is 85 m^2/g. It is smaller than the specific surface are of sample B-CeTi because the density of the mixture of $BaTiO_3$ (6.08 g/cm^3) and SnO_2 (6.95 g/cm^3) is higher than the density of the mixture of CeO_2 (7.13 g/cm^3) and TiO_2 (3.86 g/cm^3) (in both mixtures, the volume ratio of the two components was 1:1). Besides, the presence of macropores also decreases the surface area of sample B-BaSn. One may notice that the specific surface area of sample B-BaSn is, however, larger than the pure mesoporous SnO_2 B-Sn (66 m^2/g). This can also be explained by the smaller particle size of sample B-BaSn than sample B-Sn.

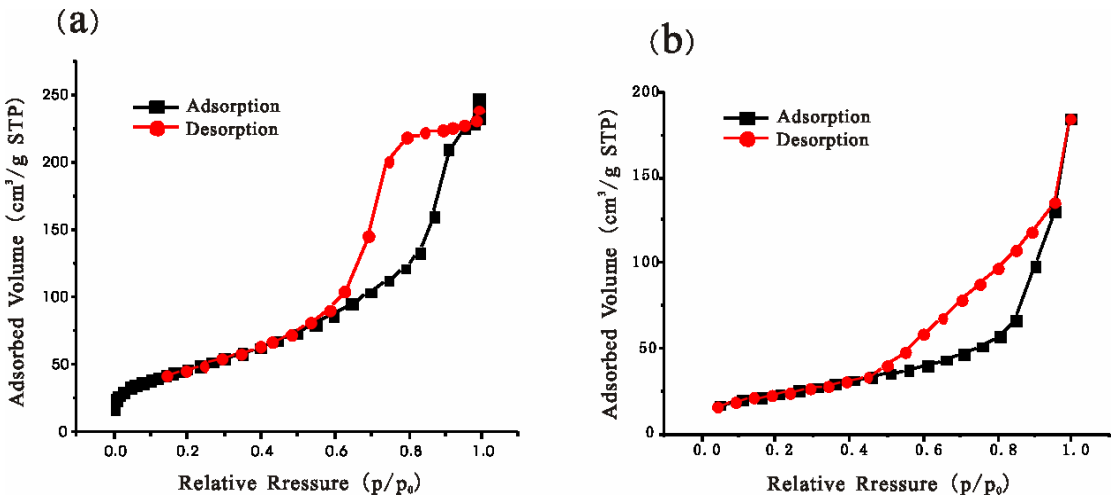

Figure 4.26 Nitrogen adsorption-desorption isotherms of sample B-CeTi (a) and B-BaSn (b).

4.4.3 Conclusion

In this part of my work, mesoporous mixtures of CeO_2 and TiO_2, $BaTiO_3$ and SnO_2 were synthesized by using the stable sols of corresponding metal oxide nanoparticles. The obtained materials are proven to be highly porous and crystalline with relatively high surface area. Most importantly, the achievement of synthesizing mesoporous metal oxide mixtures proves the unique feature of using preformed crystalline nanoparticles to construct mesoporous materials and exhibits their promising ability to make more complex mesoporous metal oxide mixtures.

4.5 General Discussion on the Formation of Mesoporous Structures Using Preformed Metal Oxide Nanocrystals

Different from the classical route to synthesize mesoporous metal oxides using molecular precursors, typically metal chlorides or metal alkoxides, preformed metal oxide nanocrystals were employed as building blocks to construct mesoporous materials in this project. Previously successful syntheses of mesoporous tungstated zirconia[7] and mesoporous CeO_2[16, 18] have proven the validity of this strategy. The syntheses of mesoporous TiO_2, SnO_2 and the mixtures of metal oxides strongly confirm that the utilization of crystalline NBBs to produce mesoporous metal oxides

is not only just an alternative method to molecular precursor route, but also an important complement to them.

In the following, I would like to roughly summarize the factors impacting the formation of mesoporous materials and give some basic and general principles that have to be followed in further work of synthesizing mesoporous metal oxides using nanoparticulate precursors. Although only a limited number of experiments were performed within this work, I think that some general trends can be discussed.

4.5.1 Factors Impacting the Formation and Ordering of Mesopores

1. Intrinsic chemistry properties of all substances involved in the EISA process

Like in the other chemistry processes, they are certainly the most important factors deciding rather than just impacting the entire EISA process. Assuming that the hydrophilic-hydrophobic interactions do not exist in the nature or the preformed nanocrystals are thermally unstable, none of aforementioned examples could be achieved. However, because men can only use but not really control these properties in most of the cases, they won't be further discussed in the following although they surely play a crucial role in EISA.

2. Particle size as well as the dispersibility of the preformed nanocrystals in continuous phase

Table 4.2 presents the mean particle sizes of the nanocrystals used for the formation of mesoporous materials reported in the literatures and obtained in my work. It is apparent that the nanocrystals used in all cases are smaller than 6 nm, even down to 3 nm, which is very small for crystalline nanoparticles and underlines the dimension of the nanoparticulate precursors used in this approach. This extremely small particle size is necessary for the formation of mesoporous structures. The main reason is, only when the nanocrystals are so small, the superamolecular interactions, which are mainly hydrophilic-hydrophobic interactions here, are able to overcome the aggregate tendency of the nanoparticles and enable the polymer templates (hundreds nanometers

in length) to manipulate the nanocrystals to construct mesopores. Another reason is that the very small particle size offers the possibility to disperse the nanocrystals in certain solvent, which is one of the prerequisites for the formation of mesopores (discussed later). Furthermore, the very small particle size also keeps the space for the growth of nanoparticles during calcination without destroying the porous structures. Last but not the least, the small particle size is also a demand of fitting the size of the mesopores, because it's not very probable to build around 10 nm sized mesopores with same or greater size building blocks.

Besides the small particle size, another similarity of the examples is that the nanocrystals in all cases were well dispersible in certain solvent (water, mixture of water and ethanol or THF) and they were all applied in the form of colloidal dispersions. Their good dispersibility is not only a reflection of their very small particle size, but also an obvious indication that they all have very good mobility to be operated by polymer templates and allows them to follow the direction of the templates to build up the mesostructures. It seems that a homogeneous colloidal dispersion of preformed crystalline nanoparticles is one of the prerequisites that have to be fulfilled to realize corresponding mesoporous materials.

Table 4.2 Main examples of mesoporous metal oxides using preformed nanocrystals as building blocks and the mean particle sizes of the nanocrystals

Mesoporous metal oxide	Measurement technique	Mean particle size (nm)
Tungstated ZrO_2[7]	HRTEM	3
CeO_2[16]	N/A	5
CeO_2[18]	AUC	3
TiO_2	AUC	5.5
SnO_2	AUC	3.5

The comparison of mesoporous TiO_2 and SnO_2 in consideration of their porous structures is a good example revealing the influence of the particle size as well as

dispersibility on the mesoporous structures. As what we've seen in chapter 4.2 and 4.3, the size of SnO_2 particles was only 3.5 nm and they were very well dispersible in THF without any additional dispersing agent; in contrast to that, the size of TiO_2 nanoparticles was as large as 5.5 nm and they can only be stabilized in water by dopamine molecules attached on the surface of the particles. According to the previous discussion, it's clear that SnO_2 nanoparticles exhibited better ability to construct mesopores and porous structures than dopamine functionalized TiO_2 nanoparticles. The fact was indeed that the pores of mesoporous SnO_2 were highly ordered, whereas there was basically no pore ordering in mesoporous TiO_2.

As a short conclusion, in order to successfully synthesize mesoporous metal oxide materials, partial efforts should be put on minimizing the size of the crystalline NBBs as well as optimizing their dispersity in proper solvents. The realization of relatively concentrated colloidal dispersion of the nanoparticles is truly the tricky and crucial point of this approach.

3. The ability of micellization, chain length and robustness of the polymer templates

Different from classical nonionic surfactants, small block oligomers composed of an oligoethylene and oligo(ethylene oxide), amphiphilic block copolymers have many advantages to be utilized as templates in making mesoporous materials, such as larger molecular weight as well as longer chain lengths to induce large accessible mesopores, great variability in composition and functional groups, greater robustness in thermal treatment, etc.

As templating agent, the block copolymer should not only be able to form stable micelles and provide control of the pore sizes, but also be robust enough to maintain the porous structure in the transformation from soft matter, liquid crystal phase, to hard inorganic framework during calcination. Among the examples given in Table 4.2, two kinds of nonionic block copolymers were employed as templating agents, commercially available Pluronic P-123 and PB-PEO-23 synthesized in our institute

(structures shown in Figure 4.27). Pluronic P-123 is a poly(ethylene oxide)-*block*-poly(propylene oxide)-*block*-poly(ethylene oxide) triblock copolymer and has successfully served as template to make mesoporous materials using both molecular and nanoparticulate precursors. Its number-average molecular weight is approximately 5750 g/mol and its stretched chain length is about 40 nm (the bond lengths of C-C bond and C-O bond are 0.154 nm and 0.143 nm, respectively) with a 25 nm long hydrophobic block. Depending on different inorganic precursors and reaction systems, Pluronic P-123 led to different *d* spacing values varying from 8.6 nm to 12.2 nm and different pore diameters between 4 nm to 7 nm.[7, 16] The huge difference between the polymer chain length and the actual pore size (strictly related to the size of micelles formed by polymer template) indicates that the polymer chains were folded in the micelles to balance the interfacial forces. We did try to use Pluronic P-123 to make mesoporous TiO_2. However, no TiO_2 with regular large mesopores could be obtained. The reasons are, at first, the size of dopamine functionalized TiO_2 nanoparticles (5.5 nm) was too large comparing with the relatively short hydrophilic blocks of Pluronic P-123 (2×7.5 nm); secondly, the hydrophobic-hydrophilic contrast of Pluronic P-123 was not sufficient due to the presence of C-O bonds in the backbone of hydrophobic block. Therefore, we had to find some other polymer template, which has longer chain length, higher hydrophobic-hydrophilic contrast than Pluronic P-123 and also, sufficient thermal stability. Finally, block copolymer PB-PEO-23 was found to be able to fulfill all the demands for making mesoporous materials with large nanoparticles.

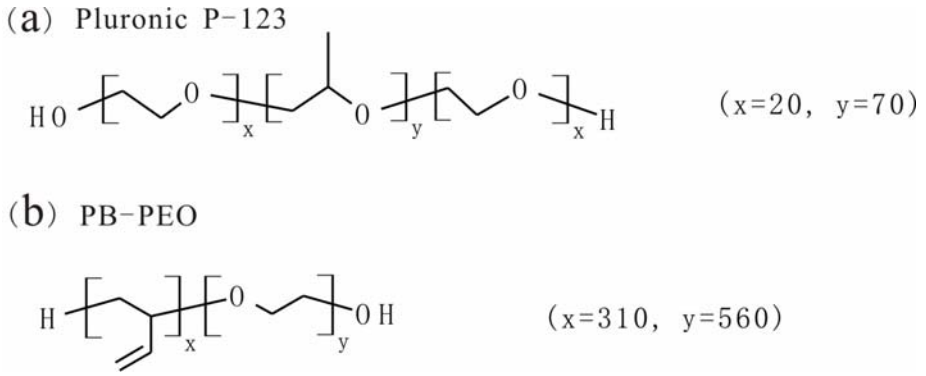

Figure 4.27 Molecular structures of polymer templates, Pluronic P-123 (a) and PB-PEO-23 (b).

PB-PEO-23 is a poly(butadiene)-*block*-poly(ethylene oxide) diblock copolymer. The number-average molecular weight of PB-PEO-23 is approximate 41630 g/mol. Its stretched chain length is about 340 nm with a 245 nm long hydrophilic block. Apparently, the molecular weight and chain length of PB-PEO-23 are all much greater than Pluronic P-123 indicating that PB-PEO-23 should introduce larger pore size in the final mesoporous materials and has better ability to handle the nanoparticles. It is noticeable that the hydrophilic-hydrophobic contrast of PB-PEO-23 is better than Pluronic P-123 as there is no polar bond existing in the backbone of hydrophobic block (the hydrophilic blocks are all polyethylene oxide). Moreover, PB-PEO-23's ratio of the length of hydrophilic block and hydrophobic block is much larger than the ratio of Pluronic P-123, which suggests that PB-PEO-23 has much better micelle formation ability than Pluronic P-123. The successful syntheses of mesoporous CeO_2 and TiO_2 proved the great validity of PB-PEO-23 to be employed as templating agent of mesoporous materials. Furthermore, the achievement of mesoporous SnO_2 demonstrated that PB-PEO-23 is also able to form highly ordered porous structure in THF. In contrast, Pluronic P-123 was only reported to form porous structure in ethanol or mixture of ethanol and water. This feature of PB-PEO-23 greatly broadens its potential applications in organizing THF dispersible nanocrystals. Last but not the least, the huge molecular weight and chain length of PB-PEO-23 offers very good thermal stability and allows it to prevent the collapse of the mesopores during calcination.

The comparison of Pluronic P-123 and PB-PEO-23 demonstrates the importance of choosing the proper polymer template to make mesoporous materials. It also proves the possibility to tune the pore size by changing the chain length of the polymer, e.g., 4-7 nm for Pluronic P-123 and 15-18 nm for PB-PEO-23. Besides, in order to adapt the relatively large particle sizes, block copolymers having compatible chain length, especially the chain length of the hydrophilic block, have to be used.

4. Influence of the solvents

First of all, as the continuous phase, a proper solvent being able to well disperse both nanocrystals and polymer template has to be used so that those two components could have high mobility for further EISA process. Since all the metal oxide nanocrystals are hydrophilic, only polar solvent could be considered as candidates and therefore many organic nonpolar solvents have been excluded by this point. Besides, in order to drive polymer templates to form stable micelles, solvents having strong polarity and hydrophilicity are highly required. Consequently, ethanol or mixture of water and ethanol are usually employed as continuous phase for both molecular and nanoparticulate precursors.

It is a little special that THF was used as the solvent in the case of making mesoporous SnO_2 because both the polymer template and crystalline SnO_2 nanoparticulate were all perfectly dispersible in it. Furthermore, it was also known that PB-PEO-23 could form stable micelles in THF, which was very important for the formation of mesostructure.

5. Organic ligands attached to the surface of NBBs

The organic ligand, which binds to the surface of the crystalline nanoparticles and improves the dispersity of NBBs in the solvent, strongly impacts the hydrophilicity of the nanoparticles, changes the interactions with the polymer templates and will definitely further influence the porous structure of the mesoporous materials.

In order to synthesize mesoporous CeO_2, 6-aminocaproic acid (ACA), $NH_2(CH_2)_5COOH$, was introduced as a ligand into the colloidal dispersion of CeO_2 nanoparticles to strengthen the interaction between nanoparticles and polymer template in reference [16] (sketch shown in Figure 4.28). However, no additional ligand was added into the CeO_2 sol in reference [18] due to the high dispersibility of CeO_2 nanocrystals in the mixture of ethanol and water. Because high order reflections can be observed in the SAXS pattern of mesoporous CeO_2 in reference [18] whereas only one broad peak could be observed in the SAXS pattern of mesostructured CeO_2

in reference [16], it can be deduced that CeO_2 mesostructure in reference [18] is better than the mesostructure in reference [16]. There are many reasons leading to the slightly less ordering of the mesopores in reference [16]. I think one of the main reasons is that there is a 5-carbon alkyl part in ACA molecules, which causes less hydrophilicity of the CeO_2 nanoparticles than the naked CeO_2 nanoparticles in reference [16].

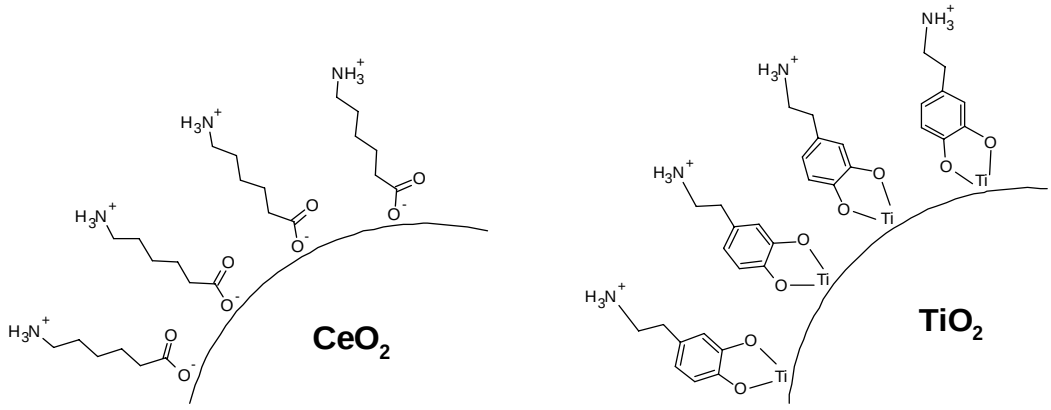

Figure 4.28 Sketches of surface functionalization of CeO_2 and TiO_2 nanoparticles

A more obvious example is the mesoporous TiO_2 formed by dopamine functionalized TiO_2 nanocrystals. As I mentioned before, dopamine molecules were covalently attached on the surface of TiO_2 nanocrystals[26] (sketch shown in Figure 4.28). As there is a rigid benzene ring in the dopamine molecules, the hydrophilicity of the TiO_2 nanoparticles was strongly decreased and the ordering of the mesopores was disturbed. Therefore, no highly ordered TiO2 mesostructure was achieved (details shown in chapter 4.2). In contrast, mesoporous SnO_2 confirms that rather surface "pure" (no surface functionalization) nanocrystals are important for the formation of highly ordered mesoporous materials.

Because organic ligands are often necessary to improve the dispersity of NBBs in the solvent or enhance the interaction between NBBs and polymer template, the aim to have highly ordered mesostructure is always in contradiction to the application of organic ligands. Therefore, depending on the applications of the materials, one factor has to compromise with another to have the optimum properties.

6. Concentration of the nanoparticles

This is actually a factor related to the dispersity of the nanoparticles. In principle, one is always able to disperse some nanoparticles in a certain solvent. The question is if the concentration of the nanoparticles is high enough to build up the framework of the mesopores. Practically, 5.5 wt%[16] and 6.5 wt%[18] of CeO_2 sols, 3 wt% of TiO_2 sol and 4 wt% of SnO_2 sol were used to synthesize mesoporous CeO_2, TiO_2 and SnO_2, respectively. These data indicate a minimum concentration for the formation of mesoporous materials is necessary. My experience was, if the concentration of the nanoparticles was lower than 1 wt%, it was impossible to achieve any mesoporous materials.

7. Calcination program

This is also important factor impacting the final mesostructure. Because violent physical and chemical procedures take place during the removal of the template, the temperature has to be raised gently to preserve the porous structure. Normally, the temperature was enhanced slowly with a ramp of 2°C/min to synthesize mesoporous CeO_2,[18] TiO_2 and SnO_2. In addition, the temperature had to be maintained at 250°C or 300°C for 1 or 2 hours during calcination so that the polymer template has sufficient time to start decomposing and the nanoparticles could rearrange to fit the great change of thermal environment.

In fact, the design of the calcination program is very empirical. Careful experiments have to be done to find the right program.

8. Ambient environment during EISA

In **4.2.2**, I have discussed the influence of humidity on the mesostructure of TiO_2 films. Another important factor is temperature, which strongly impact the evaporating speed of the solvents, the mobility of the nanoparticles and polymer template, etc. However, because the EISA process using preformed nanocrystals is very robust to the surrounding conditions, the ambient environment influence much more on the

mesostructures in case of using molecular precursors than using nanoparticulate precursors. This is also one of the advantages of using crystalline nanoparticulate precursors. In practice, room conditions, i.e. ~20°C, no wind and 40% relative humidity, is sufficient for the formation of mesoporous materials using nanocrystals and no additional control is necessary.

4.5.2 Basic Principles to Synthesize Mesoporous Metal Oxides Using Crystalline Nanoparticulate Precursors

1. The size of the nanoparticles should be minimized (<6 nm).
2. Very good dispersibility of the nanoparticles in certain solvent and sufficient concentration (>1%) is mandatory.
3. Amphiphilic block copolymers having compatible chain lengths to the size of the nanoparticles and proper molecular weight are necessary to function as templating agent. High hydrophilic-hydrophobic contrast on the polymer chains and good micellization ability is preferred.
4. Pore size can be adjusted by using polymer templats having different chain lengths.
5. In order to form a metal oxide framework, hydrophilic solvents have to be used. Solvents with low boiling points and high polarity are preferred.
6. It's better not to use organic ligands attached to the surface of the nanoparticles in case that high ordering of the mesopores is desired.
7. A slow temperature-increasing calcination program has to be applied in order to both remove the polymer template completely and preserve the original mesostructure.
8. Room conditions are sufficient to perform EISA process using nanoparticulate precursors.

4.6 References

[1] IUPAC, *Pure and Applied Chemistry* **1972**, *31*, 578.

[2] C. T. Kresge, M. E. Leonowicz, W. J. Roth, J. C. Vartuli, J. S. Beck, *Nature* **1992**, *359*, 710.

[3] J. S. Beck, J. C. Vartuli, W. J. Roth, M. E. Leonowicz, C. T. Kresge, K. D. Schmitt, C. T. W. Chu, D. H. Olson, E. W. Sheppard, S. B. McCullen, J. B. Higgins, J. L. Schlenker, *J. Am. Chem. Soc.* **1992**, *114*, 10834.

[4] Q. Huo, D. I. Margolese, U. Ciesla, P. Feng, T. E. Gier, P. Sieger, R. Leon, P. M. Petroff, F. Schuth, G. D. Stucky, *Nature* **1994**, *368*, 317.

[5] P. D. Yang, D. Y. Zhao, D. I. Margolese, B. F. Chmelka, G. D. Stucky, *Nature* **1998**, *396*, 152.

[6] J. Y. Ying, C. P. Mehnert, M. S. Wong, *Angew. Chem., Int. Ed.* **1999**, *38*, 56.

[7] M. S. Wong, E. S. Jeng, J. Y. Ying, *Nano Lett.* **2001**, *1*, 637.

[8] S. Inagaki, S. Guan, T. Ohsuna, O. Terasaki, **2002**, *416*, 304.

[9] D. Kuang, T. Brezesinski, B. Smarsly, *J. Am. Chem. Soc.* **2004**, *126*, 10534.

[10] C. J. Brinker, Y. F. Lu, A. Sellinger, H. Y. Fan, *Adv. Mater.* **1999**, *11*, 579.

[11] J. Y. Y. Tao Sun, *Angew. Chem., Int. Ed.* **1998**, *37*, 664.

[12] D. M. Antonelli, J. Y. Ying, *Chem. Mater.* **1996**, *8*, 874.

[13] B. Smarsly, D. Grosso, T. Brezesinski, N. Pinna, C. Boissiere, M. Antonietti, C. Sanchez, *Chem. Mater.* **2004**, *16*, 2948.

[14] B. B. Markus Antonietti, Christine Göltner, Hans-Peter Hentze, *Adv. Mater.* **1998,** *10,* 154.

[15] M. Niederberger, G. Garnweitner, J. Buha, J. Polleux, J. Ba, N. Pinna, *J. Sol-Gel Sci. Tech.* **2005,** in print.

[16] A. Corma, P. Atienzar, H. Garcia, J. Y. Chane-Ching, *Nat. Mater.* **2004,** *3,* 394.

[17] F. Bosc, A. Ayral, P. A. Albouy, L. Datas, C. Guizard, *Chem. Mater.* **2004,** *16,* 2208.

[18] A. S. Deshpande, N. Pinna, B. Smarsly, M. Antonietti, M. Niederberger, *Small* **2005,** *1,* 313.

[19] G. Eranna, B. C. Joshi, D. P. Runthala, R. P. Gupta, *Crit. Rev. Solid State Mater. Sci.* **2004,** *29,* 111.

[20] N. Barsan, M. Schweizer-Berberich, W. Göpel, *Fresenius J. Anal. Chem.* **1999,** *365,* 287.

[21] A. Kolmakov, D. O. Klenov, Y. Lilach, S. Stemmer, M. Moskovits, *Nano Lett.* **2005,** ASAP.

[22] C. P. Nicholas, T. J. Marks, *Nano Lett.* **2004,** *4*, 1557.

[23] Y. Idota, T. Kubota, A. Matsufuji, Y. Maekawa, T. Miyasaka, *Science* **1997,** *276,* 1395.

[24] A. C. Arias, J. R. de Lima, I. A. Hümmelgen, *Adv. Mater.* **1998,** *10*, 392.

[25] A. Andersson, N. Johannsson, P. Bröms, N. Yu, D. Lupo, W. R. Salaneck, *Adv. Mater.* **1998,** *10*, 859.

[26] M. Niederberger, G. Garnweitner, F. Krumeich, R. Nesper, H. Cölfen, M. Antonietti, *Chem. Mater.* **2004,** *16,* 1202.

[27] J. Ba, J. Polleux, M. Antonietti, M. Niederberger, *Adv. Mater.* **2005,** *17***,** 2509.

[28] A. Trovarelli, *Catalysis by ceria and related materials* Imperial College Press, London, 2002.

[29] J. A. Wang, J. M. Dominguez, A. Montoya, S. Castillo, J. Navarrete, M. Moran-Pineda, J. Reyes-Gasga, X. Bokhimi, *Chem. Mater.* **2002,** *14*, 4676.

[30] H. S. Tzou, H.-J. Lee, S. M. Arnold, *Mech. Adv. Mater. Struc.* **2004,** *11,* 367.

[31] P. K. Dutta, R. Asiaie, S. A. Akbar, W. D. Zhu, *Chem. Mater.* **1994,** *6,* 1542.

[32] Y.-S. Her, E. Matijevic, M. C. Chon, *J. Mater. Res.* **1995,** *10,* 3106.

[33] T. Lee, I. A. Aksay, *Cryst. Growth Des.* **2001,** *1,* 401.

[34] Z. X. Chen, Y. Chen, Y. S. Jiang, *J. Phys. Chem. B* **2001,** *105,* 5766.

[35] A. S. Bhalla, R. Guo, R. Roy, *Mat. Res. Innovat. 2000, 4,* 3.

[36] N. Setter, R. Waser, *Acta*. *Mater.* **2000,** *48,* 151.

[37] D. Hennings, M. Klee, R. Waser, *Adv. Mater.* **1991,** *3,* 334.

[38] J.-Y. Lee, J.-H. Lee, S.-H. Hong, Y. K. Lee, J.-Y. Choi, *Adv. Mater.* **2003,** *15,* 1655.

[39] S. Förster, M. Antonietti, *Adv. Mater.* **1998,** *10,* 195.

[40] D. Grosso, G. J. d. A. Soler-Illia, E. L. Crepaldi, F. Cagnol, C. Sinturel, A. Bourgeois, A. Brunet-Bruneau, H. Amenitsch, P. A. Albouy, C. Sanchez, *Chem. Mater.* **2003,** *15,* 4562.

[41] G. J. d. A. A. S.-I. D. Grosso, F. Babonneau, C. Sanchez, P.-A. Albouy, A. Brunet-Bruneau, A. R. Balkenende, *Adv. Mater.* **2001,** *13,* 1085.

[42] F. Cagnol, D. Grosso, G. Soler-Illia, E. L. Crepaldi, F. Babonneau, H. Amenitsch, C. Sanchez, *J. Mater. Chem.* **2003,** *13,* 61.

[43] A. Thomas, H. Schlaad, B. Smarsly, M. Antonietti, *Langmuir* **2003,** *19,* 4455.

[44] T. Brezesinski, C. Erpen, K.-i. Iimura, B. Smarsly, *Chem. Mater.* **2005,** *17,* 1683.

[45] T. Brezesinski, M. Antonietti, M. Groenewolt, N. Pinna, B. Smarsly, *New J. Chem.* **2005,** *29,* 237.

[46] T. Brezesinski, B. Smarsly, K. Iimura, D. Grosso, C. Boissiere, H. Amenitsch, M. Antonietti,

C. Sanchez,, *Small* **2005,** *1,* 889.

[47] M. Antonietti, G. A. Ozin, *Chem. Eur. J.* **2004,** *10,* 28.

[48] D. R. Rolison, *Science* **2003,** *299*, 1698.

[49] C. J. Brinker, G. W. Scherer, *Sol-Gel Science* Academic Press 1990.

[50] D. Grosso, C. Boissiere, B. Smarsly, T. Brezesinski, N. Pinna, P. A. Albouy, H. Amenitsch, M. Antonietti, C. Sanchez, *Nat. Mater.* **2004,** *3,* 787**.**

[51] A. S. Deshpande, N. Pinna, P. Beato, M. Antonietti, M. Niederberger, *Chem. Mater.* **2004,** *16,* 2599.

[52] M. Niederberger, N. Pinna, J. Polleux, M. Antonietti, *Angew. Chem. Int. Ed.* **2004, 43,** 2270.

Chapter 5 Summary and Conclusions

This PhD thesis mainly consists of two parts. In the first part, nonaqueous syntheses and characterization of crystalline metal oxides nanoparticles, i.e. tin oxide (SnO_2) and tin-doped indium oxide (ITO), have been reported. The second part of the thesis focuses on the synthesis of mesoporous metal oxides using preformed crystalline metal oxide nanoparticles such as titanium dioxide (TiO_2) and tin oxide, as nanobuilding blocks (NBBs) and amphiphilic block polymer as template via evaporation induced self-assembly (EISA) process.

The SnO_2 nanoparticles were synthesized by the "benzyl alcohol route" involving the reaction between $SnCl_4$ and benzyl alcohol. They exhibit an average particle size of 3.5 nm, a rather uniform particle morphology and high crystallinity. The most remarkable feature of the as-synthesized SnO_2 nanoparticles is that they are perfectly dispersible in THF, which shows their great potential to construct mesoporous material.

The ITO nanoparticles synthesized by a nonaqueous and halide-free approach involving the reaction between indium acetylacetonate and tin *tert*-butoxide in benzyl alcohol not only exhibit high crystallinity, a narrow particle size distribution (~ 5-10 nm), and a nearly spherical particle morphology, but also possess tunable electrical conductivity in dependence on their tin-doping level. The as-synthesized sample with approximately 15 wt% of SnO_2 content shows the highest conductivity (in the form of compressed pellet) of 2.56 S/cm. The conductivity could be further enhanced to be 52.6 S/cm by sintering the sample at 700ºC under nitrogen. Investigation of the ITO samples after different reaction times nicely illustrates the transformation from an inorganic-organic hybrid material to the final ITO crystallites and might help to understand the formation mechanism of the ITO nanoparticles.

Dopamine-functionalized water-soluble TiO_2 nanoparticles were used as nanoparticulate precursors to synthesize mesoporous TiO_2 in forms of both film and bulk material. The obtained films and bulk material are all highly porous with the mean pore size of 20 nm and the specific surface area of 130 m^2/g. However, the mesopores are completely unordered.

In contrast to TiO_2, highly ordered mesostructures were observed for mesoporous SnO_2 synthesized by using SnO_2 nanoparticle sols. The specific surface area of the mesoporous SnO_2 is 66 m^2/g.

In addition to single component mesoporous metal oxides, also mesoporous materials consisting of mixtures of CeO_2/TiO_2 and $BaTiO_3/SnO_2$, were synthesized. Both of them exhibit rather high specific surface areas, which are 170 m^2/g and 85 m^2/g, respectively. Yet, no pore ordering was observed.

The second part of the thesis ends with discussion and summary of the basic principles to synthesize mesoporous metal oxides using crystalline nanoparticle precursors. Many factors such as particle size, dispersibility of the nanoparticles in the solvent and the amphiphilicity of the templating block copolymer have a strong impact on the formation of mesoporous structures.

Chapter 6. Appendix

Abbreviations

AUC…….Analytical Ultracentrifugation

BET……the Brunauer-Emmett-Teller Method

EDXS…….Energy-Dispersive X-ray Spectroscopy

EISA……Evaporation Induced Self-Assembly

HRTEM……High Resolution Transmission Electron Microscopy / Microscope

HTS……High Temperature Superconductor

ITO……Tin Doped Indium Oxide / Indium Tin Oxide

IUPAC……International Union of Pure and Applied Chemistry

JCPDS……..Joint Committee for Powder Diffraction Studies

KLE……poly(ethylene-*co*-butylene)-*block*-poly(ethylene oxide)

NBB……Nanobuilding Block

NMR……Nuclear Magnetic Resonance Analysis

PB-PEO……polybutylene-*block*-poly(ethylene oxide)

SAED……Selected Area Electron Diffraction

SAXS……Small Angle X-ray Scattering

SEM……Scanning Electron Microscopy / Microscope

STM……Scanning Tunneling Microscopy / Microscope

TCO…….Transparent Conducting Oxide

TEM……Transmission Electron Microscopy / Microscope

TEOS……tetraethylorthosilicate

TGA……Thermogravimetric Analysis

THF……Tetrahydrofuran

WAXS……Wide Angle X-ray Scattering

XPS……X-ray Photoelectron Spectroscopy

XRD…….X-ray Diffraction

YBCO……$YBa_2Cu_3O_7$

Acknowledgement

This is my favorite section to write and read in this thesis. Not because it is the only nonscientific part of this thesis, but because it is the part that I could express my gratitude to all the people who ever helped me to get this thesis done.

Firstly, I would like to thank my director, Prof. Dr. Markus Antonietti, who gave me a precious chance to do my Ph.D. as well as many valuable suggestions, great ideas, and has never stopped inspiring me.

My supervisor, Dr. Markus Niederberger, is sincerely acknowledged for generally helping me so much in many aspects, such as directing my daily experimental work, writing papers, correcting my thesis, also accommodating me in Dallenwil etc., for numerous very helpful scientific/nonscientific discussions, for his kindness and for making our group so dynamic, creative and fruitful.

My ex-colleagues and colleagues in our group, Dr. Atul Deshpande, Dr. Igor Djerdj, Dr. Georg Garnweitner, Dr. Stephanie Grancharov, Dr. Julien Polleux, Dr. Nicola Pinna and Regina Rothe are thanked for helping me a lot during my work in the institute, having much great cooperation and always making the lab filled with happiness.

I am very grateful to Dr. Bernd Smarsly for always willing to help and many very helpful discussions with him and to Dr. Dina Fattakhova for the great cooperation on ITO investigation. I also want to thank Dr. Helmut Schlaad and Ines Below for supplying me the crucial ingredient to make mesoporous materials, block copolymer PB-PEO-23.

Meanwhile, I want to thank Dr. Cornelia Sinn, every member in Bernd's group, Dr. Doreen Eckhardt, Dr. Danielle Franke and all the other colleages in colloids department for being so nice to me, always willing to help me and accelerating me to

work hard.

Further more, I am also very grateful to all of my Chinese friends who are in Berlin (or ever lived in Berlin) and colleagues/friends who are working (or ever worked) in Max Planck Campus in Golm for making my days in Berlin as well in MPI KGF so pleasant, impressive and meaningful.

I want to thank my girlfriend, my beloved Xiaohan Pan, for her endless love, for always being confident of me, for making my days with her so sweet, beautiful and unforgettable.

In the end, I want to thank my parents, Yushan Ba and Sufen Zhu, for giving me much much more than a life. I don’t know how much I owe them and what to say to express my great gratitude to them. I wish they would be very happy to see that I have done my Ph.D. successfully and would be proud of me.

List of Publications

Nonaqueous Synthesis of Tin Oxide Nanocrystals and Their Assembly into Ordered Porous Mesostructures

J. Ba, J. Polleux, M. Antonietti, M. Niederberger, *Adv. Mater.* **2005**, *17*, 2509.

Nonaqueous Synthesis of Uniform Indium Tin Oxide Nanocrystals and Their Electrical Conductivity in Dependence on the Tin Oxide Concentration

J. Ba, D. Fattakhova Rohlfing, A. Feldhoff, T. Brezesinski, I. Djerdj, M. Wark, M. Niederberger, *Chem. Mater.* **2006**, in print.

Nonaqueous Synthesis of Metal Oxide Nanoparticles: Overview and Indium Oxide as Case Study for the Dependence of Particle Morphology on Precursors and Solvents

M. Niederberger, G. Garnweitner, J. Buha, J. Polleux, J. Ba, N. Pinna, *J. Sol-Gel Sci. Tech.* **2006**, in print.